POLITECNICO DI TORINO

MASTER's Degree in ENERGETIC ENGINEERING

MASTER's Degree Thesis

Experimental assessment of *SFNM04* perovskite for chemical looping CO_2 dissociation

Supervisors

Prof. MASSIMO SANTARELLI

……

Dr. DOMENICO FERRERO

……

Candidate

FABIO BELFORTE

……

JULY 2021

Abstract

For decades, the increase in anthropogenic CO_2 emissions has represented one of the main problems to be solved or, at least, to stem. Over the years, the growth of this factor has inevitably caused a significant environmental impact leading to global warming and an increase in energy demand. The rise in energy production allowed to satisfy this demand mainly exploiting fossil fuels (coal, natural gas, etc.) as raw material in power plants. However, there have been several international agreements that aimed to reduce and mitigate the CO_2 emissions and, consequently, to keep the rise in global average temperature under control. Strong measures have been adopted with the purpose of making the power plant processes more efficient. Nevertheless, an alternative and more promising way to mitigate the emissions issue would be the energy transition to renewable sources by following a decarbonization pathway. Carbon capture, as attractive process, has been widely discussed in this work considering, however, the increasing importance of the CO_2 re-utilization for the production of synthetic fuels or chemicals by exploiting thermochemical redox cycle processes. Chemical looping for two-step thermochemical CO_2 splitting involves the use of an oxygen carrier or redox material that reacts alternately with oxidizing and reducing gas mixtures in order to produce a synthetic gas. Generally, syngas (CO/H_2 mixture) production is the main objective since it is the starting point for the production of multiple chemicals (methanol, ethanol, DME, etc.). Many different materials have been used as oxygen carrier in chemical looping processes, starting from metal oxides, then exploiting more promising materials such as cerium oxides and perovskites. In particular, this work comes from an international collaboration project involving University of Udine, Massachusetts Institute of Technology (M.I.T.), and Politecnico di Torino which aspires to propose a new perovskite-based oxygen carrier for the conversion of the captured CO_2 to carbon monoxide. The material in question is $Sr_2FeNi_{0.4}Mo_{0.6}O_{6-\delta}$ (SFNM04) and it was synthetized by University of Udine, it has been extensively investigated in order to assess its redox ability and stability through microreactor tests. An important property of this material is the formation of Fe-Ni alloys by exsolution process when subjected to a reducing environment.

This phenomena allows to Fe^{2+} and Ni^{3+}, when reduced, to exsolve from the lattice to the surface of the sample acting as catalysts for the oxidation step. Moreover, this phenomena permits to generate a large number of oxygen vacancies which are fundamental for the redox reaction allowing a larger production of CO. The experimental section of this work is focused on the CO production achieved during the oxidation reactions in which a gas mixture containing different concentrations of carbon dioxide reacts with the SFNM04 sample. Both the oxidation and reduction conditions such as operating temperatures, gas mixture compositions, and reaction times have been modified and changed in order to assess the perovskite response and the consequent CO global yield, CO maximum production rate, and the CO_2 conversion. Through all the experiments it was noticed a negative impact on the redox ability of the sample when reducing the operating temperature of both oxidation and reduction. 850°C was the maximum temperature value imposed in the thermochemical cycles performed in these experiments, moreover, increasing it too much, exceeding 850°C, could be ineffective since one of the aims to be achieved employing perovskite oxygen carrier is to obtain promising results at lower temperatures than those used for ceria or metal oxide chemical looping processes. The CO_2 and H_2 concentrations were changed and modified from about 5% up to 100% for oxidizing and reducing gas mixtures, respectively. As the concentrations increased a higher CO production was detected by the gas analyzer, so both the cases have been investigated separately, focusing first on the oxidation reaction conditions variation and then on the reduction ones. Subsequently, all the results obtained were analyzed, and it was evaluated whether the reactions could be considered completed or not, trying to identify if there was a need for further operating conditions variations in order to reach a completely oxidized or reduced sample. In conclusion, this experimental investigation represents a part of the study aimed to evaluate the redox ability of SFNM04 and its capacity to produce monoxide carbon from CO_2. Structural analysis of the sample after the thermochemical process should be integrated in order to better understand the operating conditions effects on the material and to verify whether or not the sample can be considered fully oxidized (or reduced). In addition, with an XRD analysis it is possible also to detect the eventual presence of different structural phases that

may negatively impact on the redox performance, such as carbonates ($SrCO_3$) and molybdate ($SrMoO_4$) that inhibits the re-oxidation of the sample. Nevertheless, this work would help to highlight the crucial importance of developing new materials or technologies able to pursue a decarbonization pathway aiming to reach, as soon as possible, the fulfillment of the goals evidenced by the United Nations.

Summary

List of Tables

List of Figures

Acronyms

GHG	Greenhouse Gas
UNFCC	United Nations Framework Convention on Climate Change
IEA	International Energy Agency
SDG	Sustainable Development Scenario
TFEC	Total Final Energy Consumption
TES	Transforming Energy Scenario
SDS	Sustainable Development Scenario
CCS	Carbon Capture & Sequestration
CCU	Carbon Capture & Utilization

DME	Dimethyl Ether
SMR	Steam Methane Reforming
CSP	Concentrated Solar Power
TR	Thermal Reduction
IGCC	Integrated Coal Gasification Combine Cycle
WGS	Water Gas Shift
MEA	Monoethanolamine
PSA	Pressure Swing Adsorption
CaL	Calcium Looping
ASU	Air Separation Unit
ITM	Ion Transport Membrane

EOR	Enhanced Oil Recovery
SOEC	Solid Oxide Electrolytic Cell
AEC	Alkaline Electrolytic Cell
PEMEC	Proton Exchange Membrane Electrolytic Cell
PEC	Photochemical Cell
HTGR	High-Temperature Gas Reactor
CDCL	Coal Direct Chemical Looping
CTSCL	Coal to Syngas Chemical Looping
FCC	Fluid Catalytic Crackers
PBR	Packed Bed Reactor
CLC	Chemical Looping Combustion

CLOU	Chemical Looping with Oxygen Uncoupling
WS	Water Splitting
CDS	Carbon Dioxide Splitting
CLR	Chemical Looping Reforming
MPSZ	MgO-partially Stabilized Zirconia
RPC	Reticulated Porous Ceramic
TGA	Thermogravimetric Analysis
BET	Braunauer-Emmet-Teller
SFNM	Strontium-Iron-Nickel-Molybdenum perovskite
MFC	Mass Flow Controller
UniUD	University of Udine

SCADA	Supervisory Control and Data Acquisition
TCD	Thermal Conductivity Detector
EDTA	Ethylenediaminetetracetic acid
SCS	Self-Combustion Synthesis
TPR	Temperature Programmed Reduction
XRD	X-ray Diffraction
RP	Ruddlesden-Popper
MIT	Massachusetts Institute of Technology
SEM	Scanning Electron Microscopy
TRL	Technology Readiness Level

Chapter 1

1 - Introduction

1.1 - GHGs emissions and decarbonization pathway

One of the most demanding challenges in the current years is dealing with the constantly increasing greenhouse gases (GHGs) emissions, that are correlated to the climate change effects, and thus to the global warming. Human influence on climate changes has been the dominant cause of observed warming since the mid-20^{th} century [1], and has become a principal agent of change on the planet, shifting the world out of the relatively stable Holocene period into a new geological era (Anthropocene). Attempts to remedy this problem, and raise awareness about climate changes, have been conducted since 1994 when UNFCC (United Nations Framework Convention on Climate Change), an international environmental treaty, was negotiated. The ultimate objective of UNFCC was to stabilize GHG concentrations, in the atmosphere, at a level that would have prevented harmful anthropogenic interference for the Earth's climate system. Then, in 1997, Kyoto Protocol was signed and it provided measures to reduce emissions of polluting elements by no less than 8.65%, in the period 2008-2012, compared to the emissions recorded in 1990. Furthermore, the protocol required to reduce the CO_2 emission by 5% compared to the reference year (1990). In 2016, the Paris Agreement entered in force with the long-term objective to contain the increase in global average

temperature below the 2°C threshold above pre-industrial levels and to limit this increase to 1.5°C, as this would have substantially reduced the risks and the effects of climate change. Therefore, it is evident that for a long time the role of CO_2 emissions has been taken into account and evaluated in order to try to find a way toward decarbonization. To understand the importance of a decarbonization pathway and how much it is necessary, it is fundamental to know the effects of CO_2 emissions and their nature. CO_2 is a long-lived greenhouse gas, such as N_2O, meaning that has a persistent impact on radiative forcing and, being chemically stable, is able to lasts hundreds of thousands of years in the atmosphere. Its cumulative presence in the atmosphere increases every year and, in 2020, CO_2 emissions reached 34 Gt. This is the first cause of the rise in global mean temperature, in fact, level of warming is currently increasing at a rate of 0.3°C-0.7°C per 30 years [2] (see Figure 1.1).

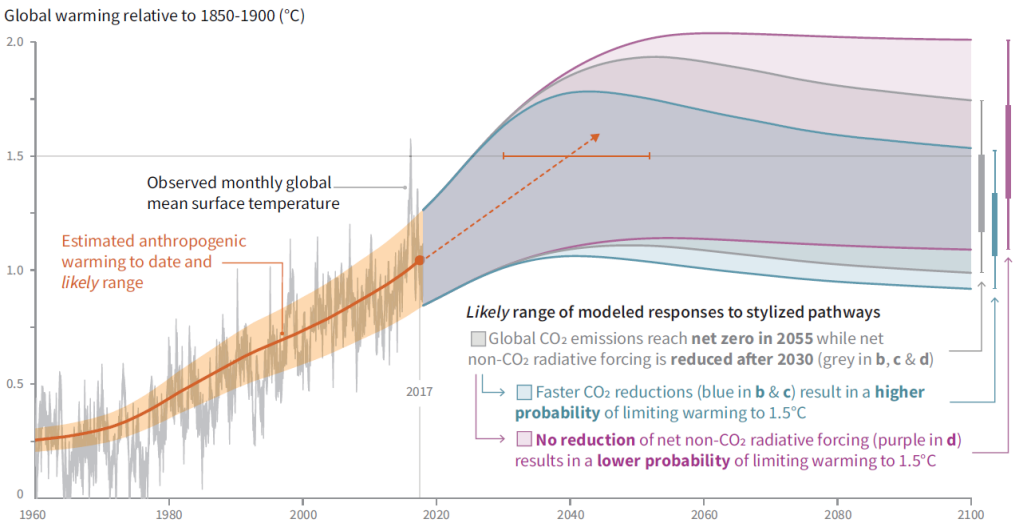

Figure 1.1: *Observed global temperature change and modeled responses to stylized anthropogenic emission and forcing pathways according to IPPC report 2018 [2].*

Understandably, switching to low-carbon sources and renewables technologies has become a "must". However, despite renewables generation growth in the power sector in the past years, there are issues related to their flexibility and integration. Renewables energy generation is affected by intermittency and fluctuation that lead to discrepancy between power supply and demand [3]. Consequently, demand for

fossil fuels is still very high, especially in developing countries, although there has been a slight decrease compared to previous year. However, in 2020, fossil fuels have met 62.8% of the world electricity generation, and among these, coal resulted in 36.4% of the total electricity production (Figure 1.2). This makes coal the main contributor to CO_2 emissions with 13.7 Gt of CO_2 emitted in 2020.

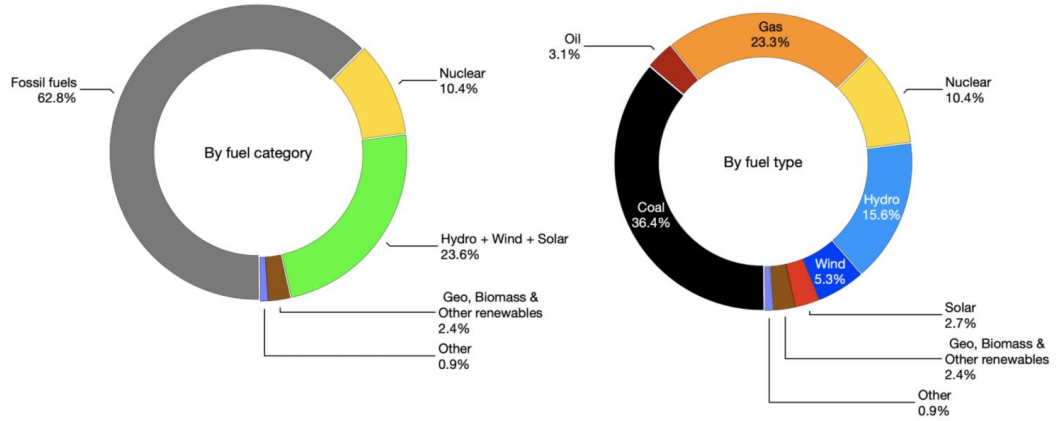

Figure 1.2: *World electricity generation [4].*

Accordingly, IEA found that CO_2 emitted from coal combustion was responsible for over 0.3°C of the 1°C increase in global average annual surface temperature above pre-industrial levels [5]. It is pointed out that, in response to higher electricity consumption, the power generation sector is the main source of CO_2 emissions, followed by the transport and industry sectors, in fact it needs to switch to low-carbon sources deploying technologies able to reduce GHG emissions. Obviously, adequate policies and measures have to be adopted worldwide in order to make the transition from conventional thermal power-generating sources to clean energy technologies faster. Sustainable Development Goal (SDG) 7, concerning "Affordable and clean energy", sets several targets to be achieved by 2030. Among these targets there are the increase in global percentage of renewable energy and the doubling of the improvement in energy efficiency, with the ultimate goal of enhancing the share of renewable energy in total final energy consumption (TFEC). Unfortunately, the world is not on track to meet the target set for 2030. Despite

impressive growth in renewable energy, the share need to accelerate in order to achieve affordable, reliable, sustainable, and modern energy [6]. According to IEA's Stated Policy Scenario, power generation from renewables is expected to reach 37% of TFEC by 2030, exceeding that of coal in 2025. Irena's transforming energy scenario (TES) sets a pathway to achieve, by 2030 a 57% share of renewables in the global power generation mix [6] (Figure 1.3). In summary, one of the ways to pursue the path of decarbonization of all end-use sectors is to reduce the consumption of fossil fuels persecuting the transition towards renewable energy sources.

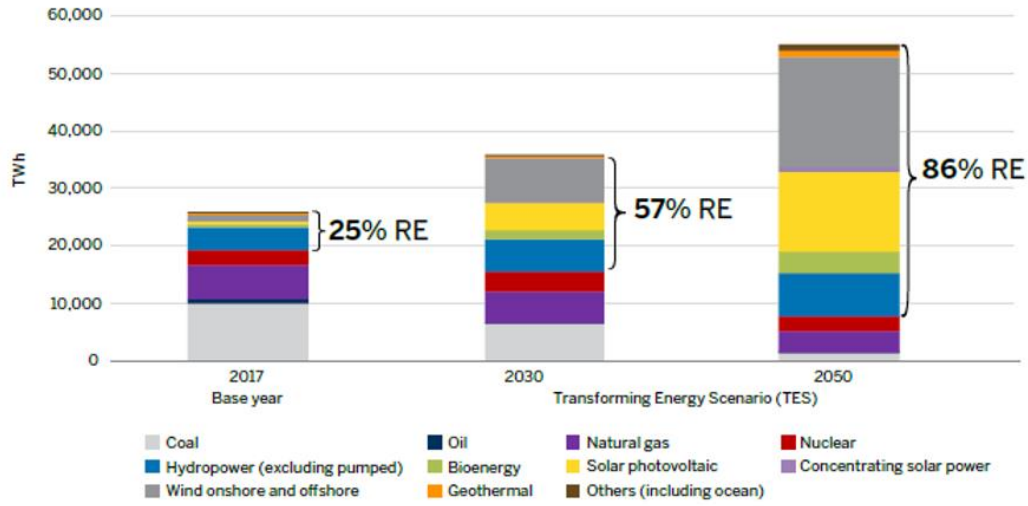

Figure 1.3: *Share of modern renewables in electricity generation [6].*

This has to be done with a proper planning of the energy sector, with policies able to drive renewable sources deployment and technological competitiveness, with investments that aim at long-term solutions. Obviously, at the same time, the capital spent on fossil fuels should decrease over the years switching on low-carbon sources and supporting electricity grids and battery storage. Besides, this would help to reduce the carbon intensity of power generation. The second option for decarbonization and for CO_2 emissions abatement is investing in the improvement rate of energy efficiency. Efficiency gains will make the overcited transition affordable but its improvement rate is lower than previous years, therefore it requires investments and new policies that will be able to no longer limit its gain.

According to IEA's Sustainable Development Scenario (SDS) efficiency and renewable sources would produce a reduction, in terms of emissions, equivalent to 37% and 32%, respectively [6] (Figure 1.4). Another option is indirect electrification that relies on the exploitation of H_2 and synthetic fuels. Green synthetic fuels are alternative fuels having the important role of facilitating the transition to low-carbon sources and reducing GHG emissions [7]. What makes synthetic fuels so attractive, is also the possibility to convert them into heat, by combustion, or electricity during peak loads by means of fuel cells ensuring the flexibility of the grid [8]. However, despite the measures aforementioned so far, a very important role is played by the application of Carbon Capture & Sequestration (CCS) technology.

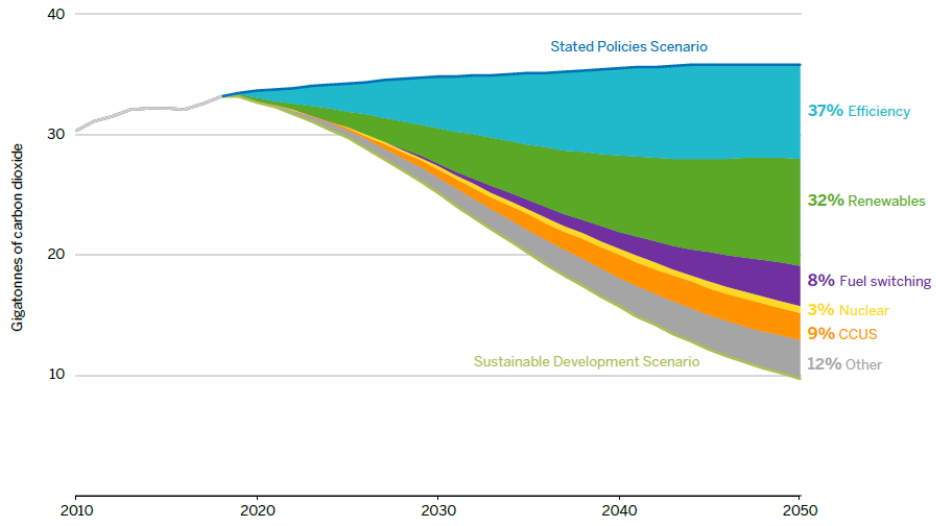

Source: IEA 2019a.
Note: Reduced thermal losses in power generation account for 15 percent of efficiency improvements.
CCUS = carbon capture, utilization, and storage.

Figure 1.4: *Additional reductions in CO2 emissions by measure under the SDS relative to the Stated Policies Scenario [6].*

Its contribution to the reduction of CO_2 emissions is realized especially in the field of power generation plants and in the industry sector. In particular, emissions from industries (cement, iron, steel industry, etc.) are mainly correlated to chemical and physical reactions, which make emissions difficult to be mitigated, since switching to alternative fuels would be irrelevant [9]. On the other hand, concerning the power plants, CCS may be a useful instrument from the point of view of enabling

continuous operation of existing power plants by retrofitting CO_2 capture equipment. The storage option has been one of the first to be considered and it is extensively studied and investigated in order to accumulate the captured carbon dioxide for future purposes instead of directly emitting it in the atmosphere. However, although it is ideally feasible, in practice it is impossible to store all the amount of CO_2 emitted from power plants in several geological formations (or depleted oil sites) involving challenges such as risks of leakage, high level of uncertainty, and prediction of plume migration. As alternative, the captured CO_2 can be re-used, exploiting the concept of Carbon Capture and Utilization (CCU). Carbon dioxide may be re-used in many ways: as technological fluid (solvent), by conversion to chemicals and synthetic fuels, and by mineralization to solid inorganic carbonates [10] (see Figure 1.5). The CO_2 conversion into synthetic fuels is an attractive and interesting path to focus on, since their use has been already mentioned above as a valid option for decarbonization. Among the routes of conversion the hydrogenation is one of the most important through which methanol is produced.

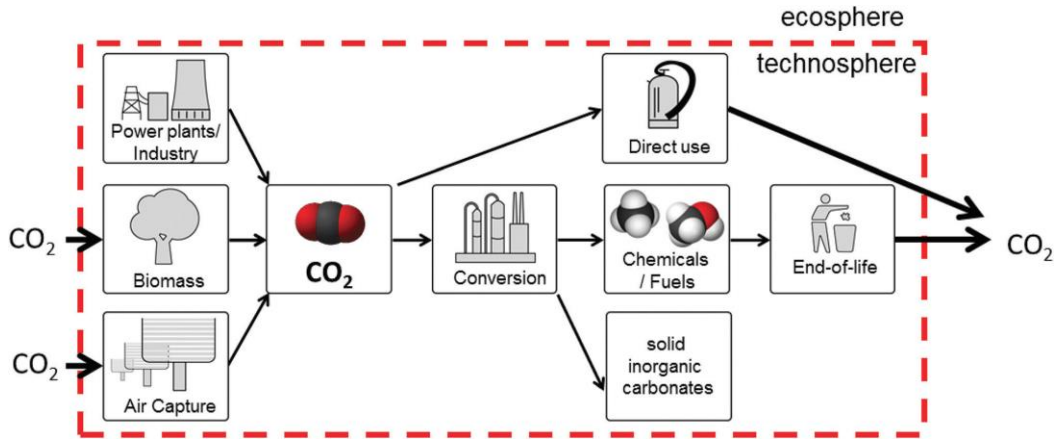

Figure 1.5: *Utilization pathways for carbon dioxide [10].*

Anyway, CO_2 can be re-used to produce syngas (synthetic gas); it is a fuel composed by a mixture of CO and H_2, both of them obtainable from the flue gases, in which CO_2 and H_2O are largely available, collected from power plants adopting carbon capture. Syngas has a central role in production of several chemicals (see Figure 1.6) such as overcited methanol, but aslo ethanol and especially dimethyl

ether (DME), a clear-burning fuel that represents a potential diesel substitute [11]. Obviously, the first step is to collect CO_2 and H_2O from the flue gases, secondly there is the dissociation driven by electricity or, alternatively, by thermal energy that can be obtained at a lower cost by converting solar energy.

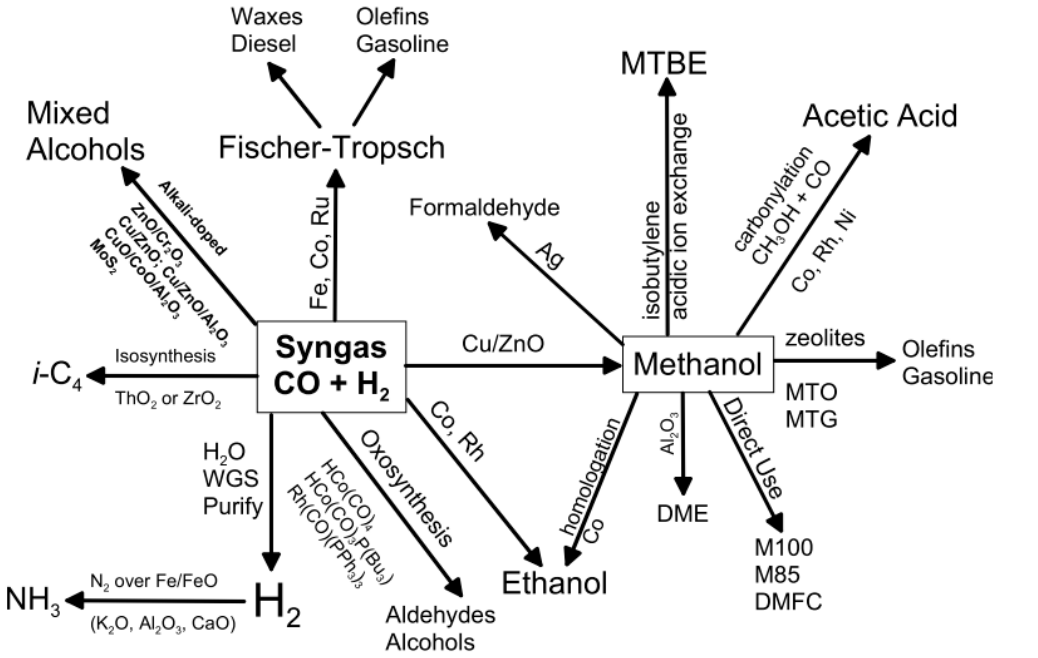

Figure 1.6: *Chemical production from syngas [12].*

To date, syngas is mainly produced by coal and biomass gasification, methane reforming, and cracking. Anyway, combining syngas production and solar thermal energy is a promising way to obtain a synthetic fuel ("solar fuel" in this case) by means of renewable sources. Solar thermal dissociation of CO_2 and/or H_2O can be achieved through different methods: thermolysis, thermochemical cycles, electrolysis, and photoelectrolysis (see Figure 1.7). Among these, thermochemical cycles combined with concentrated solar energy is the cheapest solution to produce syngas and it is becoming competitive with steam methane reforming (SMR), a well-known technology that has reached its maximum levels in efficiency and development, and, in addition, it makes use of fossil fuels as raw material, that is clearly a negative aspect from the point of view of GHG emissions.

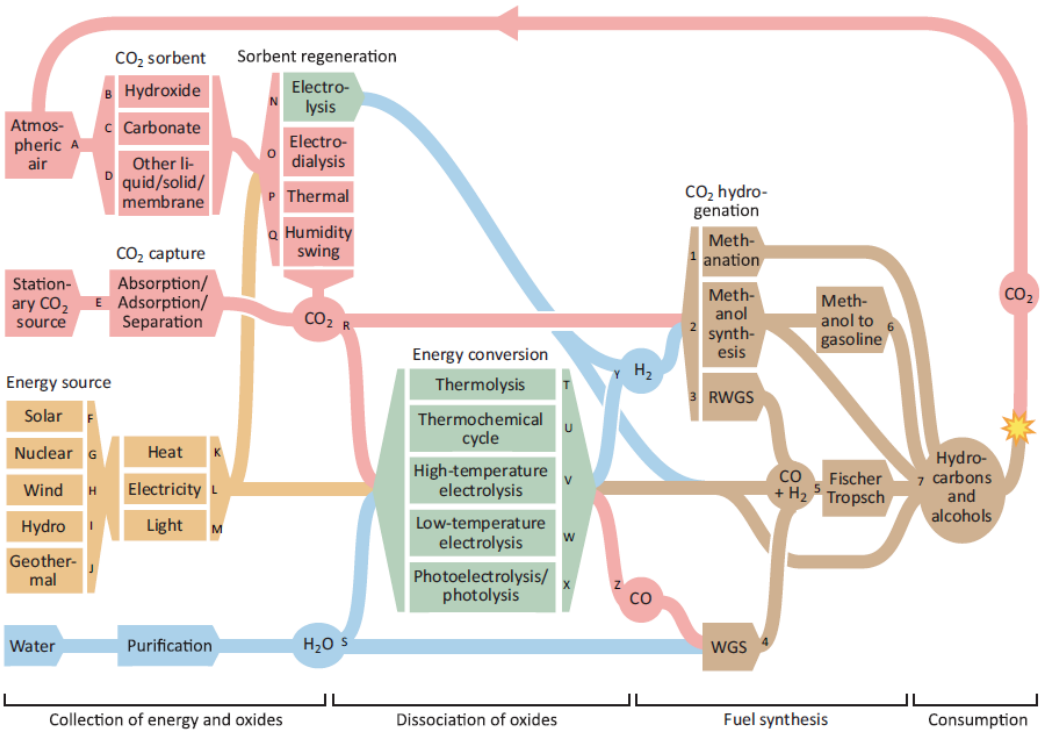

Figure 1.7: *All possible pathways from CO_2 and H_2O to hydrocarbon fuels [13].*

1.2 – Thermochemical processes for CO_2 re-use

Converting solar radiation into heat, by means of concentrated solar power (CSP), it is possible to reach high temperatures able to realize splitting of molecules in thermochemical cycles allowing production of solar fuels. There are two main thermochemical processes that avoid GHG emissions by exploiting renewable sources: thermolysis and thermochemical cycles (Figure 1.8). Solar thermolysis is a single-step direct thermal dissociation of H_2O/CO_2. It is conceptually the simplest way to dissociate H_2O/CO_2, being able to break chemical bonds and extract $\frac{1}{2}O_2$ [16]. Unfortunately, since the dissociation energy for breaking the C=O bond is around 750 kJ/mol, high energy is required, and a very high temperatures (above 2500 K), and this requirement makes this process not a viable option according to the technology available nowadays [17]. Furthermore, another drawback is the

issue of the separation of H2/CO and O2 in order to avoid production of any explosive mixture.

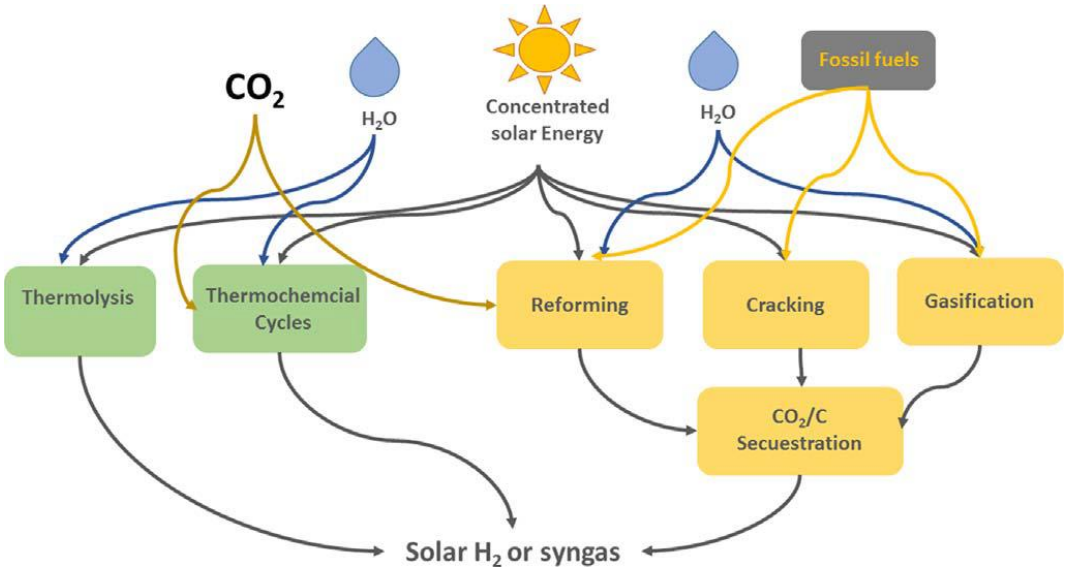

Figure 1.8: *Thermochemical solar routes for syngas production [14].*

On the other hand, thermochemical cycles are promising processes composed of two or three steps involving metal oxide redox reactions occurring at lower operating temperatures (800-2000 K). In a two-step thermochemical cycle, the oxygen carrier (metal oxide) undergoes a first thermal reduction (TR) reaction at high temperature (supplied by solar energy) followed by an oxidation reaction in which the metal oxide is re-oxidized by H_2O/CO_2. The TR step is endothermic and requires a higher valence metal oxide, in this step oxygen is released obtaining the reduced metal oxide. In the oxidation step (exothermic) the reduced oxygen carrier is oxidized back to the pristine oxide by taking oxygen from H_2O/CO_2 to form H_2/CO. Thus, the metal oxide is regenerated and recycled and re-used again unlike gasification or reforming [14]. Furthermore, two-step metal-oxide based thermochemical redox cycle bypasses the risk of explosive mixtures of products since O_2 is produced separately from the desired fuel. Several materials have been tested as oxygen carrier in order to maximize the syngas production, the conversion efficiency, and decrease the reduction temperature. Among the materials that showed the most promising results was found to be ferrites, ceria-based materials,

and perovskites. Nevertheless, a lot of work is still needed in order to enhance redox properties focusing on material structure and lattice, trying to modify it by doping and substitution of elements.

Chapter 2

2 - Literature review

2.1 – Carbon capture, storage, and utilization

Basically, the carbon capture process was suggested in the early 1970s, after the global crisis, to inject CO_2 in an oil field to boost its recovery [20]. However, this process has become significantly important, across a range of sectors (power plants, industries, etc.), making possible the emissions tackling and the transition toward net-zero emissions goal. Today, there are 21 CCUS facilities able to capture up to 40 Mt of CO_2 each year [21] (Figure 2.1).

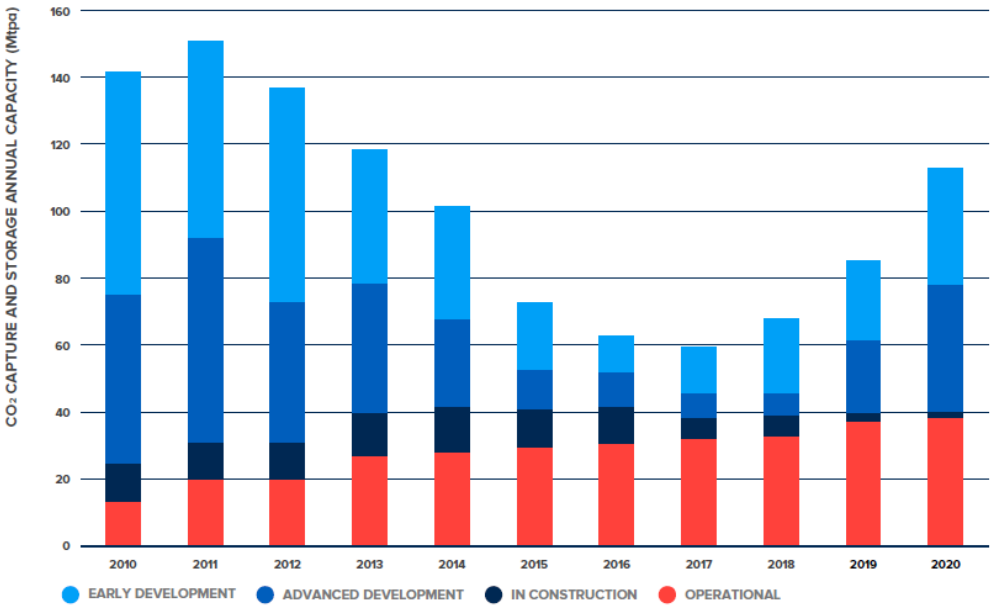

Figure 2.1: *Global CO_2 captured capacity [22].*

Anyway, according to target set by IEA in 2009, large-scale CCUS projects should have been developed in order to be able to store 300 $MtCO_2$ per year, by 2020 [21]. Therefore, it is obvious that the current data are far below the target, representing just 13%. This scenario is mainly due to lack of policy support and investments that affects the CCUS deployment, and thus its commercialization. In fact, the high cost of CCUS installation has always been one of the main challenges together with difficulties in integrating this technology with the other elements of the CO_2 supply chain. Nevertheless, the interest in CCUS has increased recently, leading to lower costs and policy support. Currently, there are 65 commercial CCUS facilities all over the world of which 21 in operating conditions, while the remainder are under development or under construction. CCUS consists of several steps: CO_2 capture, conditioning, transport, and storing. With regard to the first step of the chain, according to the phase in which CO_2 is captured, there are three viable paths: pre-combustion, oxy-fuel combustion, or post-combustion (Figure 2.2). In the pre-combustion process, CO_2 is removed before combustion takes place; it is mainly applied in power production systems and chemical industries and works with solid fuels (natural gas and coal) such as in Integrated Coal Gasification Combined Cycle (IGCC) [23].

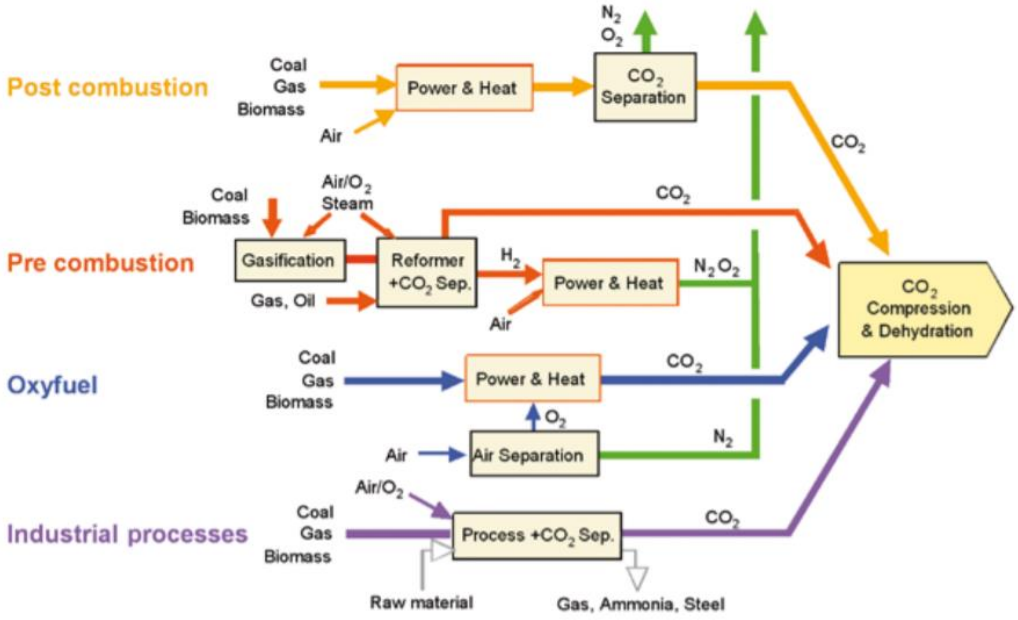

Figure 2.2: *CO_2 capture process and systems [27].*

Coal is gasified and converted into syngas (CO/H_2), CO_2 is produced starting from CO by means of the Water Gas Shift (WGS) reaction (reaction 2.1), finally CO_2 is separated from the hydrogen (via physical/chemical absorption or using a membrane [31,32]) that can be burned later as free-emissions fuel.

$$CO + H_2O \leftrightarrow H_2 + CO_2 \tag{2.1}$$

Furthermore, in the case of natural gas, the first step is steam reforming (reaction 2.2), then WGS reaction to produce CO_2 and enhance the H_2 content [24].

$$CH_4 + H_2O \leftrightarrow 3H_2 + CO \tag{2.2}$$

Post-combustion capture technologies separate CO_2 from the flues gas after the combustion is completed and it represent an effective option to retrofit existing fossil fuel power plants. One of the main challenges is the large parasitic load associated with the low CO_2 levels in post-combustion flue gas, due to the usage of air in the combustion [23]. This load is correlated to the energy consumption associated with the solvent regeneration [25] that is necessary for CO_2 capture. Furthermore, this type of capture shows high energy penalties, in fact many efforts are made with the aim of improving this technology. There are several methods available for CO_2 post-combustion capture, among these chemical absorption is widely used, the classical chemical absorbent is 20-30 wt% aqueous monoethanolamine (MEA) [10], it is a low-cost material and has quite good CO_2 transfer property, but it has also some drawbacks such as slight toxicity and thermal degradation issues. The chemical absorption process called “chemical wash” consists of counter-flow of gas to be solved with solvent in an absorption column (scrubber). Together with MEA there are other amine-based solvent such as MDEA, EDA, and amine blends (PZ/AMP, PZ/MDEA, MEA/MDEA). Anyway, it must be specified that multi-phase absorbents (liquid-solid, and liquid-liquid separation systems) represent another option for chemisorption. Unlike these methods, in which CO_2 separation is achieved via chemical reactions, physical absorption is based on CO_2 capture on the surface of a liquid solvent and it used when the concentration of CO_2 in flue gas exceed 15% vol. [26]. Furthermore, regarding chemical and petrochemical industries, pressure swing adsorption (PSA)

and cryogenic separation have been largely exploited. An alternative for post-combustion CO_2 capture is Calcium looping (CaL) technology (reaction 2.3):

$$CaCO_3 \leftrightarrow CaO + CO_2 \qquad \Delta H = -178\ kJ/mol \tag{2.3}$$

Limestone has the advantages of being largely available and low-cost with respect to MEA. Moreover, the spent sorbent may be reused for cement making processes [10]. Oxy-fuel combustion process is not based on absorption, the idea is to perform a combustion in which air is replaced by a stream of almost pure oxygen (> 95%). An air separation unit (ASU), upstream to combustion chamber, is needed in order to separate oxygen from N_2, thus, flue gas contains mainly CO_2, water and traces of other gases. The substitution of N_2 by CO_2 and water leads to the reduction of the flame speed [23] and to a reduced control of the adiabatic flame temperature, this make recirculation of exhausted gases necessary [28]. The main drawback in this scheme is the ASU which needs large amounts of energy to drive cryogenic air distillation, furthermore it is not efficient enough to be considered a competitive technology yet. Another method to obtain oxygen from an air stream, without cryogenic processes, is using ion transport membrane (ITMs) reactor in which a MIEC (mixed ionic and electronic conducting) conductor, able to conduct O^{2-} ions and e^-, is employed. Anyway it is still a high energy-requiring method since air need to be compressed up to 20 bar and heated up to 900°C in order to match the membrane operating conditions. Once CO_2 is captured it needs to be transported to the storage site and the most viable method for onshore transport is via pipeline. Anyway, also the transport by ship tanker is feasible and cost-competitive with pipelines in case of long distances [24]. To date, the majority of transportation occur via pipeline, CO_2 is compressed, before to be introduced in the ducts, up to a value that depends on the pressure drop along the pipeline and on the stream's composition, since some impurities (water and non-condensable gases) may remain in the captured CO_2. CO_2 storage in geological formations have received extensive consideration, but before to be implemented the formation has to be analyzed, especially in terms of thickness, depth, and rock permeability. Moreover, a risk assessment concerning CO_2 leakage is also required, in fact another important parameter regard the overlying cap rock in the geological formation evaluating

whether or not it provide an efficient sealing. To date, among the geological formations exploited there are deep saline formations, coal mines and depleted hydrocarbon fields. This last one has been used for decades in the USA allowing the oil recovery (enhanced oil recovery EOR) by injecting CO_2. Alternatively, deep ocean storage has been considered. Oceans cover the 70% of the Earth's surface and represent a natural CO_2 sink, so it has been thought that injecting CO_2 at a depth of more than 3 km could be a viable option for CO_2 storage. Furthermore, oceans would be able to keep the stored CO_2 for hundreds of years. Nevertheless there might be issues correlated to alteration of the marine ecosystem and to ocean acidification effects. The storage methods discussed so far have a huge potential but, on the other hand, they are limited by a finite global capacity in addition to various issues linked to the risks and to the economic expenditure. For this reason, alternatively to the storage option, another viable path is the utilization (CCU) through which CO_2 can be exploited and converted for the production of new chemicals and fuels. CCU is attractive thanks to its potential to mitigate climate change reducing emissions and depletion of resources and providing a path toward decarbonization of several sectors. CO_2 may be directly reused as raw material, for example in the food and drink industry it may be used as carbonating agent, preservative, and in the decaffeination process or in the pharmaceutical industry as intermediate in the synthesis of drugs [30]. Anyway the level of CO_2 amount directly reused cover only a small portion of the total CO_2 emitted every year, the only direct utilization would have a minimal impact on the emissions reduction. For this reason, CO_2 conversion is taken into account allowing the exploitation of CO_2 as precursor for organic compounds or for the production of chemicals and fuels. Anyway, initially the idea of converting CO_2 has been criticized since it would be stored temporarily in fuels and then released again in the atmosphere, furthermore it has been pointed out the difficulty in CO_2 conversion because of its high thermodynamic stability. Anyway, from recent studies, CCU has been recognized to play a vital role in mitigation and in reducing emissions in the next years. Summarizing, despite of the conversion difficulties and the amount of energy required to achieve it, CO_2 utilization remains a promising option that leads to the production of chemicals and fuels. Among the pathways available, the most

promising one is represented by the production of synthetic fuels by means of recycled CO_2, especially syngas that, as already stated, is a starting point for the production of numerous chemicals and can be used in multiple processes thanks to its versatility. In order to achieve this objective, namely the syngas production, CO_2 has to be dissociated and there are several ways that allow to reach this goal but among all of these methods the one that has received more interest in this work is the overcited chemical looping.

2.2 - CO_2 utilization in chemical looping and other dissociation processes

Synthetic gas generation can follow several routes and there are basically two classes of methods available: electrochemical and thermochemical processes. In order to be consistent with the mitigation objective, all the methods that will be reviewed below are supported by renewable sources. The first option for electrochemical transformation of CO_2/H_2O into value-added products is the electrolysis. This process consists in the splitting of the starting molecules through the application of an external electric potential. Pelayo Garcia de Arquer in his study [33] presents a hybrid catalyst that enables efficient CO_2 and CO gas-phase electrolysis at a current densities higher than 1 A/cm^2. Another study made by Severin Foit [34] shows electrochemical reduction of CO_2 to CO on ceramic solid oxide cells (SOECs) at different operating temperatures, loads and flow rates. The optimal temperature for the direct CO_2 electrolysis was found to be around 800-850°C, imposing an external potential of 1.1 V. Furthermore, SOEC performs better than the other electrolyzers such as alkaline electrolytic cell (AEC) and proton exchange membrane electrolytic cell (PEMEC) because it requires a lower voltage and allows to perform co-electrolysis of both CO_2 and H_2O (reaction 2.4, 2.5) by sending a mixture of the two at the cathode obtaining syngas as final product.

$$H_2O + 2e^- \leftrightarrow H_2 + O^{2-} \quad (2.4)$$

$$CO_2 + 2e^- \leftrightarrow CO + O^{2-} \quad (2.5)$$

Anyway, solid oxide electrolyzers require further development in terms of degradation due to the high operating temperature, and they need more stable materials. An electrochemical alternative to electrolysis are photochemical cells (PECs) which are based on the solar energy exploitation (Figure 2.3). PEC consists of a photo-electrode immersed into an electrolyte solution, and of p-type and n-type semiconductors that acts as photocathodes and anodes, respectively. Under solar irradiation, electrons and holes are generated in the semiconductor at the conduction band (CB) and valence band (VB), respectively [35]. The band bending is the phenomenon that allow to enhance CO_2 conversion by separating electrons and holes at the interface between electrode and electrolyte. The upward band bending occurs at the interface for n-type, viceversa, the downward band bending occurs for p-type.

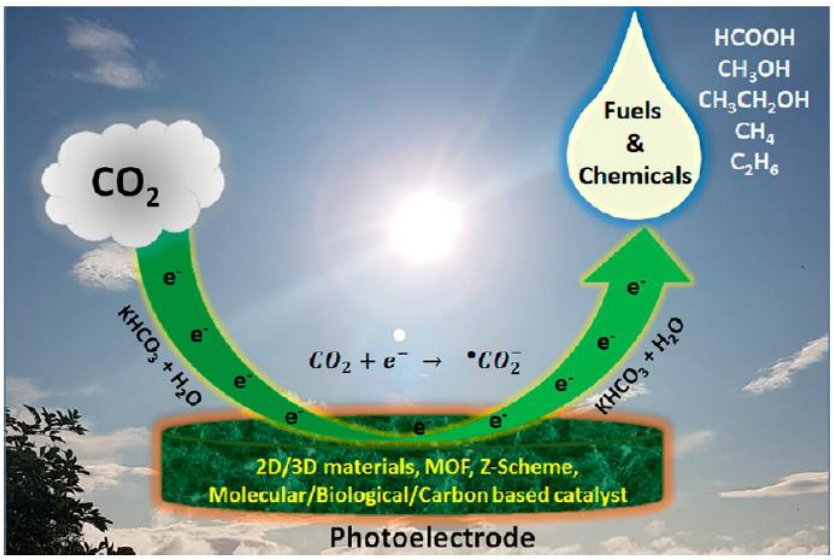

Figure 2.3: *PEC CO_2 conversion into value-added products [35].*

The intermediate product of this process is CO_2^-, and starting from it *CO*, formic acid (*HCOOC*), methanol (CH_3OH), methane (CH_4), etc. can be produced. PEC represents a feasible method to use renewable sources in order to achieve CO_2 conversion and enhancement however further research activities are necessary in

order to obtain suitable performances for large-scale production. As already said, electrochemical path is only one of the viable options, thermochemical route is the other attractive method to convert CO_2 and it encompasses several processes (Figure 2.4). Solar thermochemical processes can be used in various sectors allowing the production of several products. For example, solar thermochemical process may be employed in metal and cement industries, in the production of lime and ammonia, and it represents a means for upgrading organic waste and landfill gases. On the other hand, besides chemicals, exploitation of solar thermochemical cycles is promising in the field of hydrogen, carbon monoxide, and syngas production. Regarding the production of solar fuels, thermolysis and thermochemical cycles are the primary choices.

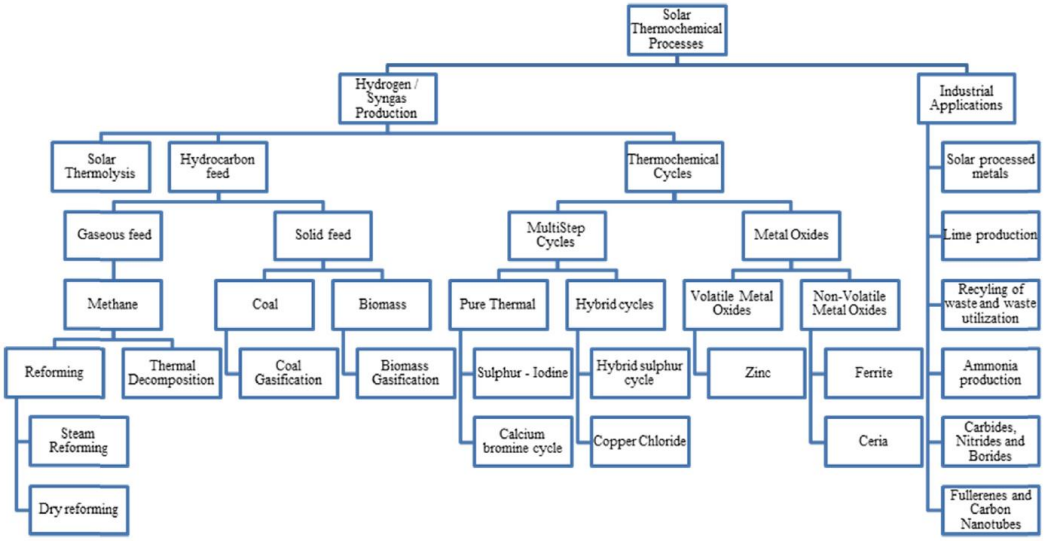

Figure 2.4: *Classification of solar thermochemical processes [17].*

Solar thermolysis, as already stated in the previous chapter, is based on the direct dissociation of CO_2 at temperature up to 2500 K in order to achieve a high bond-dissociation energy able to break the C=O bond. The direct dissociation of CO_2 and H_2 is based on endothermic reactions:

$$CO_2 \leftrightarrow CO + \frac{1}{2}O_2 \tag{2.6}$$

$$H_2O \leftrightarrow H_2 + \frac{1}{2}O_2 \tag{2.7}$$

Among these two reactions, the CO_2 dissociation is more thermodynamically favorable, and the production of CO is favored with increasing temperature and decreasing O_2 partial pressure. In the study of Maria Tou [36] the experimental setup consists of a reactor for co-thermolysis of CO_2 and H_2O in which a tubular ceria membrane is employed (Figure 2.5). In this study was reached a CO_2 production rate of 1.7 μmol/min/cm^2 at a maximum temperature of 1873 K. Anyway, the requirement of high temperatures and the final quenching needed for CO/H_2 separation from O_2 avoiding explosive mixture represent great drawbacks. Alternatively to thermolysis, thermochemical cycle route is a more feasible and cheaper way to produce syngas and to convert emitted CO_2 to CO. Chemical looping process address the two major problems correlated to thermolysis: separation of produced gases and reduction of the operating temperature necessary for the splitting of CO_2.

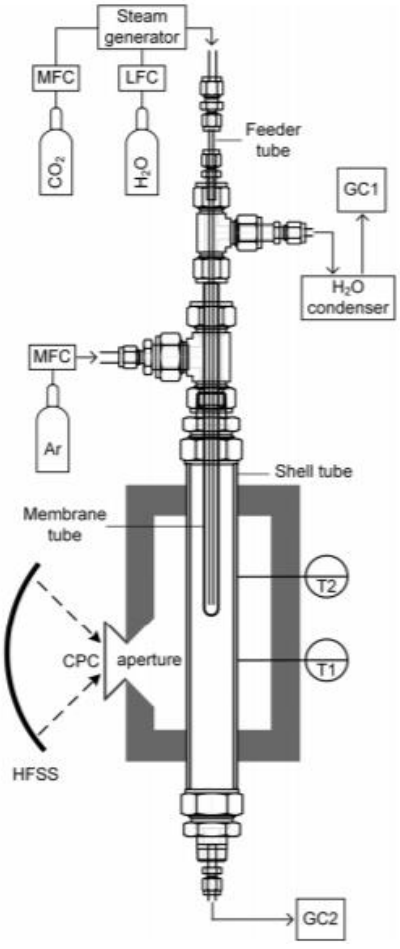

Figure 2.5: *Experimental set-up for direct CO_2 dissociation [36].*

2.2.1 - Chemical looping applications

Chemical looping is based on several steps in which various chemical reactions occur and the oxygen carrier, that acts as one of the reactants, is circulated in a closed loop composed by distinct reactors. The oxygen carrier (typically metal oxide), by recirculating, undergoes oxidation and reduction reactions, in which it is re-generated and it alternates between different oxidation states. These cycles generally operate at lower temperatures (800-1600 K) and are composed of two or three steps [3]. In the case of three reactors configuration, multi-step thermochemical cycles have been initially used for hydrogen production supplying heat with a nuclear reactor. The temperature was limited to 1000 K since it was the set value for the high temperature gas cooled reactors (HTGR). Due to this thermodynamic limitation, three reactors were the minimum that allowed to achieve a feasible hydrogen production. Obviously, not only nuclear reactors can act as heat source but also solar energy can be exploited in order to perform the process such as in the case of sulphur-iodine (S-I) cycle (Figure 2.6). The first step is the endothermic sulphuric acid decomposition in which oxygen and aqueous SO_2 are produced. In the second step the exothermic Bunsen reaction occurs, and finally the last step is HI decomposition in which hydrogen is produced [37].

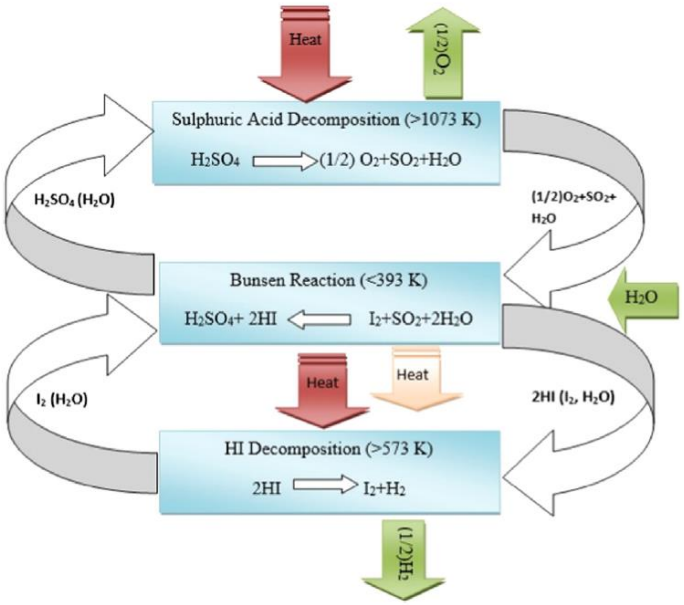

***Figure 2.6**: Sulphur-iodine cycle scheme [17].*

Regarding chemical looping in which an oxygen carrier is continuously recirculated, an example with three reactors configuration is reported in Figure 2.7. In the fuel reactor CH_4 is converted into CO_2 and H_2O (combustion products) and Fe_2O_3 is reduced to FeO that reacts with steam in the steam reactor to produce hydrogen and Fe_3O_4. Finally, in the air reactor Fe_3O_4 is converted to Fe_2O_3 reacting with oxygen supplied by an air stream. The iron-based oxygen carrier cannot recirculates endlessly performing always at the same way, in fact as the number of cycles increases the material loses efficiency and leakage may also occur in the system, so generally a step for the make-up of the reactant is inserted upstream of the steam reactor.

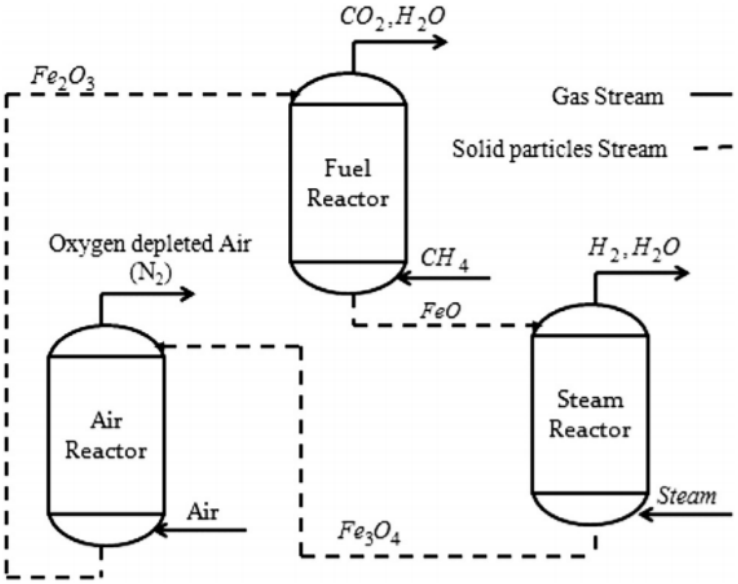

Figure 2.7: *Iron-based oxygen carrier in three chemical looping reactors [38].*

This type of configuration and this redox material are used in the case of syngas chemical looping process, in this case a counter-current moving bed fuel reactor is used for CO_2 capture, a second counter-current moving bed reactor is used as oxidizer and lead to the production of hydrogen, finally a dense fluidized bed air reactor is used for the regeneration of the redox material [40]. Anyway, multi-step thermochemical cycles present several issues such as the occurrence of more reactions that take place at different temperature levels, so it is difficult to be integrated in other processes. The alternative is the two-step thermochemical cycle

process in which oxidation and reduction reactions occur in two different reactors, respectively. Generally the endothermic reduction reaction requires higher temperatures than the exothermic oxidation one, this introduces a temperature swing between the two reactors. Anyway there are some cases in which it is possible to perform the cycle in a more convenient isothermal condition without the need of varying the operating temperature between the reduction and oxidation reactors. Depending on the type of process and the type of reactor used, chemical looping can have various configurations and numerous applications. For example, using a counter-current moving bed fuel reactor it is possible to convert the fuel to CO_2 and H_2O. One of the options is to perform a coal direct chemical looping process (CDCL) [39] that represents a technology for CO_2 capture similar to oxy-combustion one but with the advantage of not requiring a pure steam of oxygen, therefore without requiring an air separation unit (ASU). On the other hand, in case of co-current moving bed fuel reactor, it is possible to perform the coal to syngas chemical looping process (CTSCL). The chemical looping consists of two reactor, a co-current moving bed fuel reactor for producing syngas and a fluidized bed air reactor for the oxygen carrier regeneration. Bubbling fluidized beds and circulating fluidized beds may be another viable option for chemical looping processes, in fact a single loop chemical looping combustion process with bubbling fluidized bed reactors is similar to commercial fluid catalytic crackers (FCCs) [40]. Both the processes present similar components like two bubbling fluidized bed reactors and

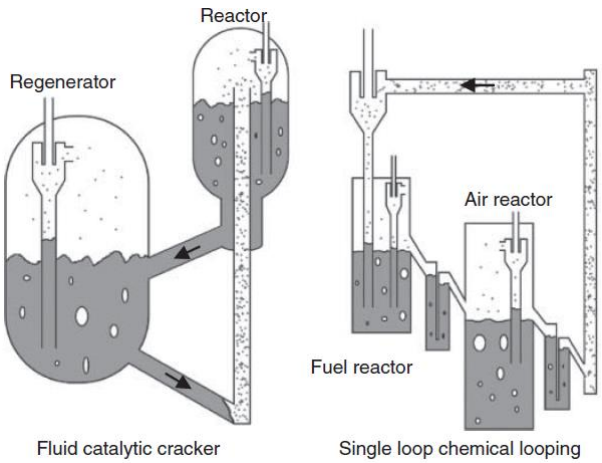

Figure 2.8: *Comparison between a fluid catalytic reactor and a single loop chemical looping [40].*

a riser (Figure 2.8). During the process, the catalyst is recirculated between the fuel reactor in which allows fuel cracking or oxidation, and the regenerator in which it is, in point, regenerated. A further way to apply chemical looping technology is by means of packed bed reactors (PBR). In this case the solid redox material remain stationary instead of circulating between two reactors, on the other hand what varies is the gas flow composition between oxidation and reduction steps. Chemical looping combustion (CLC) process is a promising method for fuel decarbonization and it can be based on packed bed reactors in which the oxygen carrier generally is first oxidized using air stream and then reduced with a fuel. Differently from previous systems, in this type of process the oxygen needed for the combustion step is transported by the oxidized oxygen carrier instead of being introduced directly through an external air or oxygen stream, thus circumventing the air separation requirement. This method is conceptually quite similar to the chemical looping process used in this work, anyway the objective for CLC is to decarbonize the fuel emitting CO_2 and then separating it from the flue gases [41]. Finally, another process involving packed bed reactors that represents a variant of CLC is the chemical looping with oxygen uncoupling (CLOU). In this type of processes the oxygen is released from the oxygen carrier in the fuel reactor and then can be provided for the fuel combustion reaction, as shown below in Figure 2.9.

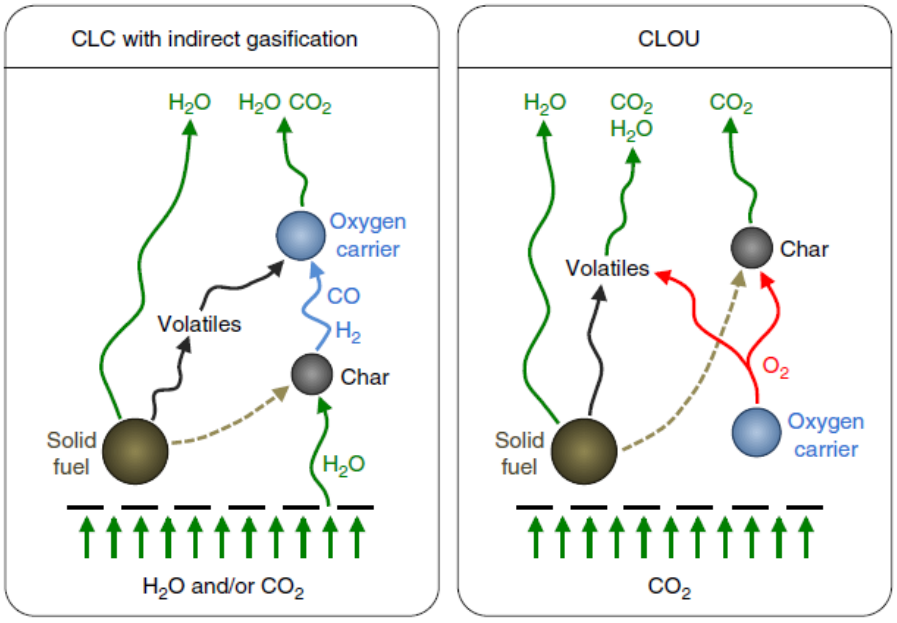

Figure 2.9: *Differences between CLC and CLOU processes [40].*

2.3 – Chemical looping for CO_2 and H_2O dissociation

Chemical looping employed for CO_2 and H_2O dissociation allows the production of CO and H_2, thus these processes are very promising for syngas production. Generally the best-known configuration is the two-reactor setup in which a metal-oxide is recirculated as redox material. The two interconnected reactors form a closed loop, the metal oxide is first reduced at high temperature (>1300°C) in the reduction reactor allowing the oxygen release with consequent formation of oxygen vacancy in the matrix, subsequently the reduced metal oxide is re-oxidized in the oxidation reactor at lower temperature (around 1000°C) using CO_2 or H_2O. In this work for the reduction reaction has been used H_2 as reducing agent and CO_2 as oxidizing agent. The vacancies creation is the phenomenon that make this process feasible, obviously the ability of generating oxygen vacancies depends on the material properties and on its morphological structure. Regarding the thermal reduction step, it is favorite at high operating temperature and low oxygen partial pressure (vacuum conditions), on the other hand opposite conditions are favorable for the oxidation reaction, so according to these requirements there would be a pressure and a temperature swing between the two reactors. Anyway, it is possible to make the process easier in terms of operating conditions in fact with a reducing fuel the pressure can be maintained at around environment conditions, furthermore in a reducing environment it is also possible to lower the reduction temperature up to reaching the oxidation temperature level. As already stated, since a high temperature is needed for the endothermic reduction reaction the chemical looping process integration with solar thermal energy is extremely promising in order to split CO_2 and H_2O. The respective reactions are listed below:

$$Thermal\ reduction\ (TR):\ MeO_x \rightarrow MeO_{x-\delta} + \frac{1}{2}O_2 \tag{2.8}$$

$$Water-splitting\ (WS):\ MeO_{x-\delta} + \delta H_2O \rightarrow MeO_x + \delta H_2 \tag{2.9a}$$

$$CO_2-splitting\ (CDS):\ MeO_{x-\delta} + \delta CO_2 \rightarrow MeO_x + \delta CO \tag{2.9b}$$

Chemical looping reforming (CLR) [42] is a viable technology for decreasing the reduction temperature, thereby reducing the temperature swing between the two

reactors. A suitable oxygen carrier is used to convert methane to syngas in the first step (reaction 2.10) at 800-1500°C, then the oxygen carrier oxidation step is generally carried out with steam and/or carbon dioxide (reaction 2.9a,b) producing hydrogen and carbon monoxide, respectively (Figure 2.10).

$$MeO_x + \delta CH_4 \rightarrow MeO_{x-\delta} + \delta(CO + 2H_2) \qquad (2.10)$$

In the work of Zhu et al. [43] it was reported a chemical looping steam methane reforming using Fe_2O_3 and CeO_2 as oxygen carrier. It was pointed out that Fe_2O_3 has a low reducibility, on the other hand CeO_2 has a more favorable performance in methane conversion but the reactivity could be enhanced by doping. For this reason a $CeO_2 - Fe_2O_3$ sample was prepared, it was shown a highest oxygen storage capacity, furthermore the interaction Ce-Fe implied good oxygen mobility. CH_4-IR (isothermal reduction) was performed in a fixed-bed reactor at 850°C with a flow composition of 5% CH_4 in N_2 (100 cm^3/min) for a fresh sample and for two other samples which had already been subjected to 1 and 10 cycles, respectively. It was noticed that samples with lower concentrations of surface oxygen produced less CO_2, furthermore as the number of cycles increased the area of the *CO* peak increased as well, since the recycled samples exhibited a favorable oxygen mobility.

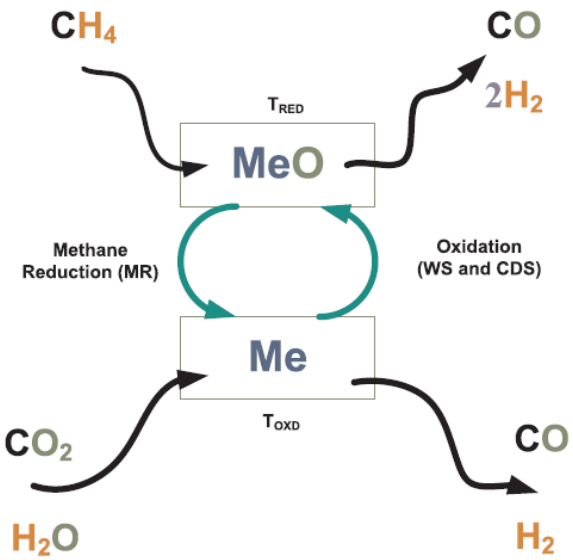

Figure 2.10: *Schematic of chemical looping reforming (CLR) [47].*

In the Ryden's work [45] $La_xSr_{1-x}Fe_yCo_{1-y}O_{3-\delta}$ was investigated as oxygen carrier in a CLR process. Several samples were synthetized as $La_{0.8}Sr_{0.2}FeO_{3-\delta}$ and $La_{0.5}Sr_{0.5}FeO_{3-\delta}$, the first one provided high conversion of methane and high selectivity towards *CO* and H_2 but increasing the methane flow the CH_4 conversion decreased substantially. $La_{0.5}Sr_{0.5}FeO_{3-\delta}$ showed a lower reactivity and selectivity towards *CO* and H_2. Anyway other materials have been tested such as $NiO/MgAl_2O_4$ that caused early formation of solid carbon, and $Fe_2O_3/MgAl_2O_4$ that with additional NiO exhibits the enhancement of both reactivity and selectivity towards *CO* and H_2. This result show that Ni is an excellent catalyst and this is one of the reasons why it has been used also as dopant for SFNM perovskites in the present work. One of the main drawbacks of CLR process is the occurrence of carbon deposition reaction which places a limit on the operating condition. This phenomenon occurs in the reduction reactor through two different reactions: Boudouard reaction (reaction 2.11) and methane dissociation reaction (reaction 2.12):

$$2CO \rightarrow C(s) + CO_2 \tag{2.11}$$

$$CH_4 \rightarrow C(s) + 2H_2 \tag{2.12}$$

The produced carbon follows the reduced metal-oxide in the oxidation reactor and here it reacts with CO_2 and H_2O according to the reactions 2.13 and 2.14.

$$C(s) + H_2O \rightarrow CO + H_2 \tag{2.13}$$

$$C(s) + CO_2 \rightarrow 2CO \tag{2.14}$$

These two reactions, that lead to syngas production, compete with the reduced oxygen carrier oxidation lowering its utilization and preventing its re-oxidation. Anyway, CLR method has been developed to circumvent some other issues related to the conventional steam methane reforming (SMR) process that has been the main process for the industrial hydrogen production in the last decades [44]. SMR is based on the reaction 2.2 and on the reaction 2.1 that represents the water gas shift (WGS) reaction. WGS reaction is generally divided in two steps: one at high temperature (350°C) in which *CO* is converted in order to produce H_2, then another

one at low temperature (200°C) where the *CO* content is further reduced obtaining a H_2-rich stream. Anyway SMR, as already said, has several issues regarding especially two processes, namely, water gas shift (WGS) reaction and pressure swing adsorption (PSA) (the final clean-up process) that are very energy consuming and represent a remarkable drawback. The direct alternative to SMR is the dry reforming process (reaction 2.15):

$$CH_4 + CO_2 \rightarrow 2CO + 2H_2 \quad (2.15)$$

This reaction requires higher temperature but it represents an attractive option for carbon capture.

2.4 – Oxygen carriers

Several redox material have been extensively investigated for thermochemical cycles involving CO_2/H_2O splitting reactions. Generally metal oxides represent a promising option for chemical looping processes being able to exhibit different oxidation states within the redox reactions. This characteristic allows metal oxides to alternately release oxygen during the reduction step and to promote CO_2/H_2O splitting during oxidation reaction. Basically, there are two classes of oxygen carrier characterized by their physical phase in reduced conditions. "Non-volatile" oxygen carriers remain in the solid state throughout the entire process, on the other hand "volatile" oxygen carriers exhibit a transition to gas phase during the reduction step.

2.4.1 – Volatile oxygen carriers

In this class of materials, the solid-to-gas transition during reduction step is provoked by the high reduction temperature required to achieve CO_2/H_2O splitting. This means that generally the reduction temperature exceeds the boiling temperature of metal-oxide employed in the process causing the above mentioned transition to gas phase. This aspect has a positive repercussion since it allows to obtain a high entropy gain favoring thermodynamically the process. On the other

hand, it is challenging since it implies several issues such as the necessity of a fast cooling after the reduction step in order to prevent recombination between released oxygen and the reduced metal oxide [18]. This is the main problem for volatile oxygen carriers cycles. In this class of materials one of the most famous application is *ZnO/Zn* cycle (Figure 2.11), it has been initially investigated mainly for H_2O splitting (WS), while CO_2 splitting (CDS) has been studied recently. ZnO decomposes approximately at around 2300 K and has a boiling temperature of 1180 K [15]. The reaction ΔG approaches the zero at 2235 K [47] and it is a further demonstration of the high endothermicity of the zinc oxide dissociation (reaction 2.16).

$$ZnO \rightarrow Zn + \frac{1}{2}O_2 \tag{2.16}$$

The next step of the cycle, WS (reaction 2.17) or CDS (reaction 2.18), is exothermic and generally takes place at temperatures lower than 1400 K producing H_2 and CO, respectively.

$$Zn + H_2O \rightarrow ZnO + H_2 \tag{2.17}$$

$$Zn + CO_2 \rightarrow ZnO + CO \tag{2.18}$$

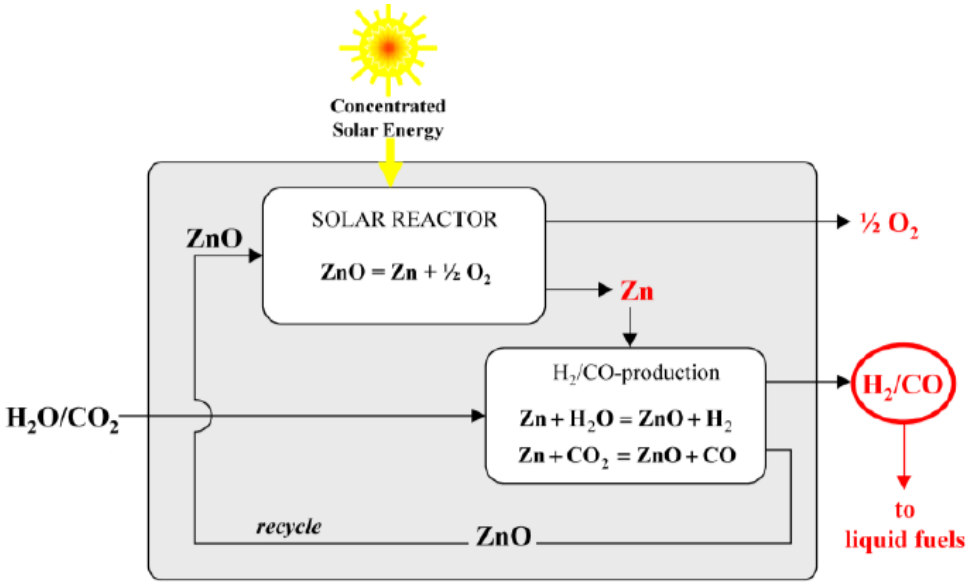

Figure 2.11: *Zn/ZnO two step thermochemical cycle [48].*

Several studies focused on Zn/ZnO oxygen carrier for different purposes (e.g. biomass gasification, syngas production, etc.) in various reactor systems (Figure 2.12) [48, 49, 50]. Although *Zn* is characterized by good thermodynamic properties (e.g. high reaction entropy gain and high energy density content), the energy efficiency of the process is heavily affected by the recombination of oxygen and metallic *Zn*(g) and by the quenching requirement. Another option is *CdO/Cd* cycle, it was first studied in the '80s and then reconsidered recently by General Atomics and University of Nevada [51]. The reducing step occurs at 1423-1723 K, the following oxidation step was tested using H_2O, anyway the entire cycle process has never been demonstrated under real-world conditions [15]. An alternative to *ZnO* was found in SnO_2/SnO redox material. It requires a reduction temperature around 1900 K and an oxidation temperature of 900 K, therefore it presents the same recombination problems already discussed.

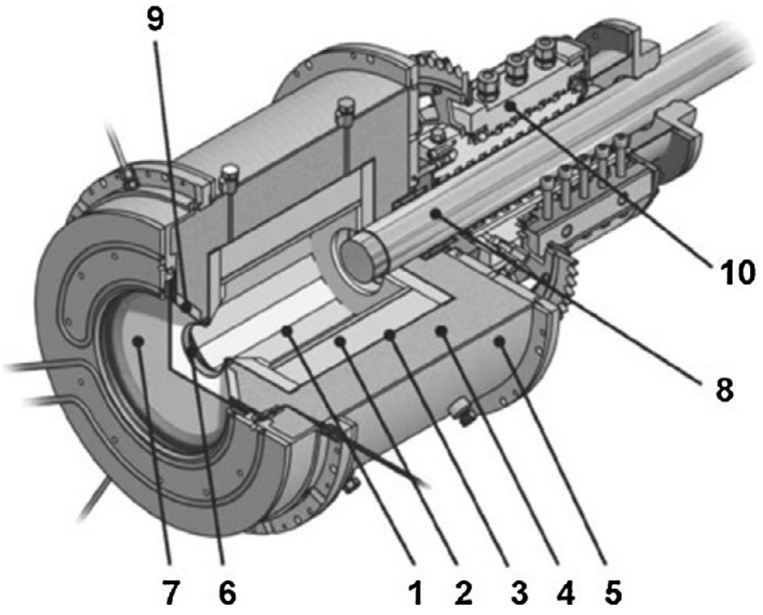

Figure 2.12: *Schematic of ZIRRUS solar reactor for ZnO dissociation [54]: (1) quartz window, (2) cavity aperture, (3) conical frustum, (4) reaction cavity, (5)* Al_2O_3/SiO_2 *insulation, (6) rotary joint, (7) quench unit.*

However, SnO exhibits lower reactivity with oxygen, with respect to *Zn*, in the high temperature reduction conditions. Chambon et al. [52] studied the hydrolysis reaction for *SnO* and *Zn* obtained from thermal dissociation of SnO_2 and *ZnO* in a moving front solar reactor. It was found out that H_2 yield for *Zn* was only 55%

while for SnO it was almost complete, even if the hydrolysis resulted slower. Finally, the last redox pair material that will be analyzed and that belongs to "volatile" oxygen carrier class is GeO_2/GeO. Kan et al. [53] demonstrated that, although the reduction of GeO_2 occurs at lower temperature (>1673 K) than SnO_2 dissociation, it was noticed the disproportionation of *GeO* into *Ge* and GeO_2 during the fast cooling step. Despite the numerous studies on this class of materials, the issues correlated to recombination and quenching suggested to investigate in another direction, taking into account other oxygen carriers.

2.4.2 – Non-volatile oxygen carriers

Differently from the previous class of materials, "non-volatile" redox materials remain in solid state throughout the chemical looping process avoiding the recombination issues correlated to the phase-change materials quenching step. Since the oxygen carrier does not exhibit a phase change, its characteristics such as particle size, porosity, and specific surface area are fundamental especially for the oxidation reaction. Non-volatile redox material exhibits change in crystal structure when subjected to reduction and oxidation reactions, but they have lower storage capacity with respect to volatile oxygen carriers, as reported by Bulfin et al. [55] (Figure 2.13). Fe_3O_4/FeO is one of the most studied and investigated non-volatile redox pair and was considered in order to decrease the solar thermal reduction temperature. The magnetite/wustite (Fe_3O_4/FeO) cycle was proposed for the first time in 1977 by Nakamura [56]. In the subsequent decades, magnetite has been exploited in the chemical looping process for H_2O and CO_2 dissociation. Fe_3O_4 thermal reduction (reaction 2.19) occurs at around 1600 K, whereas the oxidation step (reaction 2.20) is thermodynamically favored at lower temperature (up to 1200 K).

$$Fe_3O_4 \rightarrow 3FeO + \frac{1}{2}O_2 \tag{2.19}$$

$$3FeO + H_2O \rightarrow Fe_3O_4 + H_2 \tag{2.20}$$

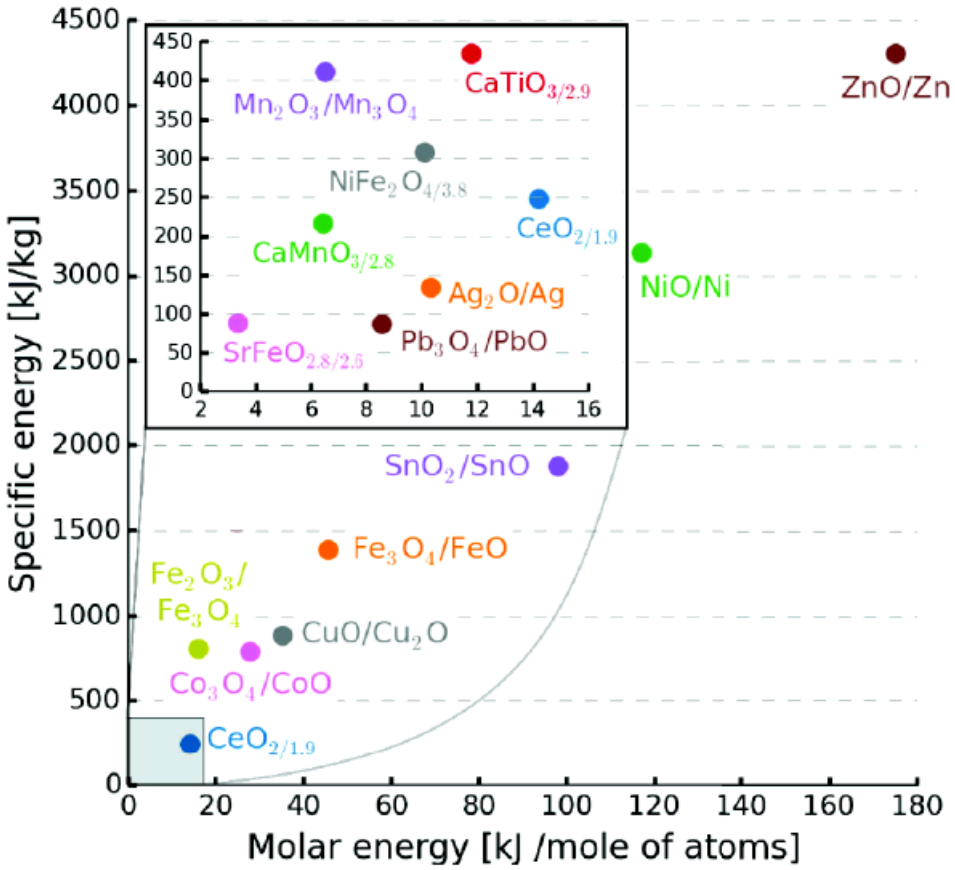

Figure 2.13: *Specific energy storage of oxygen carriers vs. the atomic molar energy storage [55].*

Iron oxides has been employed for several application, such as CLC, but in those cases, unlike two-step cycles, three reactors configuration was used and the oxide was fully reoxidized to hematite (Fe_2O_3). Anyway, the reduction temperature represent still a strong limitation for this material, in fact it affects the performance of the process causing sintering of the oxide that results in smaller particle size. A reduced particles size represents a negative aspect because it implies a consequent reduction of the H_2/CO yield. For these reasons it would be preferable to decrease the reduction temperature. The oxygen partial pressure reduction would be one of the viable methods to lower the reduction temperature and can be achieved by employing a vacuum pump that results in high energy consumption and thus in an increasing fuel produced cost. Alternatively, the iron-based oxide can be doped with other materials allowing the temperature reduction lowering and avoiding sintering phenomena. Some authors demonstrated a two-step water-splitting cycle using

Fe_3O_4 supported on monoclinic ZrO_2 (m- ZrO_2) [58, 59] that has a higher melting point. It resulted in a reduction of sintering effects that permitted the cyclability of the material in a temperature range of 1000-1400°C. Later, Fe_3O_4 supported on cubic yttria stabilized zirconia ($Fe_3O_4/c-YSZ$) was considered as a further option [59] exhibiting a higher stability than m-ZrO_2 for cyclic reactions. Furthermore, it was noticed the formation of a reactive Fe-containing cubic zirconia that was able to perform the water-splitting at less than 1400°C. Gokon et al. [60] examined $NiFe_2O_4/m-ZrO_2$ and $Fe_3O_4/m-ZrO_2$ in a thermochemical two-step water-splitting cycle with reduction temperature of 1400°C and oxidation temperature of 1000°C. It was noticed that the first sample led to a higher production of hydrogen (0.47 μmol/g) if compared to the second one (0.31 μmol/g). The same authors developed a ceramic foam with a matrix made of MgO-partially stabilized zirconia (MPSZ) [61]. They examined $NiFe_2O_4/m-ZrO_2/MPSZ$ and $Fe_3O_4/m-ZrO_2/MPSZ$ using an experimental apparatus shown in Figure 2.14. The hydrogen production for $NiFe_2O_4/m-ZrO_2/MPSZ$ and $Fe_3O_4/m-ZrO_2/MPSZ$ was found to be 2.3-3.3 Ncm^3/g and 2.4-2.9 Ncm^3/g, respectively. Anyway, iron based thermochemical cycle has several issues like sintering and low hydrogen production rates. Among all investigated nonvolatile oxygen carriers, CeO_2 represents the state-of-the-art redox material thanks to its thermodynamic and physico-chemical properties: slight effect of sintering at high temperature, fast kinetics, structural stability, and mechanical strength.

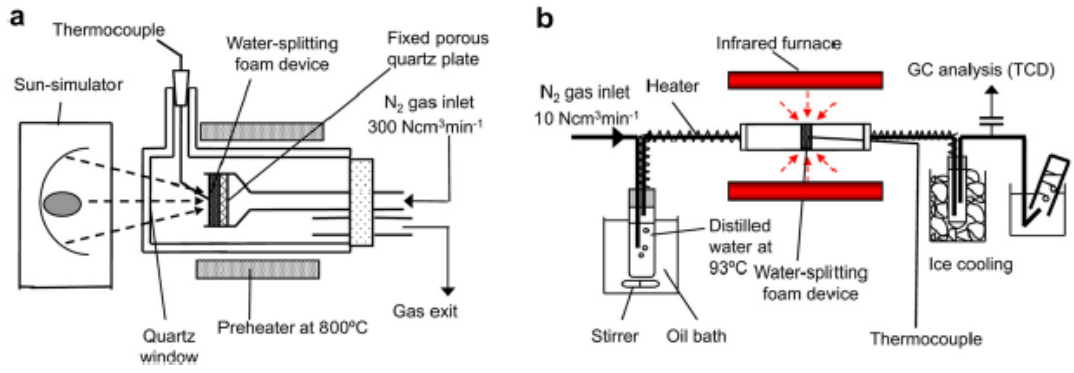

Figure 2.14: *Experimental setup for (a) TR step and for (b) water-decomposition [61].*

The stoichiometric reduction (reaction 2.21) from Ce^{4+} to Ce^{3+} requires elevated temperature level (up to 2300 K) [62], anyway this thermal requirement is quite prohibitive and various searches focused on lower temperatures (above 1500 °C) preferring non-stoichiometric reduction (reaction 2.22).

$$2CeO_2 \rightarrow Ce_2O_3 + 0.5O_2 \quad (2.21)$$

$$CeO_{2-\delta_{ox}} \rightarrow CeO_{2-\delta_{red}} + \left(\frac{\delta_{red}-\delta_{ox}}{2}\right) O_2 \quad (2.22)$$

The reduction is then followed by water and/or carbon dioxide splitting (reaction 2.23 and 2.24) that occurs between 600 and 1000°C (Figure 2.15).

$$CeO_{2-\delta_{red}} + (\delta_{red} - \delta_{ox})H_2O \rightarrow CeO_{2-\delta_{ox}} + (\delta_{red} - \delta_{ox})H_2 \quad (2.23)$$

$$CeO_{2-\delta_{red}} + (\delta_{red} - \delta_{ox})CO_2 \rightarrow CeO_{2-\delta_{ox}} + (\delta_{red} - \delta_{ox})CO \quad (2.24)$$

δ_{ox} represents the nonstoichiometry after the oxidation, while δ_{red} represents the nonstoichiometry after reduction, and the value of their difference identify the amount of fuel that can be produced per mol of CeO_2. Furthermore, CeO_2 has a high oxygen diffusion coefficient [63] and a remarkable entropy change, linked to oxygen exchange, leading to a lower temperature difference among oxidation and reduction reactions. CeO_2 has been extensively studied and investigated in several solar reactors, and during this investigation process the samples were modified trying to find the best structure to avoid limitations related to reactors technology. For example in the work of Chueh et al. [64] a porous monolithic ceria cylinder was used in a thermally insulated cavity obtaining an efficiency (ratio of output fuel energy to total input energy) reached average values around 0.4% caused mainly by re-radiation losses from the reactor. Later, Furler et al. [65] used porous ceria felt in the same type of reactor obtaining an average energy efficiency of 0.15%. In this case the low solar-to-fuel efficiency is due to the inhomogeneous temperature distribution in the felt that limit the outside surface temperature. According on this results a CeO_2 reticulated porous ceramic (RPC) foam was developed by Furler et al. [66]. With this sample a higher average energy efficiency of 1.73% was achieved

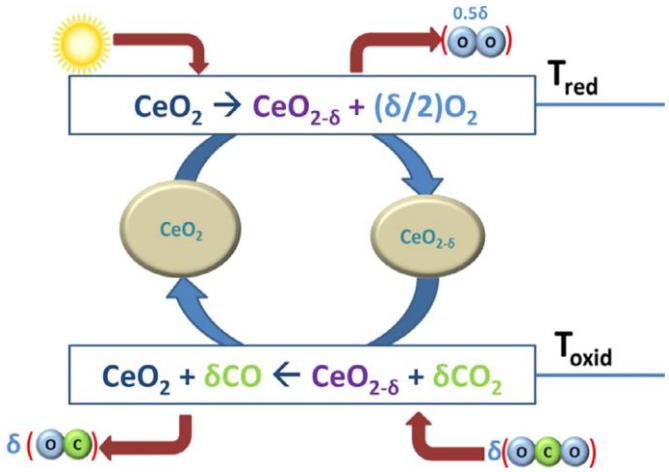

Figure 2.15: *Ceria-based thermochemical cycle [69].*

thanks to the enhanced absorption of solar energy due to macroporous structure of ceria. Anyway, the oxidation reaction was limited by low specific surface area, in fact the same authors [67] develop CeO_2 reticulated foam structure with dual-scale porosities in order to maintain a higher volumetric absorption of the incident solar radiation and a uniform heating that favor the high-temperature reduction step, but at the same time also a higher specific surface area was achieved enhancing reaction kinetics and favoring the oxidation reaction [17]. Moreover, the same solar-to-fuel efficiency value was maintained. Ackermann et al. [68] showed the dependance of CDS oxidation rates on the temperature and oxygen nonstoichiometric after reduction in H_2 (Figure 2.16), showing a decrease in CO production with increasing δ_{red} (indicated as δ_i in Figure 2.16) and with decreasing operating temperature. The doping option has been investigated, as for iron oxides, also for ceria considering transition metal and rare earth metal oxides including Sr^{2+}, Mg^{2+}, Ca^{2+}, La^{3+}, Y^{3+}, Gd^{3+}, Hf^{4+} and Zr^{4+}. Subsequently to the introduction of dopants, the structure exhibited oxygen defects in the lattice eventually due to the different sizes and atomic radius between Ce^{4+} and the dopant. $Ce_{0.9}Zr_{0.1}O_2$ and $Ce_{0.9}Hf_{0.1}O_2$ were investigated for water-splitting thermochemical cycles and it was found that they had a higher oxygen releasing ability compared to other doped ceria materials [70], furthermore the addition of Zr^{4+} (up to 50 mol%) improved the reduction extent but, on the other hand, it affected negatively the material cycling ability if compared to undoped ceria [71].

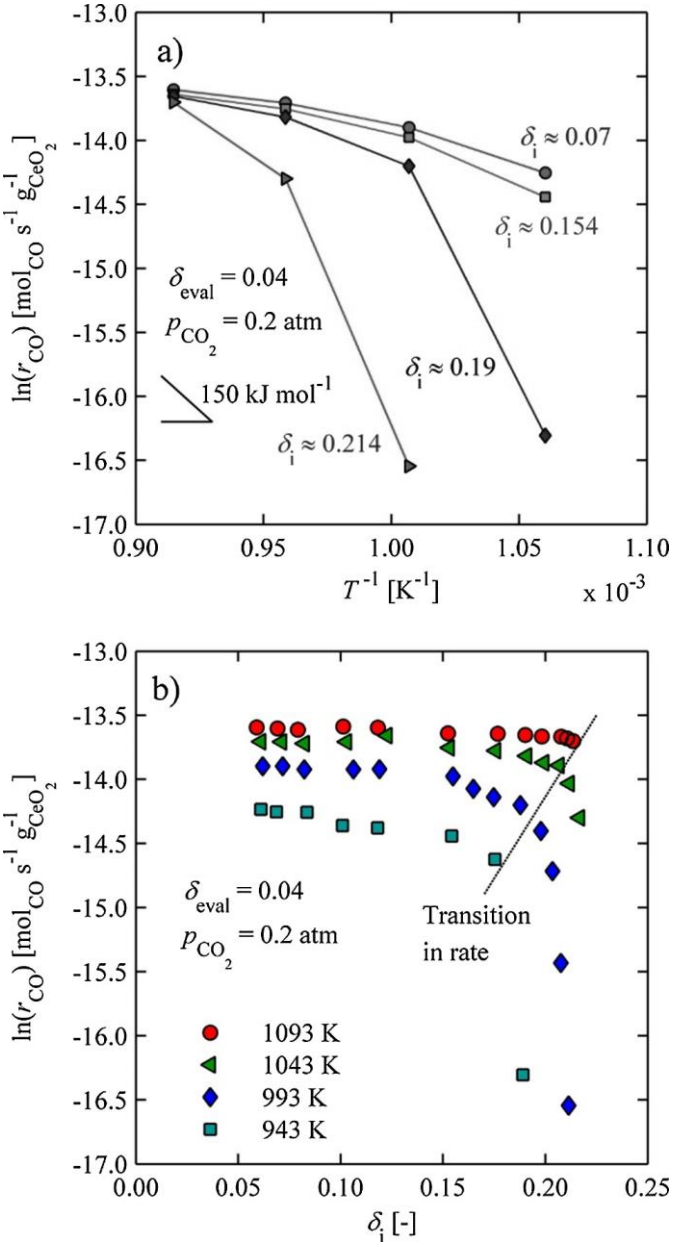

Figure 2.16: *(a) CO production vs temperature, (b) CO production vs initial reduction extents [68].*

Resuming, the improved reduction extents due to Zr^{4+} doping was obtained at the expenses of a slower oxidation kinetic and a reduced thermodynamic favorability. Kawakami et al. [72] compared $NiFe_2O_4/m-ZrO_2/MPSZ$ and $CeO_2/MPSZ$, it was noticed that ceria based foam perform better achieving a higher production of hydrogen and oxygen during the two-step water-splitting cycle, while the Ni-ferrite foam had the negative occurrence of sintering phenomena during the high

temperature reduction step. La^{3+} and Gd^{3+} doped ceria exhibited a worsening of the redox performance and increasing their concentration the H_2 production yield decreased [73]. Anyway, if La^{3+} and Gd^{3+} are distinctly added in a Zr-doped ceria sample, they was able to further enhance thermal resistance and stability. Jiang et al. [74] studied the CO_2 splitting using $Ce_xM_{1-x}O_{2-\delta}$ ($M = Ti^{4+}$, Sn^{4+}, Hf^{4+}, Zr^{4+}, La^{3+}, Y^{3+}, and Sm^{3}) as oxygen carriers. During the reduction step at 1400°C the amount of oxygen released resulted in the following order: $Ce_{0.85}Y_{0.15}O_{2-\delta}$ and $Ce_{0.85}Sm_{0.15}O_{2-\delta}$ (1.4 ml/g) < $Ce_{0.85}La_{0.15}O_{2-\delta}$ (1.5 ml/g) < $Ce_{0.9}La_{0.1}O_{2-\delta}$ (2.0 ml/g) < CeO_2 (2.5 ml/g) < $Ce_{0.75}Zr_{0.25}O_2$ (6.5 ml/g) < $Ce_{0.75}Hf_{0.25}O_2$ (7.2 ml/g) < $Ce_{0.8}Sn_{0.2}O_2$ (11.2 ml/g) < $Ce_{0.8}Ti_{0.2}O_2$ (13.2 ml/g). From the obtained data it is found that tetravalent cations lead to an improvement with respect to undoped ceria, while trivalent cations show the opposite behavior. The oxidation step was performed in the temperature range 600°C-1200°C, and it was found that at 800°C the CO production for $Ce_{0.75}Zr_{0.25}O_2$ was 10.0 ml/g, almost three times higher if compared to undoped ceria CO production. Takalkar et al. [75] investigated a two-step CO_2-splitting thermochemical cycle analyzing the effect of doping a ceria oxygen carrier with transition metal cations: $Ce_{0.9}M_{0.1}O_{2-\delta}$ (M=Ni, Zn, Mn, Fe, Cu, Cr, Co, Zr). A TGA (thermogravimetric analysis) was performed and it consisted of an oxidation step carried out with a gas flow composition of 50% CO_2/50% Ar at 1000°C, and of a reduction step carried out in presence of Ar at 1400°C. The data obtained after 10 thermochemical cycles presented CeZn and CeFe as the only two samples able to overcome Ce performance in terms of both oxygen released and CO production. In fact, considering a single cycle as a reference, the amount of oxygen released follow this order: CeFe (92.5 μmol/g) > CeZn (69.5 μmol/g) > Ce (45.8 μmol/g). According to CO production the results show that CeZn (126.4 μmol/g) > CeFe (118.9 μmol/g) > Ce (110.4 μmol/g). On the other hand, CeNi and CeCo were the worst samples showing a negative performance with respect to undoped ceria sample a lower amount of oxygen released and CO produced.

2.4.3 – Perovskite oxygen carriers

In recent years, perovskite oxides raised a growing interest as alternative class of material for several application. Perovskites have been widely used in solid oxide fuel cells [81], in oxygen permeable membranes [80], and specially as oxygen carriers for CO_2/H_2O splitting in thermochemical cycles [76]. It has been considered as alternative to ceria-based oxide [19] and the other metal-oxide carriers because of its promising properties: high-thermal stability, enhanced reduction extent, lower reduction temperature required, well-defined structure, excellent oxygen capacities at lower temperatures. The general formula of perovskites is ABO_3 where A and B identify a rare earth cation and a transition metal cation, respectively. The A cation is responsible for the thermal resistance, while the B cation is determinant for catalytic activity [76]. Depending on the materials that occupy A- and B-sites the stability of the perovskite structure and its reactivity can be efficiently affected. Perovskite's structure is generally cubic with A cations that are 12-fold coordinated with oxygen anions, while B cations are 6-fold coordinated with oxygen anion [77]. The ideal cubic structure crystallize in the space group Pm3m and is reported below in Figure 2.17, it involves corner-shared BO_6 octahedra sites composed by oxygen anions in which a B cation is enclosed. The A cations are placed at the center of the perovskite cubic structure. This type of structure enable to modify perovskite compositions by means of doping obtaining several different structures that may enhance various properties (magnetic, ionic, electronic, etc.) depending on the radius size of the large number of dopants that can be incorporated. In fact, mismatch between the (A-O) and (B-O) bond lengths may occur making possible to accommodate more A and/or B cations. Generally the ionic radius size of A cations is larger than that of B cations, but the diversification of sizes by adding dopants may lead to distortions and modification of the ideal cubic structure. The Goldschmidt tolerance (reaction 2.25) represents a tolerance factor based on the ionic radii of the A, B and O elements in order to determine whether or not the perovskite structure can be formed. When this factor is close to one the perovskite ideal structure can be formed, on the other hand a different structure can be obtained with both a higher or lower tolerance factor, in

fact when $t > 1.02$ a rhombohedral structure is obtained and when $t < 1$ an orthorhombic or tetragonal structure can be formed.

$$t = \frac{r_A + r_O}{\sqrt{2}(r_B + r_O)} \tag{2.25}$$

The distortion induced by a deviation from the *t* unit value does not depends only on the perovskites composition but also on the operating conditions, namely pressure and temperature, to which they are subjected. Some example of defected structured are: double perovskite structures ($A_2B_2O_{5+\delta}$), Ruddlesden-Popper phase ($A_{n+1}B_nO_{3n+1}$) [79], and anti-perovskites where A and B are anions sites.

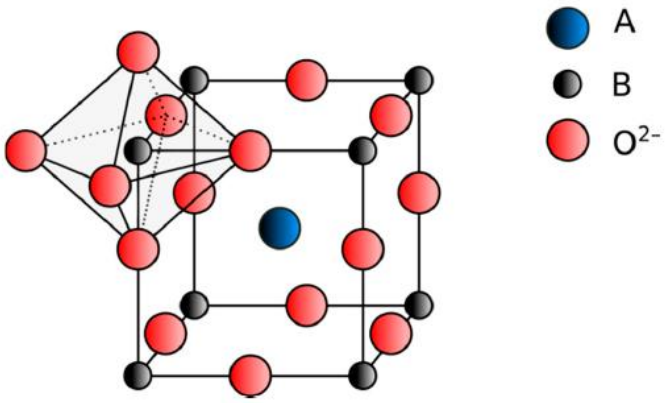

Figure 2.17: *Ideal cubic structure of perovskite with octahedral site [77].*

In the case of thermochemical cycles the perovskite oxygen carriers need a good reactivity for CO_2/H_2O splitting, mobile electronic carriers, a large range of oxygen non-stoichiometry and a well-fitting enthalpy of formation for oxygen vacancies [78]. One of the most attracting property is the large non-stoichiometry of perovskites, especially thanks to their ability of tuning the composition improving thermochemical fuel production. The redox cycle with non-stoichiometric perovskite consists of a first high temperature reduction step (reaction 2.26) and the following oxidation step in which CO_2/H_2O splitting is carried out (reaction 2.27 and 2.28):

$$ABO_{3-\delta_{ox}} \rightarrow ABO_{3-\delta_{red}} + \left(\frac{\delta_{red} - \delta_{ox}}{2}\right) O_2 \tag{2.26}$$

$$ABO_{3-\delta_{red}} + (\delta_{red} - \delta_{ox})H_2O \rightarrow ABO_{3-\delta_{ox}} + (\delta_{red} - \delta_{ox})H_2 \tag{2.27}$$

$$ABO_{3-\delta_{red}} + (\delta_{red} - \delta_{ox})CO_2 \rightarrow ABO_{3-\delta_{ox}} + (\delta_{red} - \delta_{ox})CO \quad (2.28)$$

In terms of applications some studies have been reported from literature. Several authors studied $LaFeO_3$ as it is considered an attractive redox material because of its capability of hosting high concentrations of vacancies in the structure [76]. Zhao et al. [84] investigated $LaFeO_3$ for the production of syngas and hydrogen in chemical looping steam methane reforming (CL-SMR). The oxidation was carried out at 850°C in a fixed bed reactor with two different samples, a macro-porous $LaFeO_3$ and a nano-$LaFeO_3$. It was noticed that over 10 cycles the second sample achieved a higher methane conversion in the first cycle, but it decreased and at the

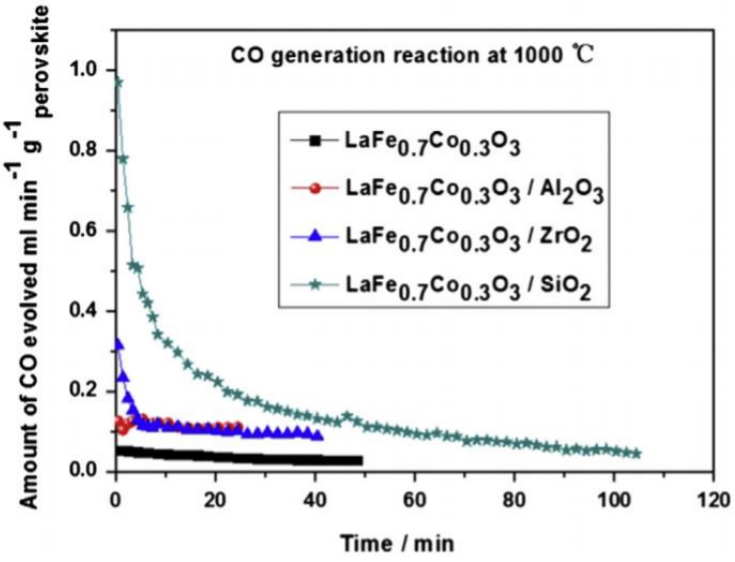

Figure 2.18: *Amount CO evolved in the oxidation step at 1000°C [86].*

last cycle the methane conversion was higher for the first sample. Both the samples exhibits a reduced conversion value over the cycles because of a collapse of the structure caused by thermal and chemical stresses. The same authors [85] studied Co-doped $LaFeO_3$ and it was found out that the doping had positive influence on the redox activity. A higher concentration of oxygen vacancies and reduction resistance were obtained by increasing the amount of Co in $LaFe_{1-x}Co_xO_3$, and a constant methane conversion (around 86%) was achieved with a Co content of x=0.3. Jiang et al. [86] investigated $LaFe_{0.7}Co_{0.3}O_3$ supported by SiO_2, ZrO_2, and Al_2O_3 for CO production through CO_2 splitting. The reduction, carried out at

1300°C, results in an enhanced oxygen evolution. SiO_2 was the support the performed better compared to the others and it leads to an oxygen evolution rate 13 times greater than that produced by unsupported sample. Furthermore, in the oxidation step, carried out at 1000°C, SiO_2-supported $LaFe_{0.7}Co_{0.3}O_3$ exhibits the highest CO generation activity (Figure 2.18). Haeussler et al. [87] investigated experimentally the thermochemical performance of $La_{0.5}Sr_{0.5}Mn_{0.9}Mg_{0.1}O_3$-coated ceria foam in a solar reactor. The reduction and oxidation steps were performed at 1400°C and 1050°C, respectively. A comparison of LSMMg-CeO_2 foam with pure CeO_2 is presented in Figure 2.19a-b. The results show that LSMMg-CeO_2 foam leads to a significantly enhanced fuel production maintaining an energy conversion efficiency (3.7%) similar to that of pure ceria (3.4%).

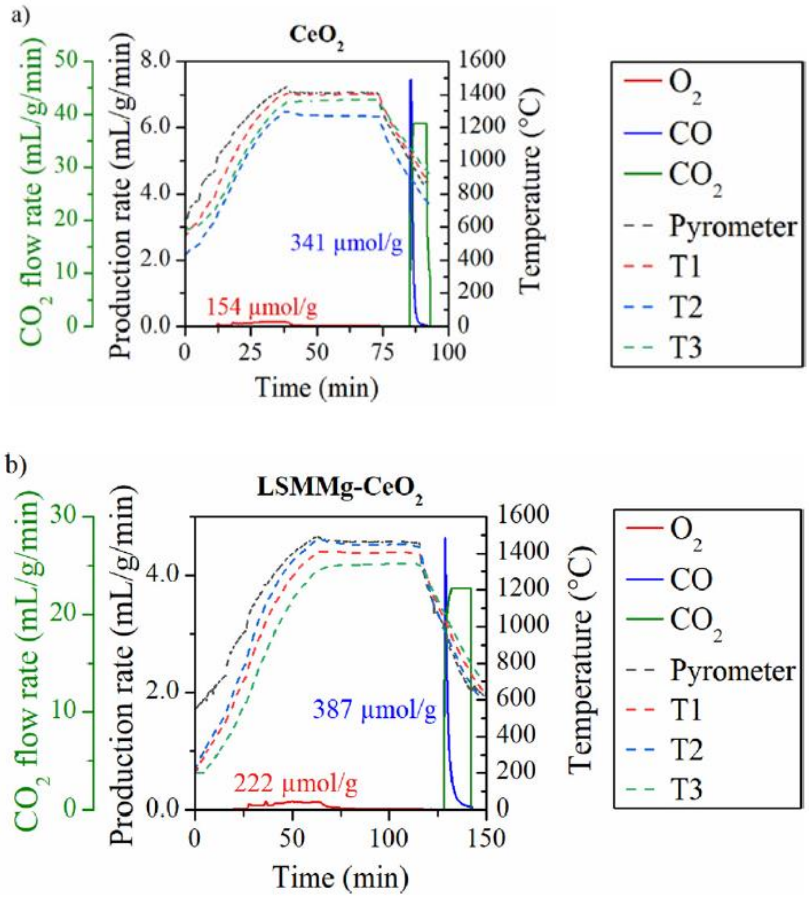

Figure 2.19: *Comparison between LSMMg-CeO_2 and CeO_2 thermochemical performance [87].*

Thermodynamic

Thermodynamic analysis is based on the investigation of the operating temperature and pressure values that enable spontaneously the reaction involved in the thermochemical cycle, thus a negative value of the standard Gibbs free energy ($G°$) has to be achieved. In order to reach these needs there are some criteria to be satisfied:

$$\Delta G°_{TR}\left(P_{O_2,red}, T_{red}\right) < 0 \tag{2.29}$$

$$\Delta G°_{WS}\left(P_{O_2,ox}, T_{ox}\right) < -\Delta G°_{H_2O}\left(P_{O_2,ox}, T_{ox}\right) \tag{2.30}$$

$$\Delta G°_{CDS}\left(P_{O_2,ox}, T_{ox}\right) < -\Delta G°_{CO_2}\left(P_{O_2,ox}, T_{ox}\right) \tag{2.31}$$

The subscripts TR, WS, CDS, "ox", and "red" stand for thermal reduction, water splitting, carbon dioxide splitting, oxidation step, and reduction step, respectively. Below in Figure 2.20 has been reported an example for $La_{0.6}Sr_{0.4}MnO_3$ where the parameters are considered according to standard conditions. From the figure it is noticed that the two temperature T_{high} and T_{low} indicates the values according to which the oxidation and reduction are favourable. In fact, for $T<T_{low}$ and for $T>T_{high}$ the oxidation and reduction are favored, respectively. Anyway considering the non-stoichiometry of the reaction, the Gibbs free energy will depend also on δ, as well as on pressure and temperature.

$$\Delta g°_{\delta}(\delta) = \Delta h°_{\delta}(\delta) - T\Delta s°_{\delta}(\delta) \tag{2.32}$$

In equilibrium condition the value of the oxygen vacancies concentration (δ) is such as to obtain $\Delta g°_{\delta}(\delta) = 0$ [55]. A deviation from standard conditions considering a non-standard pressure affects the entropy variation (reaction 2.33) and consequently the Gibbs free energy variation (reaction 2.34):

$$\Delta S_{TR} = \Delta S°_{TR} - \frac{1}{2}R\ln\left(\frac{P_{O_2}}{P°}\right) \tag{2.33}$$

$$\Delta G_{TR} = \Delta H°_{TR} - T\Delta S°_{TR} + \frac{1}{2}RT\ln\left(\frac{P_{O_2}}{P°}\right) \tag{2.34}$$

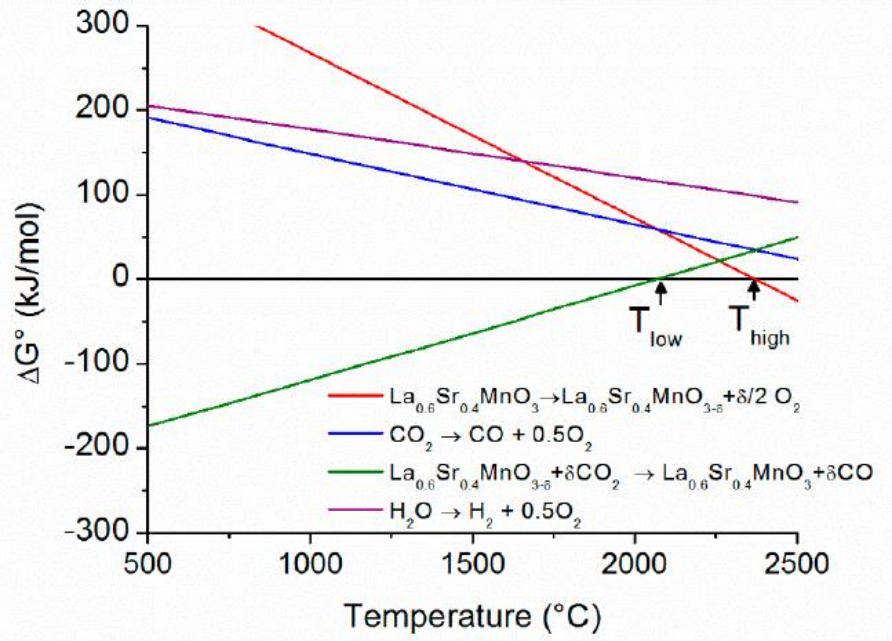

Figure 2.20: *Plot of Gibbs energy for $La_{0.6}Sr_{0.4}MnO_3$ thermochemical cycle, water splitting, and carbon dioxide splitting in standard conditions [77].*

At the same way it is possible to express the Gibbs free energy variation for the oxidation step in case of non-standard pressure (reaction 2.35, 2.36).

$$\Delta G_{WS} = \Delta H°_{WS} - T\Delta S°_{WS} + RT \ln\left(\frac{P_{H_2}}{P_{H_2O}}\right) \tag{2.35}$$

$$\Delta G_{CDS} = \Delta H°_{CDS} - T\Delta S°_{CDS} + RT \ln\left(\frac{P_{CO}}{P_{CO_2}}\right) \tag{2.36}$$

Defect chemistry

Perovskites oxygen carrier belong to non-volatile materials class, thus there are no phase changes during the thermochemical process. Oxygen release and incorporation capacity is one of the most important characteristic of perovskites and represents the driving force for reaction kinetics and fuel production. In order to be able to accommodate large quantities of oxygen in the perovskite lattice, vacancies, or generally structural defects, are required. The point defects are fundamental and there are three different types of them: electronic defects, cationic defects, and

oxygen ionic defects (oxygen vacancy) [78]. Electrons and electron holes are electronic defects that can be introduced in the perovskite structure. Electronic defects allow distribution of oxygen vacancies in the material. Cationic defects generally exists as vacancies in the A-site, they favors B-site vacancies formation. Anyway they have not a central role in the case of fuel production via two-step thermochemical cycle. Oxygen vacancies are p-type defects that allow to maintain the perovskite structure and, at the same time, affect the bulk diffusion and surface exchange of oxygen. Oxygen vacancy is the most important type of point defect, unlike interstitial oxygen that are unfavorable. In fact oxygen vacancies are important for incorporating oxygen during oxidation reactions and then to release it during the reducing step since the oxygen anions diffusion occurs through a vacancy hopping mechanism [82]. Jiang et al. [83] evaluated $Sr_{2-x}MgMoO_{6-\delta}$ (x=0, 0.05, 0.10, 0.15) as anode for a solid-oxide fuel cell and it was noticed that in reducing atmosphere the oxygen released can be calculated in Kroger-Vink notations with the following relation:

$$O_O^x + 2Mo_{Mo}^x \leftrightarrow 2Mo'_{Mo} + V_O'' + \frac{1}{2}O_2 \tag{2.37}$$

O_O^x is the lattice oxygen, V_O'' is the oxygen vacancy, and Mo_{Mo}^x and Mo'_{Mo} represent the ions Mo^{6+} and Mo^{5+}, respectively. As the temperature increases, in reducing atmosphere, the lattice oxygen is released and consequently oxygen vacancies are generated in the structure, furthermore the partial reduction of Mo^{6+} to Mo^{5+} occurs. The reaction 2.37 can be further simplified obtaining:

$$O_O^x + 2h' \leftrightarrow V_O'' + \frac{1}{2}O_2 \tag{2.38}$$

2h' indicates the electron holes obtained from the aforementioned partial reduction. Therefore, according to what is shown in reaction 2.38, at high temperature a portion of the electron holes are converted to oxygen vacancies. The maximum convertible mass in each cycle, thus the maximum fuel production obtainable in each thermochemical cycle, depends on the difference between oxygen vacancies in the perovskite structure during oxidation step and those present during reduction step.

A-site substitution effects

As already stated, doping the perovskite structure is the main way to enhance specific perovskite properties and to optimize fuel production. Globally there are at least 27 suitable elements for the A-site and 35 elements for the B-site (analyzed in the next section). Lanthanum-magnetite perovskites, $LaMnO_3$-based perovskite, are one of the most studied. Sr doping in the A-site has several benefic effects. Sr^{2+} has a lower charge compared to La^{3+} and its substitution leads to Mn oxidation state increases (Mn^{4+}) in order to maintain charge balance. Sr doping allows to obtain a higher reduction extent with respect to $LaMnO_3$ and to pure ceria, too. As the Sr content increases so does the reduction extent (Figure 2.21). It is evident that

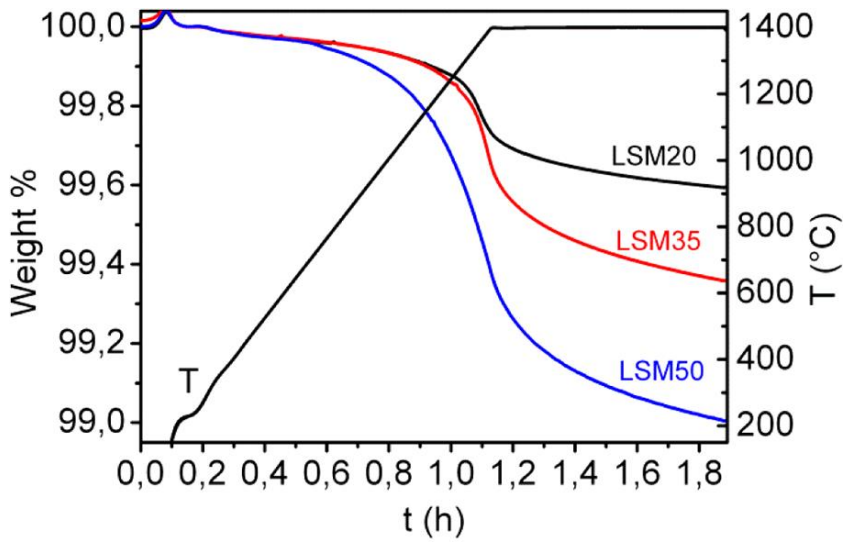

Figure 2.21: *TG analysis during thermal reduction in Ar atmosphere for LSM20, LSM35, and LSM50 [88].*

the higher the Sr content, the greater the change in oxygen content and consequently a higher fuel production is achieved. The thermodynamic characteristics are also affected by the Sr content, in fact as Sr amount increases the enthalpy of reduction decreases monotonically while the entropy remain almost constant (Figure 2.22). The enthalpy decrease implies an enhanced reducibility and a lower reduction temperature requirement, hence a greater ΔT swing between redox steps. Another

effect of the increasing Sr content is the presence of smaller grains in the material and sharp edged crystals, thus a finer structure suggests enhanced kinetics due to higher specific surface area [89]. Furthermore an increasing Sr content leads to a reduced cell volume and a lower lattice constants [91]. Although the amount of oxide required for 1 mol of hydrogen is reduced by Sr-doping, it increases the amount of the needed steam. Another trade-off is highlighted regarding the higher fuel productivity with Sr content that comes at the expenses of a reduction in fuel production kinetics. However, not all amounts of Sr are equally effective, in fact the optimum content of St is reported to be in the range 0.3-0.0 [90].

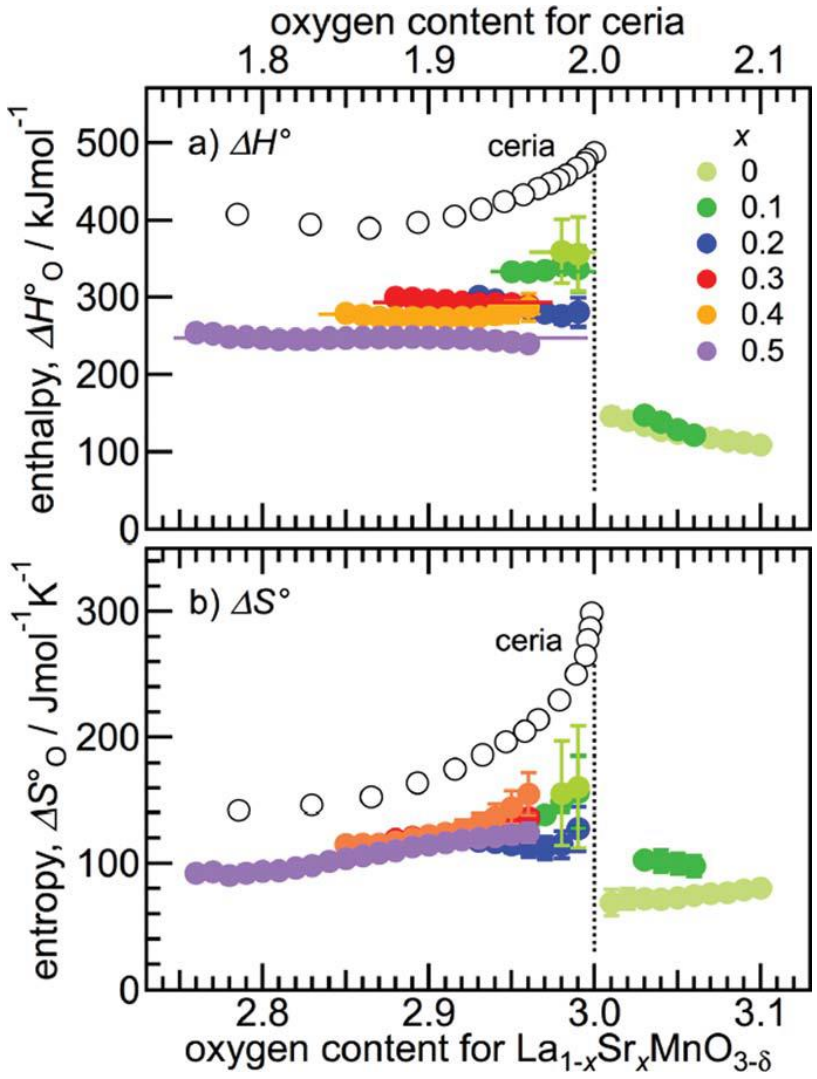

Figure 2.22: *Comparison of thermodynamic characteristics between ceria and LSM for the reduction step: (a) enthalpy and (b) entropy vs. oxygen content [89].*

The cation Ca^{2+} can also be used to substitute La in the A-site. Ca^{2+} has an ionic radius (1.34 A) lower than Sr^{2+} (1.58 A) implying a lower lattice parameter for $La_{1-x}Ca_xMnO_3$. Introducing Ca the reduction extent is further increased because of the larger reduction of the Gibbs' free energy [94], therefore the reduction temperature required is lower than that required for $La_{1-x}Sr_xMnO_3$. Wang et al. [92] investigated thermochemical H_2 production on $La_{1-x}Ca_xMnO_3$ (LCM) with x varying in the range 0.2-0.8, Increasing the Ca content in the perovskite also the oxygen releasing rate increased. The H_2 production increased when x increases only from 0.2 to 0.4, for x > 0.4 a production decline was detected (Figure 2.23).

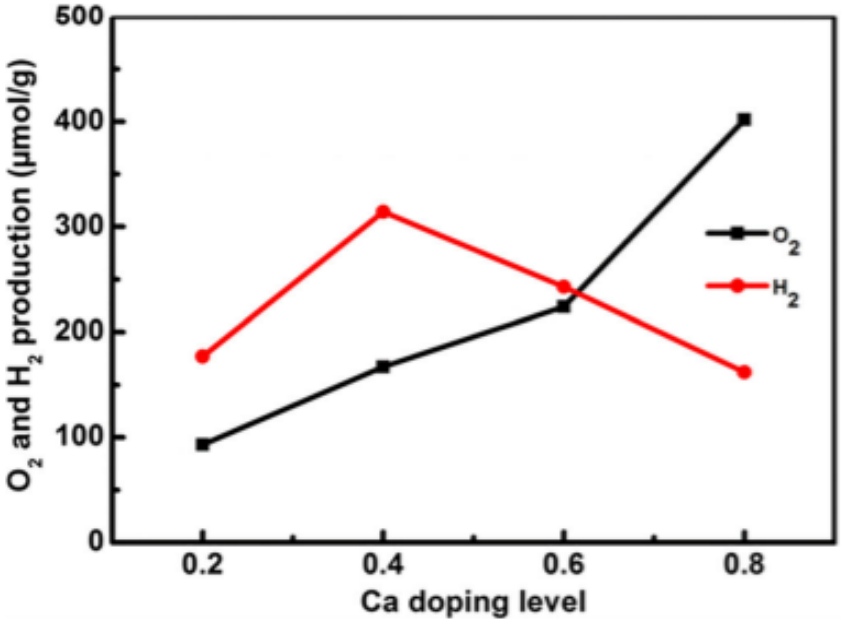

Figure 2.23: *O_2 and H_2 production as function of Ca content [92].*

Dey et al. [93] studied $La_{1-x}Ca_xMnO_3$ with x = 0.35, 0.5, 0.65, a decreasing lattice parameters was noticed when increasing Ca content. Switching from Sr to Ca the oxygen released has been observed to increase remarkably, and the same behavior has been found also for the H_2 production (Figure 2.24). Although Ca resulted in better properties, in the case of CO_2 splitting Sr doping exhibited an enhanced CO production [95]. As already seen in the case of Sr doping, also for Ca doping the

enthalpy decreased when the Ca content increased, furthermore LCMs had higher entropies than LSMs. For this reasons LCMs had higher non-stoichiometries [96].

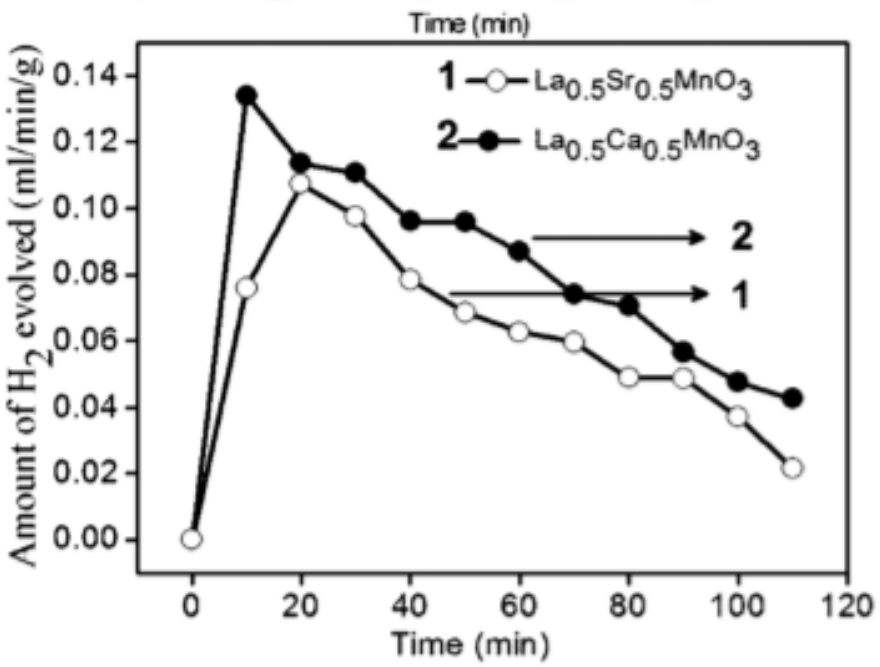

Figure 2.24: *Hydrogen evolution profiles for* $La_{0.5}Ca_{0.5}MnO_3$ *and* $La_{0.5}Sr_{0.5}MnO_3$ *[93].*

Another alternative dopant for the perovskite A-site is Ba^{2+}, this cation had an ionic radius (1.61 A) higher than Sr^{2+} (1.44). Consequently, no reduction extent improvement was detected obtaining also less O_2 production compared to $La_{1-x}Ca_xMnO_3$ and $La_{1-x}Sr_xMnO_3$, The exact order for the oxygen production was the following one: LCM50 > LSM50 > LBM50. The CO production has not been significantly improved by Ba doping. Lanthanum-cobalt is another perovskite family intensively studied for thermochemical cycles. $LaCoO_3$ thermal reduction is favored at low temperatures and a high oxygen production of almost 369 μmol/g at 1300°C, on the opposite the re-oxidation with CO_2 is not favored. In fact the CO production is quite low and it decreases over the cycles [97], and the stability and reactivity during the re-oxidation step are poor because of sintering occurrence. The Ca doping effects on A-site were evaluated , its increasing presence was found to improve oxygen production rate. Wang et al. [98] investigated $La_xCa_{1-x}CoO_3$ perovskite in a two-step thermochemical cycle. The reduction step was performed

at 1300°C for 1 hour finding that the oxygen evolution increased with increasing Ca content from 0.2 to 0.8. The oxidation step has been carried out with a stream of H_2O at different temperature levels (1100-1400°C). The hydrogen production was found to increase only when the Ca doping content increased from 0.2 to 0.4 and then declined at higher contents, as shown below in Figure 2.25.

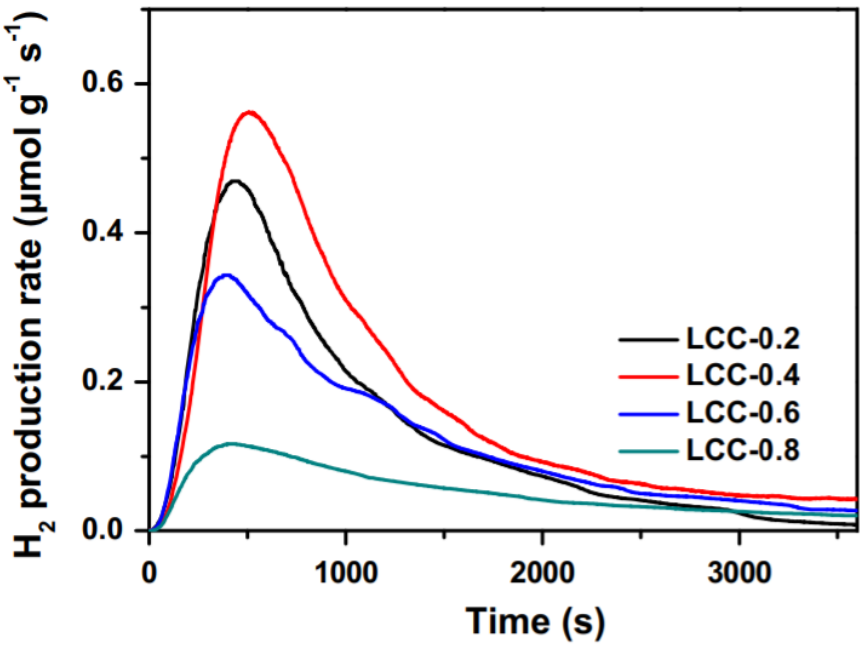

Figure 2.25: *Hydrogen production of LCCs for different Ca content (x) [98].*

Sr was also considered as alternative dopant and Orfila et al. [99] investigated $La_{0.8}Sr_{0.2}CoO_3$ for water splitting thermochemical cycles. It was found that Sr doping implied higher reduction extent than $La_{0.8}Sr_{0.2}MnO_3$, furthermore $La_{0.6}Sr_{0.4}CoO_3$ exhibited a higher hydrogen production compared to $La_{0.6}Sr_{0.4}MnO_3$ for an oxidation step carried out at 1400°C (Figure 2.26). Despite the positive data reported so far, it was also highlighted that after consecutive cycles a Co oxide phase production occur and it affected negatively the H_2/CO production. Moreover, Fe has been studied as dopant element for lanthanum cobalt perovskites and it resulted in non-beneficial effects in terms of oxidation performance. Moreover, the Fe doping had negative impact also on perovskite stability, and re-oxidation yield [97]. The Ca doping in perovskite A-site has been analyzed also for

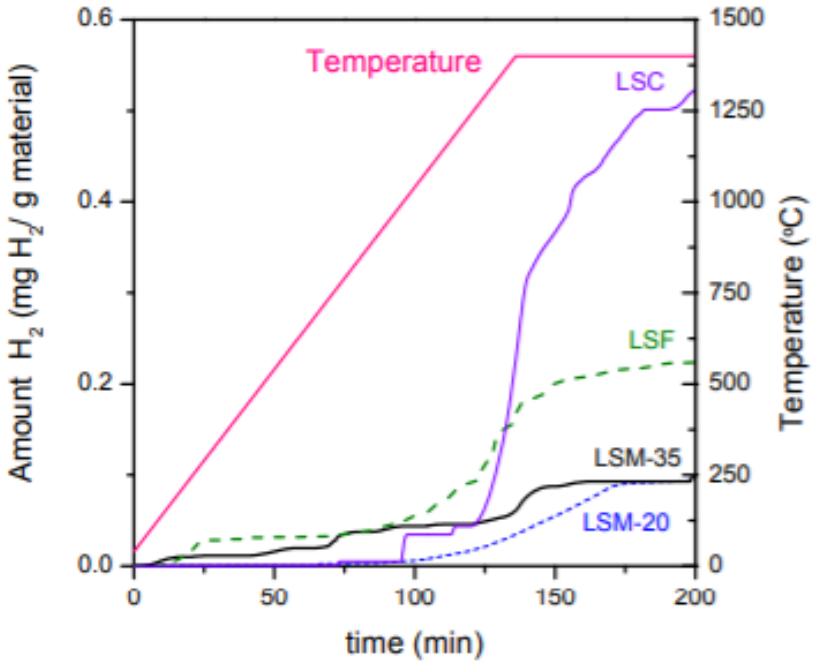

Figure 2.26: *Hydrogen released during oxidation step at 1400°C [99].*

$La_{1-y}Ca_yCu_{0.1}Ni_{0.9}O_3$. As already stated, the Ca^{2+} ionic radius is smaller than that of La^{3+} causing asymmetry in the lattice and generating oxygen vacancies. This structure ensured a lower grains size and a high specific surface area, thus it provided more contact areas with reducing gases [100]. Jiang et al. [101] investigated $La_{1-y}Ca_yCu_{0.1}Ni_{0.9}O_3$ for solar hydrogen production via CL-SMR. BET (Brunauer Emmet-Teller) measurements were carried out and the specific surface area was reported depending on the Ca content. Undoped $LaNiO_3$ exhibited a specific surface area of 4.604 m^2/g, while for $La_{0.5}Ca_{0.5}Cu_{0.1}Ni_{0.9}O_3$ a specific surface area of 4.618 m^2/g was found, furthermore this value further increase up to 5.295 m^2/g for a Ca content of y = 0.9. It was noticed that Ca doping led to a lower reduction temperature. The increasing Ca content was found to result also in higher oxygen release and in a higher methane conversion (Figure 2.27). Other studies considered Sr-doped $LaFeO_3$, for example different levels of doping were investigated by He et al. [102]. In this work $La_{1-x}Sr_xFeO_3$ (x=0.1, 0.3, 0.5, 0.9) perovskites were prepared and consequently employed as oxygen carriers in a CLR process.

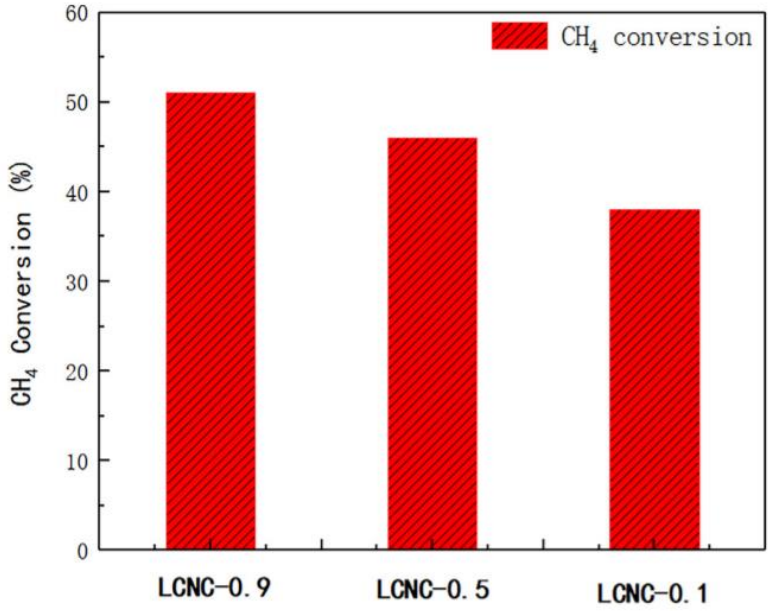

Figure 2.27: *Methane conversion for* $La_{1-y}Ca_yCu_{0.1}Ni_{0.9}O_3$ *[101].*

The La substitution with Sr cations led to lattice contraction due to the Sr smaller ionic radius, furthermore Sr^{2+} insertion caused electric unbalance in the structure that is compensated by oxygen vacancies generation or by oxidation of a portion of Fe^{3+} to Fe^{4+}. The perovskite material is not significantly improved by Sr doping since it exhibited low stability, anyway Sr had positive effects on the oxygen amount adsorbed. Yttrium-manganese perovskites have been extensively investigated in terms of doping influence. Strontium was studied as dopant and it was found that $Y_{0.5}Sr_{0.5}MnO_3$ had a higher reduction extent compared to $La_{0.5}Sr_{0.5}MnO_3$. This effect is mainly due to geometric aspects. In fact, Y^{3+} has a smaller ionic radius (1.08 A) than La^{3+} (1.36 A), this aspect affects the structure distortion increasing the inclination of MnO_6 octahedron favoring the releasing of oxygen from the lattice. Demont and Abanades [94] reported a higher oxygen production rate with respect to the overcited doped lanthanum-manganite perovskites (Figure 2.28). Moreover, the Ca cation has been used as dopant in A-site yielding $Y_{1-x}Ca_xMnO_3$. It was investigated by Dey et al. [103] in thermochemical cycles for CO and H_2 production in comparison with to

$Y_{0.5}Sr_{0.5}MnO_3$ (YSM50). The CO production for YCM50 (671 μmol/g) was higher than that achieved with YSM50 (around 550 μmol/g).

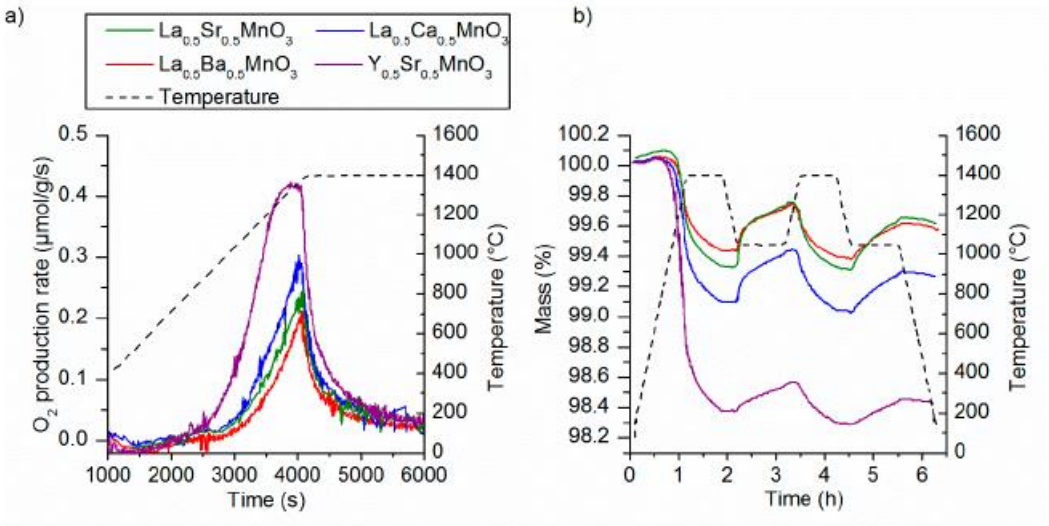

Figure 2.28: *(a) Oxygen production rates, (b) TGA data for the investigated samples during reduction at 1400°C and oxidation at 1050°C [94].*

The same behavior was exhibited in the case of the oxygen production measurements during the reduction step at 1400°C; YSM50 exhibited an oxygen production of 481 μmol/g, while the oxygen production for YCM50 was found to be equal to 593 μmol/g. The same authors, in the same work [103], investigated the influence of A-site doping for $Ln_{0.5}A_{0.5}MnO_3$ (Ln=La, Nd, Sm, Gd, Dy, Y; A=Sr, Ca). An increasing reduction extent was shown for decreasing ionic radius of the rare-earth materials tested. Consequently, also a more distorted structure, with a lower Goldschmidt tolerance, was detected. The thermochemical cycle considered consists of the reduction step and oxidation step carried out at 1400°C and 1100°C, respectively. The various doped perovskites have been reported in Figure 2.29 with respective oxygen and CO production. Among all the materials testes, YCM50 and YSM50 proved once again to exhibit the best performances (Figure 2.29). The $Ba_{1-x}Sr_xFeO_3$ perovskite represents an interesting class of non-stoichiometric oxides. It was investigated in isothermal condition (1000°C) with a content of Ba equal to x=0.5. The Ba doping has negative effects such as decreased

reduction extent and low CO production. Anyway, Ba-based carbonate formation was not observed [97].

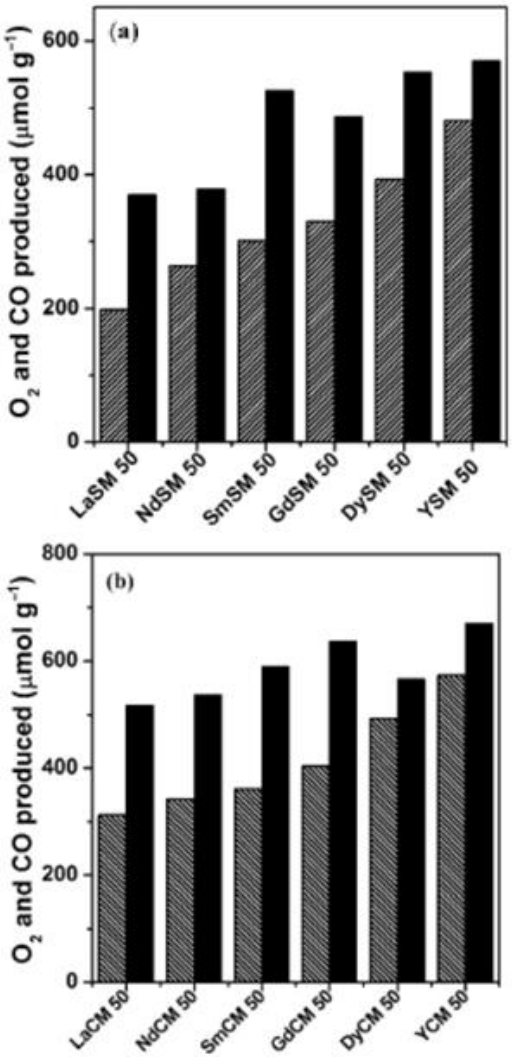

Figure 2.29: *TGA curves for thermochemical CO_2 splitting: (a) and (b) show the total amount of oxygen (dashed bar) and CO (filled bar) production for $Ln_{0.5}Sr_{0.5}MnO_3$ and $Ln_{0.5}Ca_{0.5}MnO_3$, respectively [103].*

B-site substitution effects

Lanthanum-manganese perovskites have been investigated in terms of A-site doping effects in the previous section, and it was found that none of the considered compositions exhibited a full re-oxidation. In order to fill this gap the B-site doping has been carried out. As first option, Al has been taken into account for B-site

substitution in $(La, Sr)MnO_3$ perovskites. When Al^{3+} is introduced, the reduction of Mn^{3+} to Mn^{2+} is prevented, unlike the reduction of Mn^{4+} to Mn^{3+}. The Al^{3+} has an ionic radius (0.535 A) smaller than Mn^{3+} (0.645 A) in the lattice and this implies a stronger atomic interaction related to smaller cell volume, and thus it affects positively the perovskite stability. The presence of Al^{3+} allowed to improve the reduction extent and also, the re-oxidation yield, and the reaction kinetics. Anyway, *Al* did not participate to the redox reactions maintaining its oxidation state throughout the process. Al^{3+} B-site doped LSM (LSMA) led to a higher oxygen release during reduction than LSM and pure ceria. Furthermore, also the fuel yields for CO and H_2 result improved if compared to CeO_2. The reduction extent was promoted by a lower reduction enthalpy [104] that decreased whit increasing δ. Al^{3+} has been investigated as B-site dopant also in LCM. Cooper et al. [96] investigated $La_{0.6}Sr_{0.4}MnO_3$, $La_{0.6}Ca_{0.4}MnO_3$, and $La_{1-x}(Sr, Ca)_xMn_{1-y}Al_yO_3$ in solar thermochemical fuel production. All the proposed materials showed a higher degree of reduction if compared to ceria (Figure 2.30)

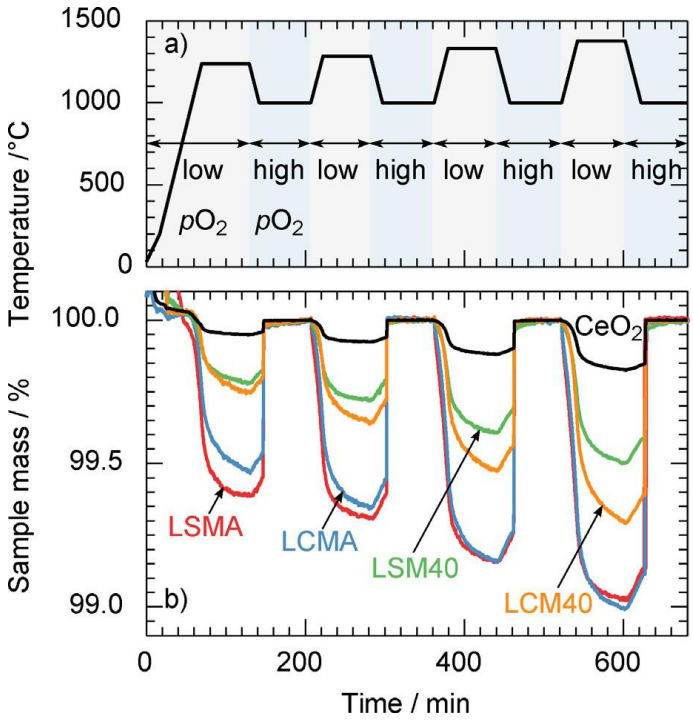

Figure 2.30: *Comparison between LCM40, LSM40, LCMA, and LSMA: (a) temperature profile during the redox cycle (1240-1400°C), (b) mass variation [96].*

This comparison confirmed that the introduction of Al^{3+}significantly affected the reduction extent. The oxidation step was further investigated within a temperature range of 650-1240°C using as oxidizing a gas mixture of CO_2 (50%) and Ar (50%). It was noticed that the lower the oxidation temperature, the more the re-oxidation tended to be complete. Another important effect of the Al^{3+} B-site doping during the oxidation reaction was the hindering of carbonate phases formation, whose presence impacted negatively on fuel production. In fact Figure 2.31 (a, b) show a TGA consisting in a reduction step (1350°C) and an oxidation step under CO_2 at a temperature ramp 400-1200°C. Corresponding to the oxidation reaction, the Al-free perovskites exhibited a significant mass increase that corresponded to carbonates generation. This behavior was not noticed in the Al-doped perovskites (Figure 2.31 c, d). Moreover, LSMA and LCMA resulted also in a higher CO production than LCM40,LSM40 and ceria. Takacs et al. [106] also investigated LSM40, LCM40, LSMA and LCMA in order to determine the doping influence of Al^{3+}. Also in this

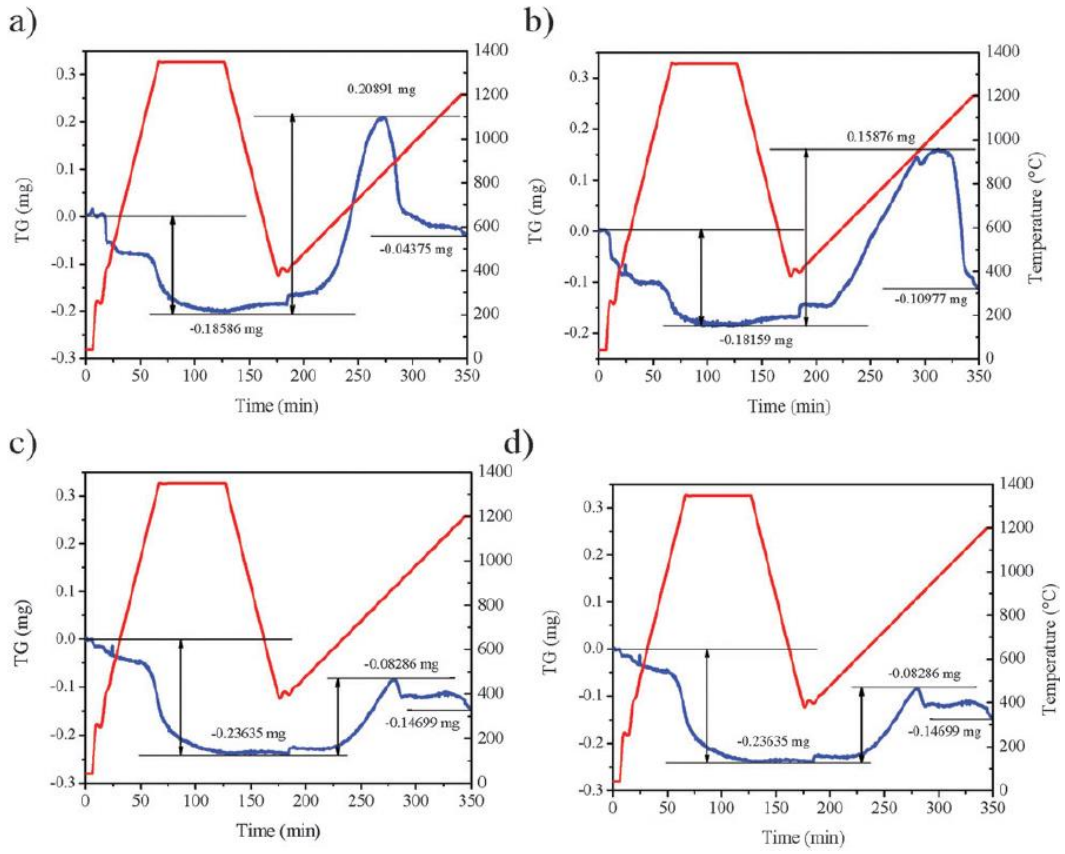

Figure 2.31: *TGA with reduction at 1350°C and oxidation at a temperature ramp 400-1200°C: (a) LCM40, (b) LSM40, (c) LCMA, (d) LSMA [105].*

work the four perovskites exhibited higher reduction extents, compared to ceria, in a process comprising a reduction reaction occurred at 1573-1773 K and an oxidation step carried out at 873 K. Takacs work confirmed also what was found by Cooper [96] in terms of thermodynamic parameters. In fact it was found that the reduction enthalpy of the Al-doped perovskites decreases with increasing δ (Figure 2.32), exhibiting an opposite behavior compared to LSM40 and LCM40.

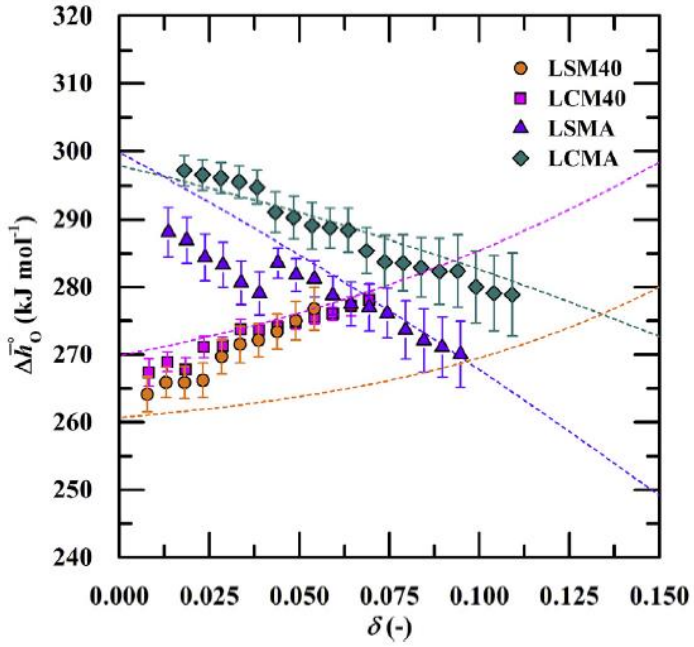

Figure 2.32: *Molar enthalpy curves for LSM40, LCM40, LSMA, and LCMA [106].*

Wang et al. [107] investigated Ga^{3+} doped LCM perovskite in a two-step thermochemical cycle. Ga^{3+} ionic radius (0.62 A), which is smaller than that of Mn^{3+} (0.645 A), leads to a decreasing pore size and to an increased surface area and this has a positive effect on gas transportation ability, and thus on fuel production. The Ga^{3+} doping on the B-site of LCM showed a good thermodynamic performance during the reduction step (1300°C) exhibiting a hydrogen production of 401 μmol/g, that is higher if compared to Al-doped LCM production (339 μmol/g). On the other hand, during the following oxidation step (900°C) Ga-doped LCM showed a re-oxidation yield of 95°C. Furthermore, also in the case of CO_2 splitting it has been noticed an increasing in CO production with respect to undoped LCM. However, the content of Ga^{3+} used to substitute Mn cations was found to be

limited to 30% [108]. Jouannaux et al. [109] studied the effect of B-site doping on lanthanum manganite perovskites (LSM, LCM) using Al, Mg, Ga and Cr as dopants. A thermogravimetric analyses was performed with two cycles composed by a thermal reduction carried out at 1400°C for 45 minutes and an oxidation step performed at 1050°C for 60 min with a gas mixture of CO_2 and Ar (1:1). All the samples, Ca- and Sr-based perovskites, reached a stable CO production, however Ca-based perovskites exhibited a higher reduction extent. During the first reduction step Al-doped LCM produced the highest amount of oxygen 449 μmol/g, while in the second reduction step the Ga-doped LCM produced more oxygen (175 μmol/g). During the first cycle the highest CO production was observed for LCMGa (215 μmol/g) with a re-oxidation yield of 40%, and although it presented the greatest CO production also in the second cycle, the re-oxidation yield was significantly lower compared to LCM (85%), LCMAl (90%), LCMCr (80%), and LCMMg (71%). Also the Sr-based perovskites presented stable CO productions, they generally have lower reduction extents compared to Ca-based perovskites, with the highest value obtained for LSMAl (302 μmol/g). The TGA profiles are reported in Figure 2.33.

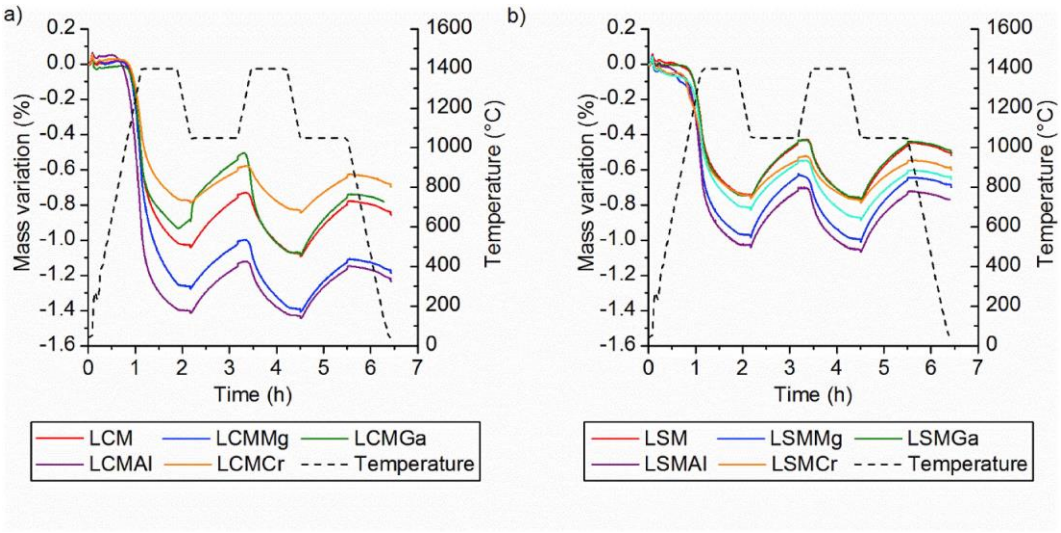

Figure 2.33: *TGA of two redox cycles for carbon dioxide splitting with: (a) Ca-based perovskites, and (b) Sr-based perovskites [109].*

Globally, Sr-based perovskites reached higher re-oxidation yield compared to Ca-based perovskites, this is due to the Ca-based perovskites lower oxidation rates which imply a lower maximal CO production yield. Cr B-site doping resulted in

lower oxygen and CO production for both undoped LCM and LSM, highlighting a negative impact in terms of redox ability. However, LSMCr if employed at high temperature (above 1400°C) resulted in high CO production, and it increased with the Cr content [110]. Ga B-site doping for F LSM has slight effects on the oxygen and CO production, reaching values extremely similar to that obtained for undoped LSM. Finally, Mg doping significantly affects the oxygen and CO production showing attractive redox properties, moreover its presence in the perovskite structure improve the resistance to sintering and the thermal stability. However, its solubility is quite low, therefore the amount of Mg that can be used to substitute Mn is limited to 15-20%. Scandium has been studied as alternative for B-site doping in LSM perovskites. Its introduction, even if a small amount (5%), given its low solubility, permits to double the oxygen produced with respect to that obtained from undoped LSM. However Sc doping and its application in thermochemical cycles with perovskite redox materials has not been extensively investigated. Luciani et al. [111] analyzed the Fe-doping effects on LSM B-site. The structure of $La_{0.6}Sr_{0.4}Mn_{1-x}Fe_xO_3$ (with x=0.2, 0.4, 0.6, 1.0) was studied, it was found that undoped LSM exhibited a single phase with tetragonal structure, for x=0.2 a coexistence of both tetragonal and orthorhombic structures was detected, while only rhombohedral phase structure was revealed for x>0.2. Fe^{3+} cation has a larger ionic radius (0.645) than Mn^{4+} (0.640) and its presence implied a larger unit cell volume. Afterwards a TG analysis was performed with a reduction step carried out at 1350°C in nitrogen (20 min) and an oxidation reaction realized at 1000°C in CO_2 (50 min). In the reduction step a higher oxygen releasing was detected for LSF (x=1.0) compared to LSM, whereas the oxidation step resulted in lower CO production and re-oxidation yield for all the doped samples. This behavior was due to the higher activity of Mn-based perovskites during the oxidation reaction. In fact increasing the Mn content led to higher reactivity and lower temperature requirement. Fe doping was further studied for $LaCoO_3$ but Nair and Abanades [97] pointed out its inefficiency in terms of stability and re-oxidation yield. Babiniec et al. [112] investigated $La_xSr_{1-x}Co_{1-y}M_yO_{3-\delta}$ (M=Mn, Fe) performing a thermogravimetric analysis. $La_{0.3}Sr_{0.7}Co_{0.8}Mn_{0.2}O_3$, $La_{0.3}Sr_{0.7}Co_{0.9}Mn_{0.1}O_3$, and $La_{0.2}Sr_{0.8}Co_{0.8}Fe_{0.2}O_3$ were found to be the most performant among the LSCM

samples with a reaction enthalpy equal to 250 kJ/kg_{ABO_3}, 245 kJ/kg_{ABO_3}, and 210 kJ/kg_{ABO_3}, respectively. The mix Fe/Co in the LSCF B-site tended to increase the reduction extent with respect to LSF perovskites [77] even if the CO production was not improved because of sintering phenomena. The Co doping in $La_{0.6}Sr_{0.4}Cr_{1-x}Co_xO_{3-\delta}$ B-site was analyzed. According to thermodynamic data it was pointed out that higher Co content was beneficial for oxygen release in the reduction step and higher Cr content affected positively the CO_2 splitting. Bork et al. [113] investigated $La_{0.6}Sr_{0.4}Cr_{1-x}Co_xO_{3-\delta}$ (x=0.05, 0.1, 0.2, 0.5) for thermochemical fuel production. It was noticed that with increasing Co content accordingly increased also the oxygen released amount during the reduction step, but the re-oxidation degree tended to decrease. The optimum amount of Co was found to be x=0.2 leading to $La_{0.6}Sr_{0.4}Cr_{0.8}Co_{0.2}O_{3-\delta}$. This sample was used to perform CO_2 and/or H_2O splitting tests (Figure 2.34) resulting in a CO yield (157 μmol/g) 25 times greater of that reached by ceria operating at the same temperatures (800-1200°C).

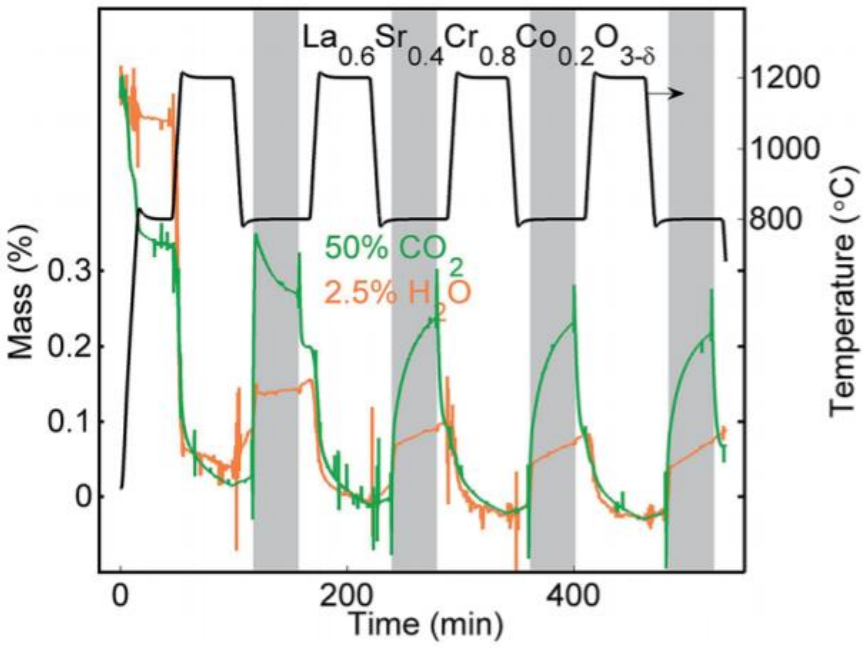

Figure 2.34: *Thermogravimetric analysis of $La_{0.6}Sr_{0.4}Cr_{0.8}Co_{0.2}O_{3-\delta}$. Reduction at 1200°C in Ar, oxidation at 800°C with 50% CO_2 or 2.5% H_2O in argon [113].*

Resuming, several available oxygen carrier have been listed and described in terms of their application as redox material in a two-step CO_2/H_2O splitting thermochemical cycle. According to their redox characteristics, it is possible to notice how the research currently is focused on finding alternative materials able to reach higher performances. However, thermochemical processes and the oxygen carriers reviewed so far present some challenges. The main problem related to this type of process is the high temperature requirement, that is the reason why new materials development is crucial. A lower operating temperature would have numerous benefic effects, and many other issues would have been solved. A lower temperature is positive in terms of reactor materials life, structural stability of the oxygen carrier, sintering and agglomeration phenomena, and integration with solar thermal energy. Anyway, the operating temperature aspects it is not the only one on interest for the development of new redox materials. In fact, it has been observed that a lot of other physico-chemical properties are fundamental in order to optimize the solar fuel production. For example, beside the temperature, also the ability of generating oxygen vacancies and the ease in releasing and uptaking oxygen from and in the material lattice, respectively, are fundamental to be improved. In the last part of the review, in the case of perovskite-based oxygen carriers, the doping has been the main path through which trying to reach those objectives. Through the doping it was possible to tune the perovskite properties in order to make it able to produce more oxygen, to reach a higher reduction extent, etc. Obviously, as in any other case, the economic and environment points of view have to be always considered, trying to exploit low-cost materials at the best of their abilities and possibly preventing any environmental problems. The oxygen carriers review started from volatile materials (Zn, etc.) showing their applications and the limitations correlated to them. As more attractive alternative the volatile oxygen carriers have been presented. The ferrite-based oxide material has been historically the first one to be studied and investigated for chemical looping processes, but its reduction requires high temperature so ceria was considered as viable option to reduce this requirement. To date, ceria is the state-of-the-art oxygen carrier thanks to its kinetic properties and its redox performances. However, the operating temperature during the reduction step is still too high, so perovskite-based oxygen

carrier have been considered and widely investigated. By the way, in this thesis it is proposed a non-stoichiometric perovskite-based redox material with the following composition: $Sr_2FeNi_{0.4}Mo_{0.6}O_{6-\delta}$ (*Ni*-doped SFM).

Chapter 3

3 – Experimental setup

3.1 – Microreactor setup description

Most of the aforementioned studies made use of an experimental setup based on Thermogravimetric analysis (TGA). However, beside TGA and complementary to that, one of the major alternative methods for the redox material characterization is testing the material through a microreactor setup that enables to study the behavior of the material during the reduction and oxidation reactions. This technology implies several advantages related to the operation and control of the operating condition inside the reactor providing process intensification, and a gain in yield and safety. Miniaturization of chemical processes leads to a lower requirement of reactants amount for the reactions and allows to make the experimentation process faster. Gerven et al. [114] used microreactors in order to perform photochemical and photocatalytic processes. Using a microreactors was noticed an efficient exposure to solar radiation thanks to the high surface to volume ratio. Kraai et al. [115] investigated the biodiesel production with a microreactor obtaining better results, compared to those obtained by batch processes, thanks to the possibility of performing the process in continuous mode. Therefore, resuming, the advantages related to microreactor technology employment are: enhanced heat and mass transfer, flexibility, higher products quality, efficient mixing, precisely controlled variables (temperature, flow rates), high surface-to-volume ratio, good heat removal, and ability to monitor the progress of extraction and reaction [116]. The microreactor tests enable to observe a process involving the perovskite SFNM04

sample that is closer to large-scale system currently in commerce than TGA. In fact, a sample of around 10-15 mg is used in the case of TGA processes, whereas in a microreactor process a SFNM sample of 200 mg has been used in the current work. Accordingly, also the gas flows report a higher order of magnitude compared to TGA. In particular a thermogravimetric analysis evaluates the mass variation of the sample thanks to a balance mechanism. However, the weight variation may be due to the actual redox reactions performed, but also to the formation of unwanted species such as carbonates, or to carbon deposition, etc. On the other hand, microreactor tests enable to directly observe the *CO* or H_2 production during the process. Nevertheless, the two methods, TGA and microreactor tests, are complementary and the data obtained from both are necessary to outline adequately the sample behavior and its properties The experimental bench employed in this work (Figure 3.1) installed in the Environment Park laboratory is aimed at testing powders and pellets under controlled atmosphere at ambient pressure in a microreactor heated up to 1700°C.

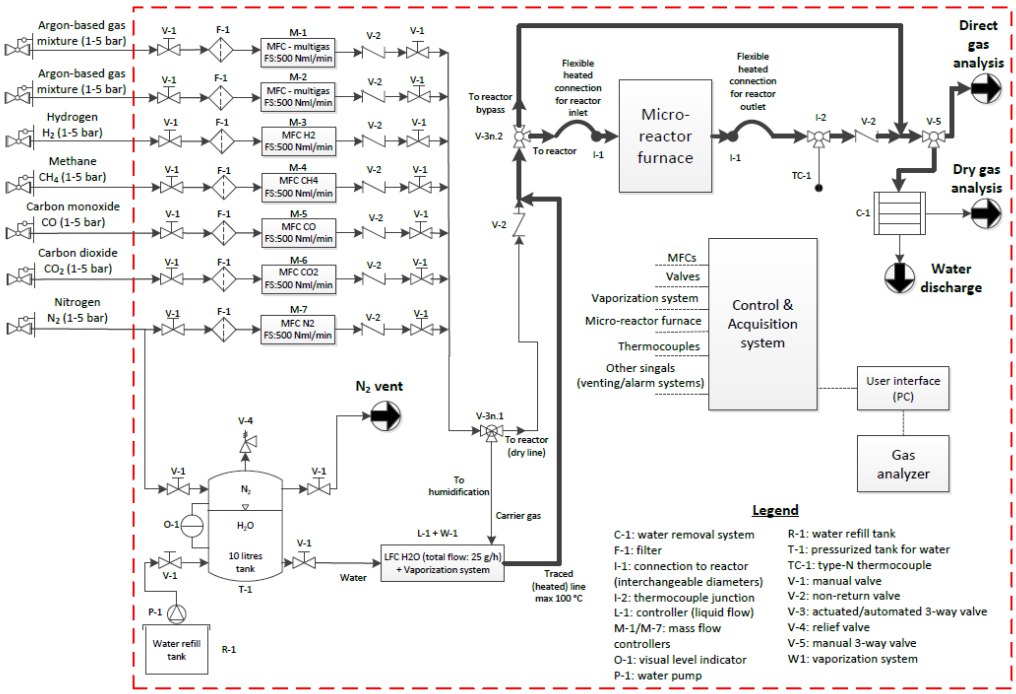

Figure 3.1: *Schematic of the test bench.*

The bench is equipped with a feeding system consisting of 7 gas lines and a water vapor generation system. The gas supplied through the laboratory lines (5 out of the mentioned above) are: N_2, CH_4, CO, CO_2, H_2. These gases are connected to the laboratory lines by means of pressure reducers installed on the wall. The remaining two gas lines are connected to cylinders which have pressure reducers directly installed on them, but only from the moment they are used and therefore connected to the bench. Downstream of the reducers there are the mass-flow controllers (MFC) to which the gases arrive through steel connection pipes (in the case of laboratory gases) or in Teflon (in the case of the cylinders). Generally the gases contained in the two eventually connected cylinders may be: Ar-H_2 (5% max), Ar-CH_4 (5% max), Ar-CO_2 (5% max), Ar-O_2 (5% max), and air. All lines have an imposed pressure of 2.5 bar, except for the nitrogen which is at 3.5-5 bar since its line is also used to pressurize the demineralized water tank. The MFCs regulate and measure the flow rate of the gases, which subsequently converges into the dry mix line. The dry gases mix line is connected to a three-way valve (V-3n.1) from which it is possible to directly feed the microreactor with the dry mixture or to humidify it first. The latter case implies the mixing of the dry flow with the vaporized water obtaining a wet mixture which is heated, and then rejoins with the dry line. However, in the present work all the performed processes involves the use of only the dry mixture. After the rejoining of the two lines there is a second three-way valve (V-3n.2) which allows to select between direct feeding of the micro-reactor or, alternatively, the bypass of the reactor. In the present work the bypass line has been used only during the calibration phase of the gas analyzer, whereas during all the experimental tests the gas mixture has been sent in the microreactor. The tubular microreactor employed in the present experimental bench is the working tube of the electric furnace (Carbolite Gero, Germany) that heats the ceramic tube of the reactor reaching temperatures up to 1700°C. The connection between the reactor and the gas lines is ensured by flanges sealed by O-rings. At the exit from the reactor there is the reconnection with the bypass line and through a manual valve (V-5) it is possible to choose to direct the gas flow towards the condenser or towards the outlet line which in our case is connected to the gas analyzer . The multichannel gas analyzer is able to determine the concentration of the various gases (CO_2, H_2, CH_4,

O_2, and CO) contained in the final mixture coming from the microreactor outlet. Finally, at the outlet of the gas analyzer the gas flow is conveyed to vent.

3.1.1 – Furnace section

The furnace is the main section of the bench in which the previously composed gas mixture reacts with the redox material sample realizing the reduction and oxidation reactions that constitute the chemical looping process. As already mentioned, the microreactor employed in the present work is the Carbolite Gero working tube (Figure 3.2) that is connected to the electric furnace system. An additional component is the power supply unit of the microreactor furnace that enables the supply of electricity to the resistances allowing the reactor to be properly heated.

Figure 3.2: *Carbolite Gero tubular microreactor.*

Through the power supply and control unit (Figure 3.3 a) it is possible to manage and then control the temperature program. The furnace is controlled by an

Eurotherm PID (Schneider Electric, France). In fact, it is possible to remotely create step by step a personalized temperature program by means of the Eurotherm iTools [117]. Each step of which the temperature program is composed represents a portion of the sequence that can be mainly an isothermal step at a fixed temperature, a ramp-up, or a ramp-down. In the case of ramps it is necessary to specify the set-point temperature values and the rate of progression expressed in K/min, while in the isothermal steps, in addition to the set-point temperature value, the time duration must be set. The microreactor is a continuous flow reactor, unlike batch production, and it consists of a cylindrical horizontal tube made of alumina (Al_2O_3) with a length of 1 m and an internal diameter that measures 32 mm. Furthermore the microreactor presents several insulation layers placed between the inner cylindrical tube and outermost layer in order to provide a temperature barrier and at the same time avoiding heat dispersion that would negatively affect the process. At the center of the reactor the redox material is held in place by an alumina crucible (Figure 3.3 b).

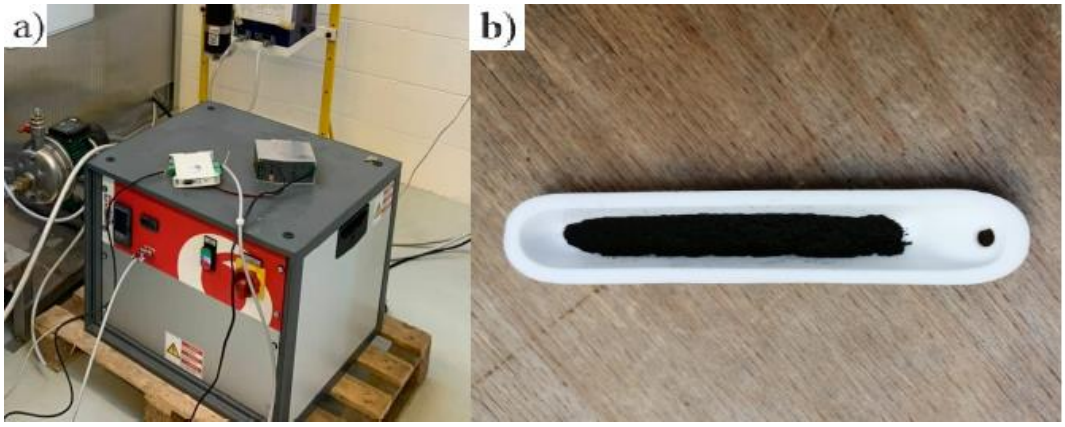

Figure 3.3: *(a) Power conditioning unit (PCU), (b) alumina crucible containing perovskite SFNM sample powder.*

Using this type of holding system the charge and discharge processes of the microreactor are easily manageable. As already mentioned, 200 mg samples have been used in the present work, and the exact mass was measured by using an analytical balance (Figure 3.4) having a high level of accuracy and a resolution of 0.1 mg. Because of its high sensitivity it is equipped with a transparent container

which, once closed, allows the sample mass measurement without the influence of any air currents that could distort the measured value. Once the sample is ready and it has been inserted in the tubular reactor, and once the temperature program has been set, it the sequence of the gas flow with the respective compositions that are fixed in correspondence with the oxidation and reduction reactions is set. As the control of gases and furnace are made by different software, these gases sequences must be temporally synchronized with the temperature program in such a way that when the reactor is set at the choose reduction temperature by the power supply unit the reducing gas mixture is actually sent in the reactor. The same it is true for the oxidation reactions and for all the steps of the thermochemical cycle, such as ramps, purge phases, etc. The gas flow compositions and the various sequence required can be created and remotely organized through a dedicated software run on a local PC connected to the data acquisition and control system of the test bench.

Figure 3.4: *Analytical balance.*

Its interface is reported below in Figure 3.5, in which a scheme of the bench is sketched. All the seven gas lines are represented, and from this interface it is possible to assign manually the value of the flow and its composition, or alternatively it is possible to create the desired sequence of step that will be automatically executed. Through this instrument it is possible to supervise and

control the entire process in fact it can be actually considered a SCADA (Supervisory Control And Data Acquisition) [119].

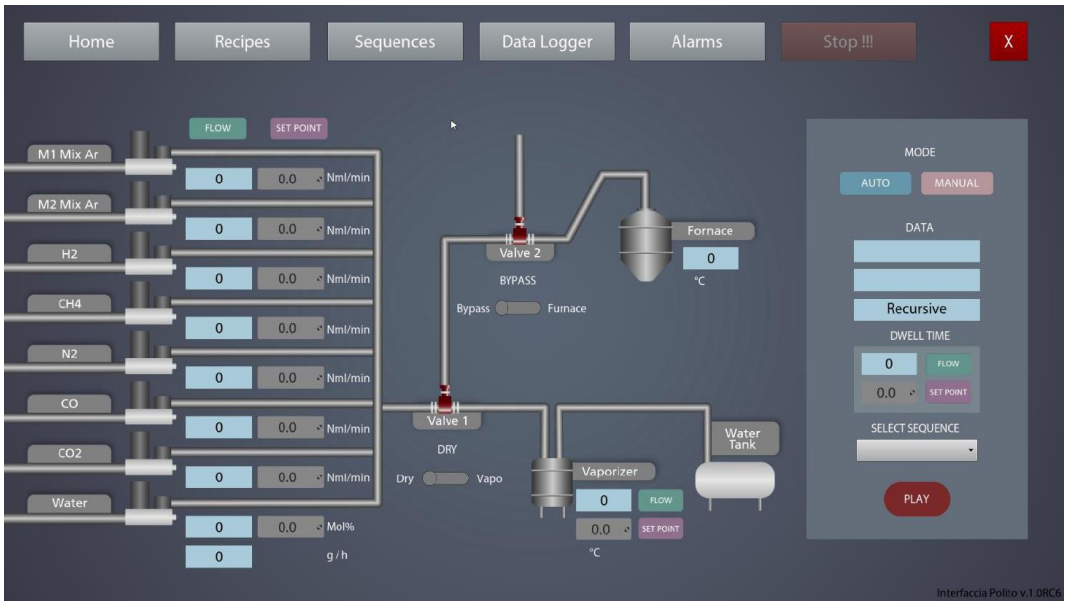

Figure 3.5: *Interface of the control system API-MIoT [119].*

3.1.2 – Gas analyzer section

In this experimental setup the Emerson Rosemount X-Stream XE gas analyzer has been employed, it works with only conditioned gas mixtures, this means that the gas mixture has to be dry, dust-free, and free of any components which may damage the instrument. For this reason upstream the gas analyzer there is a condenser that removes the moisture from the gas flow exiting the microreactor obtaining a dry mixture analyzable by the detection instrument without problems. This continuous gas analyzer is able to measure the gas mixture composition using two different types of detection technology: a thermal conductivity detector (TCD) and an infrared (IR) detector. The technology diversification enable to expand the correct functioning of the instrument to many cases employing various mixtures and compositions. The multichannel gas analyzer allows to separate the measurement of five distinct chemical species: CO_2, H_2, CH_4, O_2, and CO, one for each channel. In general, it can be resumed that the gas sensing technologies may be subdivided

into two macro-areas: those based on electrical variation, and those based on other types of variations (Figure 3.6).

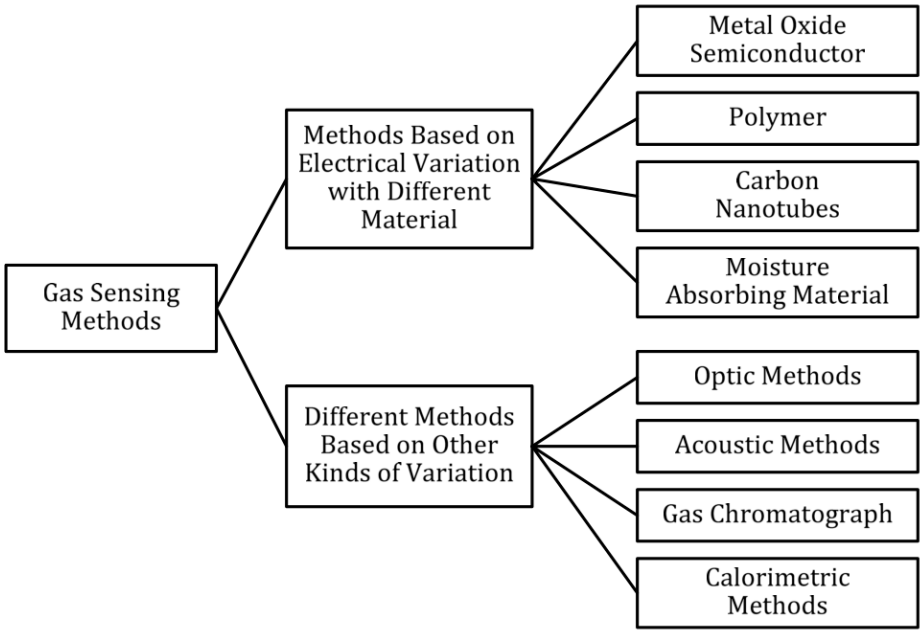

Figure 3.6: *Schematic classification of gas sensing technologies [120].*

All these methods have been investigated and evaluated by Liu et al. [120] using as performance indicators: sensitivity, selectivity, reversibility, response time, adsorptive capacity, energy consumption, and fabrication cost. Among all reported gas sensing methods the most common technologies are metal oxide semiconductors that exhibit high sensitivity, low cost, easy production, and compact size [121]. In the Emerson X-Stream gas analyzer, as already said, has several technologies available that are exploited depending on the composition of the gas mixture, this diversification allows to optimize the gas detection. The Infrared (IR) measurement is one of the measuring principles supported by the gas analyzer. This technology exploit the light absorption of the gas flow in order to distinguish the components of the mixture. In fact irradiating a gas flow with infrared light there will be several wavelengths that pass through, whereas others will be absorbed. If various wavelengths are absorbed it means that they are equal to the vibrational frequencies of the gas flow component. This result is achieved because the atoms of each molecule are capable of vibrating only with characteristic

frequencies [122], and since no compound has the same structure of another one each material has its own absorption bands. In order to evaluate the presence of a single component in a gas mixture it is required to determine the absorption intensity of its bands. In the present case a non-dispersive measurement is achieved using a gas selective detector. Twiss et al. [122] describe this process that consists of two infrared sources, a compensating cell containing air in parallel with another cell containing the sample, and two sensitized cells (Figure 3.7). The infrared radiation goes through the two cells, in the air cell there is no hydrocarbon so the radiation is absorbed by the underlying sensitized cell that instead contains hydrocarbons. On the other hand, in the sample cell a radiation portion is absorbed, while the remainder portion is absorbed always by the sensitized cell. At the end the sensitized cells on the left will exhibit a higher temperature that enables the deflection of the diaphragm placed between the two sensitized cells. In this way, it is possible to determine the hydrocarbon content in the sample cell. The instrument needs to be calibrated with a mixture that has to be similar to the expected one. However, the nitrogen shows no infrared radiation absorption, for this reason, generally. it is sent a N_2 gas flow to the gas analyzer in order to calibrate the zero value for all the five channels.

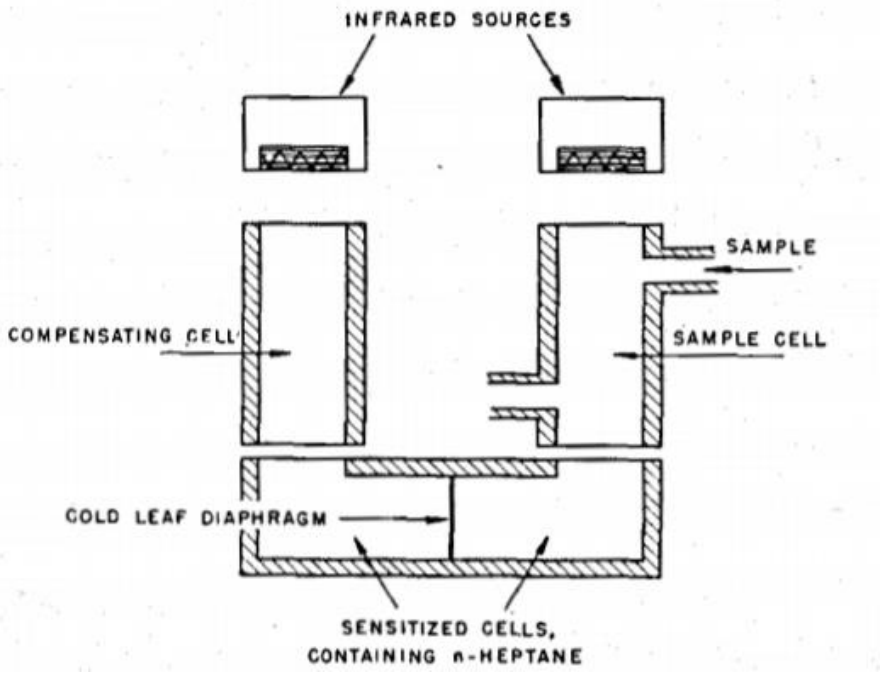

Figure 3.7: *Non-dispersive infrared analyzer example [122].*

The thermal conductivity measurement is based obviously on the ability of the analyzed material to conduct heat. This properties is obtained by means of a Wheatstone bridge (Figure 3.8) consisting of 4 temperature sensitive resistors [123]. One of the sensors (R_S) is placed in the sample gas stream, whereas a second sensor (R_R) is placed in a reference gas stream. There are two distinct paths for sample and reference gases, respectively. When no gas is flowing the bridge signal (U_{Br}) is equal to zero. The resistors are heated up by supplying electricity, this heat is then absorbed by the gases flowing through the bridge. Consequently an electric signal is generated and it is proportional to the heat absorbed by the gas flows, thus to their thermal conductivity. According to described operation of this system, a different amount of heat will be adsorbed from sample and reference gas flows, respectively. The two sensors temperatures will be different and this is the cause that generates the electrical signal accordingly to the difference between thermal conductivities of reference and sample streams. In this way, knowing the entity of the signal it is possible to trace uniquely the concentration of a chemical species in the gas sample.

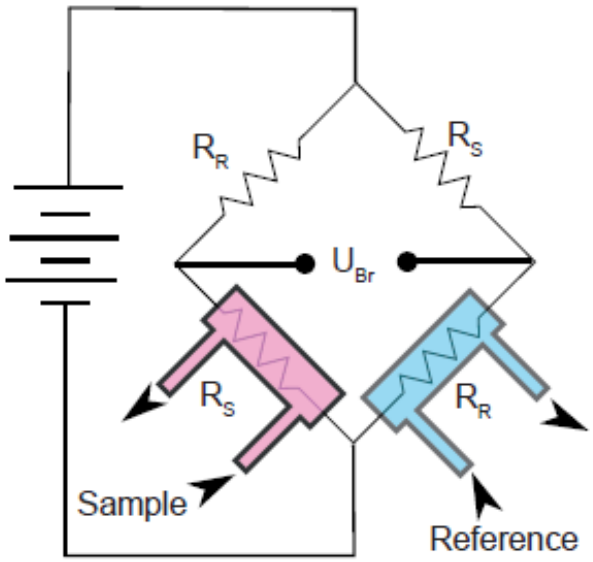

Figure 3.8: *Wheatstone bridge scheme [123].*

Obviously, the results strongly depends on the type of reference gas employed. Generally, helium (He) is chosen since it exhibits a thermal conductivity of 1580

mW/cm/K that is far above the values obtained for other elements and compounds. The only problem occurs when the sample gas contains hydrogen, since it is the only one that has a thermal conductivity (1910 mW/cm/K) relatively close to that of He. Two similar thermal conductivity values affects the electric signals, and thus the analyzer response. In order to avoid this phenomenon, it is possible to use argon as carrier gas that has a much lower thermal conductivity (189 mW/cm/K), or nitrogen (277 mW/cm/K) at the expense of a more accurate calibration requirement. Other possible disadvantages arises when corrosive substances are used, in fact their presence may damage the resistors. Anyway, after this brief review about gas sensing methods, the gas analyzer exhibits as final result the concentration values of all the five detectable chemical species (reported in ppm) second by second.

3.2 – Preliminary procedures

Before starting any experiment, the first step is the phase of charging the reactor. However, before opening the reactor by removing the flange, it must be ensured that all gas lines are closed and that the reactor has been previously purged by flushing nitrogen or argon for a few minutes in order to push out any other gases left in the reactor during previous experiments. Then, the flange is removed and a new sample is weighted and consequently placed in the alumina crucible (Figure 3.3 b) which in turn is located at the center of the tubular microreactor. If that crucible has already been used before, it must be properly cleaned of any residues, subsequently the new sample can be placed in it. Obviously, during the microreactor charge phase the power supply unit must to be turned off and the reactor has to be at ambient temperature. Subsequently, the flange of the charged reactor is closed, and a leak test is carried out. The outlet line of the entire system is connected to a flowmeter, and a certain gas flow is sent in the system. If the flowmeter measured values show a loss lower than 10% with respect to the expected value, it means that that the leakage can be considered acceptable. Once also this phase has been done, the outlet gas line is connected again to the gas analyzer, then the temperature program and the gas flow sequences are set. The last step is the gas

analyzer calibration. Every channels range has to be modified on the basis of what the expected reading concentrations will be, and then the zero value and the maximum range value reading has to be verified, sending in the gas line the respective concentrations. Once also this last step is successfully done, the last thing to do is to start the programs through the respective software and the gas analyzer data reading process.

Chapter 4

4 – Microreactor tests and results

4.1 – SFNM04 as oxygen carrier for chemical looping processes

SFNM04 is the perovskite-based redox material investigated in this work. The study of $Sr_2FeNi_{0.4}Mo_{0.6}O_{6-\delta}$ is the main object of the University of Udine "PRIN17 – Direct Biopower" project [124]. The evaluation of SFNM04 electro-catalytic properties is the main goal of this project. However, the first step is the material synthesis starting from the $Sr_2Fe_{1.5}Mo_{0.5}O_{6-\delta}$ double perovskite. Generally, double perovskites are indicated as $A_2(BB')O_6$, where A represents an alkali-earth metal and B, B' stand for transition metals and in this case Fe and Mo are the two transition metals occupying the B and B' sites, respectively. The atomic arrangement shows Sr atoms placed in the hollow between the alternating $FeO_{6/2}$ and $MoO_{6/2}$ corner-shared octahedra [125] forming a cubic structure (Fm3m) (Figure 4.1). Sr_2FeMoO_6 shows promising properties among the double perovskite materials especially in terms of magnetoresistance (MR) [127, 128]. Besides this aspect, many other properties have been listed by UniUD for $Sr_2Fe_{1.5}Mo_{0.5}O_{6-\delta}$ double perovskite, such as: high electronic and ionic conductivities, good stability at high temperatures and in both reducing and oxidizing ambient. The good electronic conductivity is manly caused by the coexistence of mixed redox species with different valence states Fe^{2+}/Fe^{3+} and Mo^{6+}/Mo^{5+}, while the ionic conductivity is mainly due to the disequilibrium of the redox couples, for this reason

a high content of oxygen vacancies in the lattice is achieved in order to establish the electroneutrality in the perovskite material.

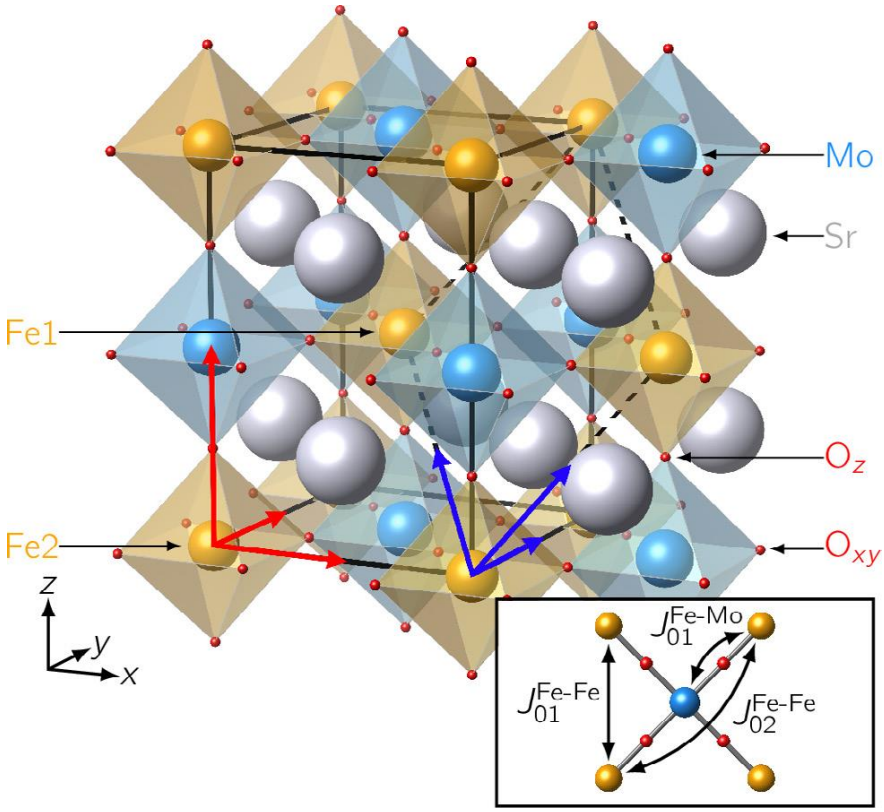

Figure 4.1: *SFMO double-perovskite structure. The dashed lines represents the primitive cell [126].*

Song et al. [129] investigated the effects of cobalt doping on $Sr_2Fe_{1.5}Mo_{0.5}O_{6-\delta}$ with the objective of employing $Sr_2Fe_{1.5-x}Co_xMo_{0.5}O_{6-\delta}$ (x=0, 0.5, 0.75, 1) in an intermediate temperature symmetrical solid oxide fuel cell (IT-SOFC). The results show that for x=0.75 it is possible to achieve a higher specific surface area (smaller grains), an improved catalytic activity, and a higher content of oxygen vacancies. Nevertheless, undoped $Sr_2Fe_{1.5}Mo_{0.5}O_{6-\delta}$ was widely studied and the various data demonstrated that it is a promising material as electrode for SOFCs [130, 132] and SOECs [131]. UniUD synthetized Ni-doped $Sr_2Fe_{1.5}Mo_{0.5}O_{6-\delta}$ and then investigated the effect of Ni doping on the catalytic properties and performances. Then, the same material has been analyzed in this work in terms of redox ability with the goal of producing CO in a chemical looping process during the CO_2

splitting step. The use of Ni arises from the need to improve the catalytic properties of ceramic materials by incorporating nanostructured catalysts such as Pt and Ni. There are several methods to incorporate nanoparticles successfully. One of these is the well-known traditional infiltration which however has some limitations, it is expensive and does not ensure good control of the morphology. Alternatively, in situ growth of nanoparticles from ceramic materials shows various advantages, with respect to traditional impregnation method [135], such as nanoparticles uniform distribution, it is a time- and cost-effective, and less affected by backbones properties [133]. Generally, Ni^{2+} tend to occupy Fe^{2+} sites substituting it in the lattice. In this way an enhanced electronic conductivity is observed, and it is mainly due to the higher conductivity of the inserted Ni^{2+} and to the Fe^{2+}/Fe^{3+} ratio change. The main peculiarity of this material is the occurrence of the exsolution phenomenon. In a few words, it is observed the spontaneous formation of Ni-Fe alloy nanoparticles on the lattice surface due to the exsolution of Ni and Fe that occurs predominantly in reducing environments and from a certain temperature onwards. The exsolution has been found to have a crucial role in the improvement of the material's electro-catalytic properties, performances, and stability. In literature several synthetization methods have been investigated such as: one-step combustion method with glycine and citric acid [134], microwave-assisted combustion method [130], citric nitrate combustion method [133], solution route with citric acid and ethylenediaminetetracetic acid (EDTA) [136]. In this case the sample has been synthetized via Self-Combustion Synthesis (SCS) with citric acid, then the powders were calcinated at more than 1100°C in order to obtain a cubic structure [124]. UniUD decided to synthetize samples with different Ni content and from an X-ray diffraction analysis (XRD) it was possible to notice that there exists a Ni solubility limit in the lattice. This upper limit is equal to x = 0.5, namely $Sr_2FeNi_{0.5}Mo_{0.5}O_{6-\delta}$ (SFNM05), in fact at this Ni content value SFNM-0.5 presents NiO segregation on the surface, this means that part of the inserted Ni failed to enter in the lattice. On the other hand, for Ni content of x = 0.4 no NiO segregation occurs. However, undoped samples were synthesized as reference materials: $Sr_2Fe_{1.5}Mo_{0.5}O_{6-\delta}$ and Sr_2FeMoO_6. The latter is quite challenging to be synthesized because of the segregation of an insulant phase, $SrMoO_4$. Liu et al.

[130] investigated this aspect concluding that Sr_2FeMoO_6 can be successfully synthesized only in a reducing environment. Taking heed of this insight, it has been observed a $SrMoO_4$ segregation also for low Ni content samples, however the segregation diminishes considerably for x ≥ 0.35 (Figure 4.2) and a pure cubic structure is obtained [133].

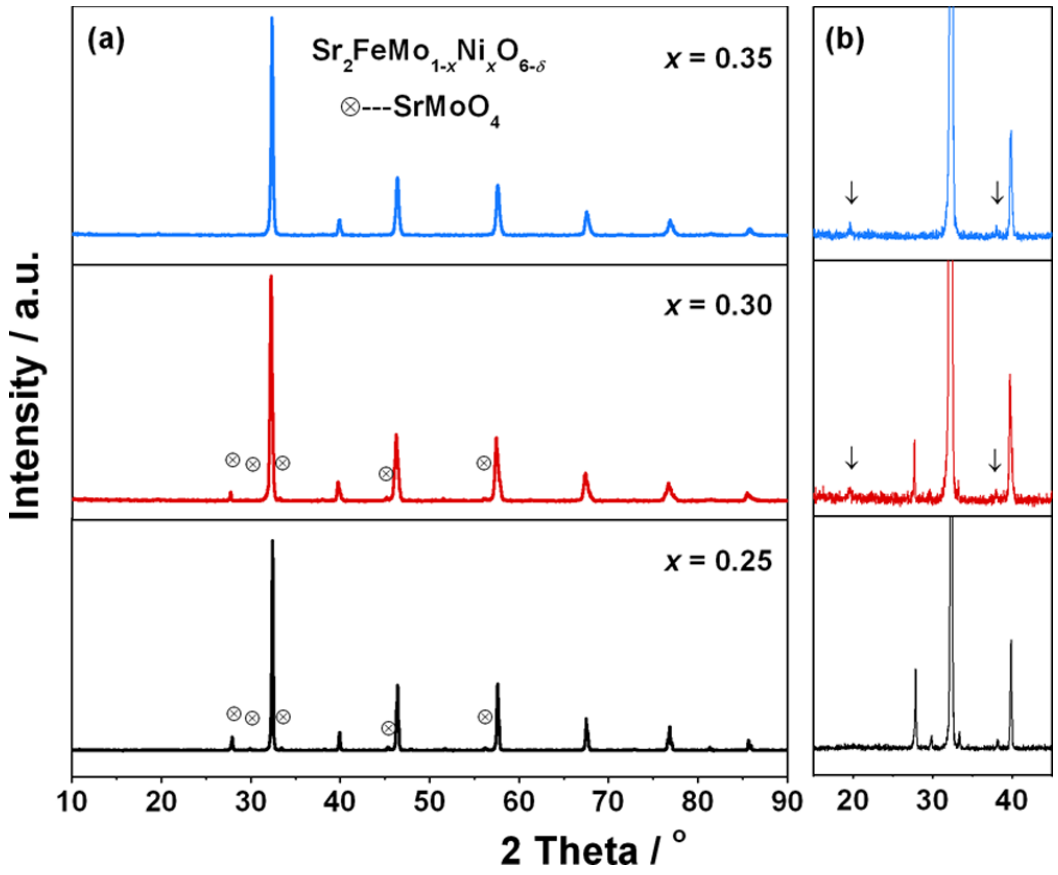

Figure 4.2: *XRD at room-temperature for* $Sr_2FeNi_xMo_{1-x}O_{6-\delta}$ *(x=0.25, 0.30, 0.35) [133].*

Furthermore, the average grain size tends to decrease as the Ni content increases implying a larger specific surface area and an improved redox activity [136]. In addition, an X-ray photoemission spectroscopy (XPS) and an energy dispersive X-ray (EDX) analysis have been performed for SFNM-04 resulting in a slight Sr segregation on the surface of the structure. A Temperature Programmed Reduction (TPR) has been carried out for SFNM-04 in order to further analyze the material cyclical redox ability. The steps composing the TPR test are reported in the following list [124]:

1. Thermal pre-treatment up to 500°C (10°C/min) in air. It has the function of removing any impurity;
2. Isothermal step at 500°C for 1 hour;
3. TPR step consisting in a temperature ramp from 500°C to 900°C (10°C/min) in a mixture of H_2 (4.5%) and N_2 (35 mL/min);
4. Ramp down to ambient temperature in N_2;
5. Sample re-oxidation from room temperature to 500°C in air (point 1).

Analyzing the data obtained from the four TPR cycles it is possible to notice how the hydrogen consumption trend changes in the second reduction with respect to the first one. In fact, from the second reduction onwards, the curves exhibit the same behavior and they follow the same trend indicating that a higher stability has been achieved.

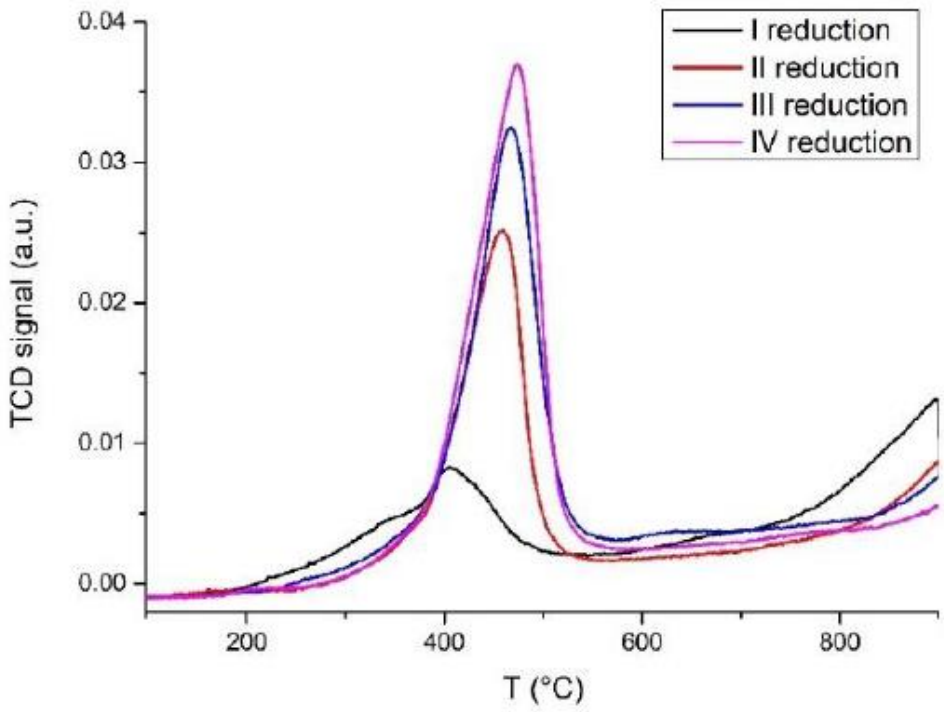

Figure 4.3: *TPR analysis of SFNM-04 in (4.5%) H_2/N_2 [124].*

The different trend obtained during the first cycle may be attributed to the occurrence of a transition phase. In order to fully understand this aspect, a XRD

analysis has been performed and it has confirmed the presence of a transition phase, more precisely, a Ruddlesden-Popper (RP) phase indicated as $Sr_3FeMoO_{6.5}$. However, this is not an absolute transition but, from the XRD analysis, the RP phase and double perovskite phase are both detected, so they are simultaneously present in the global perovskite structure. There are various Ruddlesden-Popper phases indicated as $A_{n+1}B_nX_{3n+1}$, some examples are reported below in Figure 4.4 where the RP phase is represented by one or more perovskite layers encompassed between rock-salt layers.

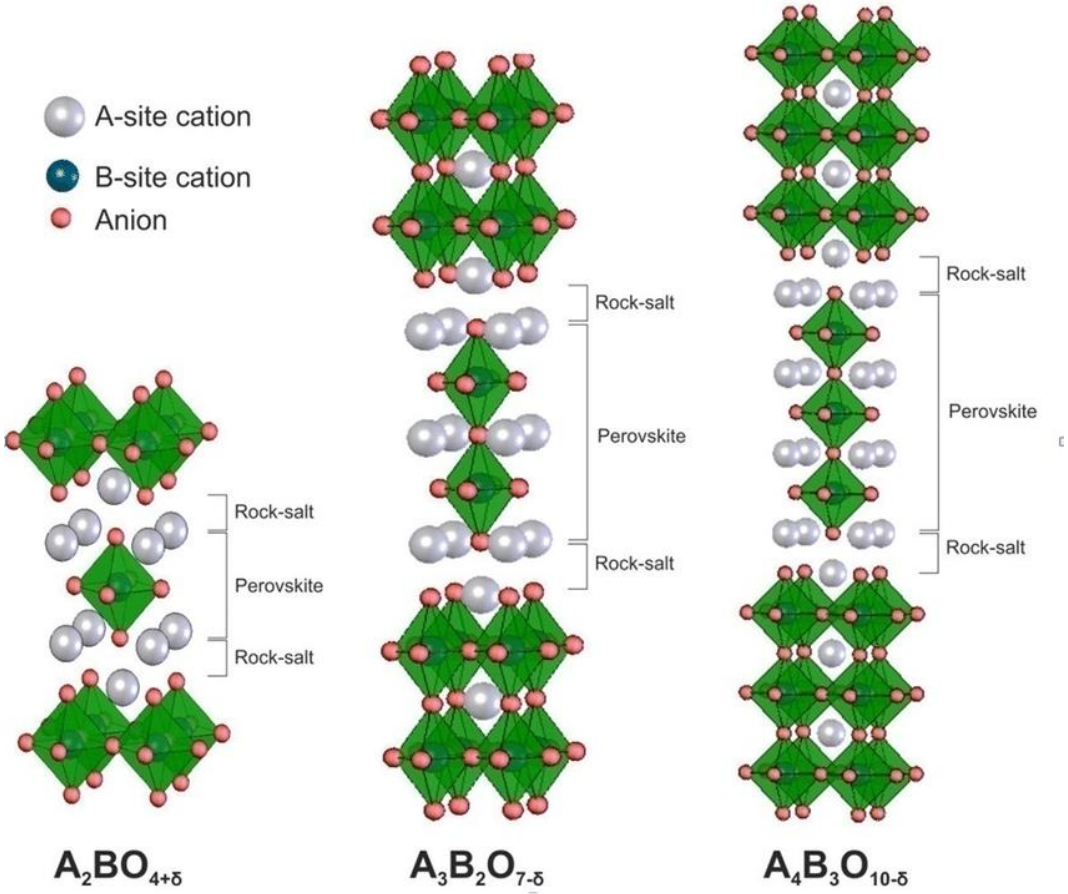

Figure 4.4: *Ruddlesden-Popper perovskite structure with varying ABO_3 layer number. (Right) n=1, (Middle) n=2, (Left) n=3 [137].*

However, beside the RP signals, the formation of $FeNi_3$ was detected on the surface through XRD analysis. This can be explained as a consequence of the exsolution process in reducing atmosphere, where both Ni and Fe are reduced and then move towards the surface where the $FeNi_3$ alloy is generated. It is possible to see it in the

magnification in Figure 4.5 below. The $FeNi_3$ alloy peak signal (44.5°) shows an area under the curve that tends to grow as the number of cycles increases, while the RP phase shows the opposite trend. This is a clear signal of the exsolution progress during the reduction steps.

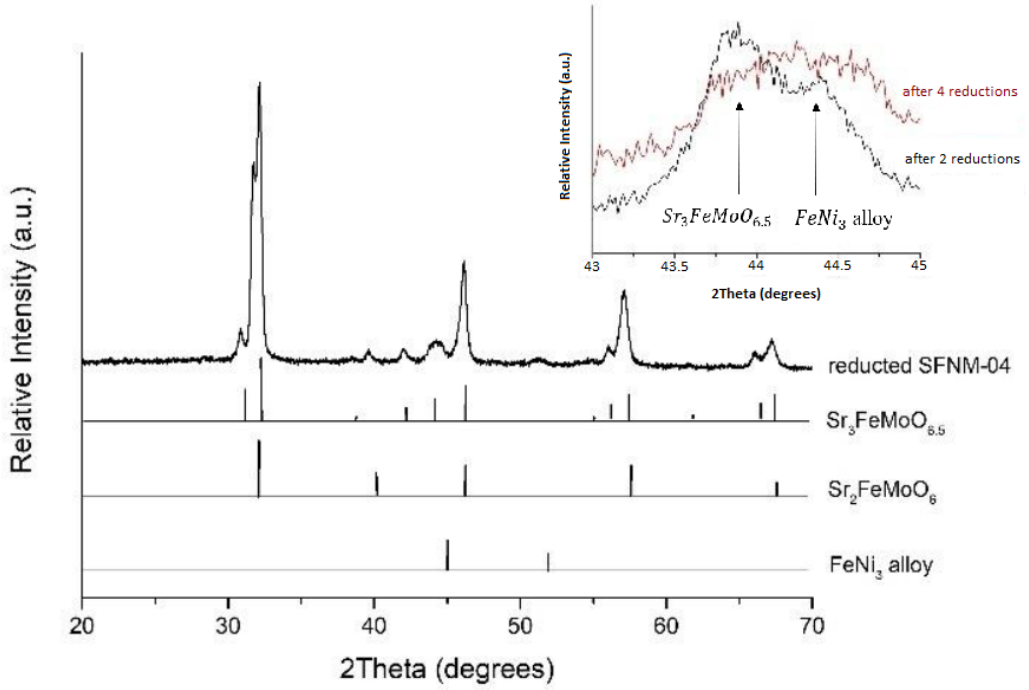

Figure 4.5: *XRD of SFNM04 after 4 reduction steps, with distinct phase identification; magnification in the range 43°-45° with comparison between SFNM-04 after 2 and 4 reductions*

.

At this point, also the increasing H_2 consumption observed during the previous TPR test can be explained as consequence of the structural changes occurring in the perovskite structure. The peak reported in Figure 4.3 at around 450°C - 500°C is correlated to the alloy reduction and the reduction, in the RP structure, of Fe^{3+} and Mo^{6+}. Furthermore, a stability test in CO_2 environment was performed and it was pointed out that the Ni presence in SFM lattice provokes the stabilization of $SrMoO_4$ and the formation of $SrCO_3$. In order to better understand this phenomenon a XRD analysis was carried out for two SFNM-04 samples. The two samples were differently treated before to perform the XRD analysis, the first sample was left for a year reacting only with atmospheric CO_2 at room temperature (SFNM04), the

other one was treated for 2 hours in 30% C_3H_8/N_2 at 800°C (SFNM04, prop). In a few words, both the samples have been subjected to a degradation process. The XRD results show a poor stability of SFNM-04 when placed to a hydrocarbon environment with the consequent degradation and formation of the insulant phase $SrMoO_4$ and the carbonate $SrCO_3$ due to the presence of nickel that catalyzes the hydrocarbon cracking. A TGA was performed for the two samples resulting in a significant loss of weight for "SFNM04, prop" due to the carbonate decomposition occurring in the temperature range 471°C - 653°C (Figure 4.6).

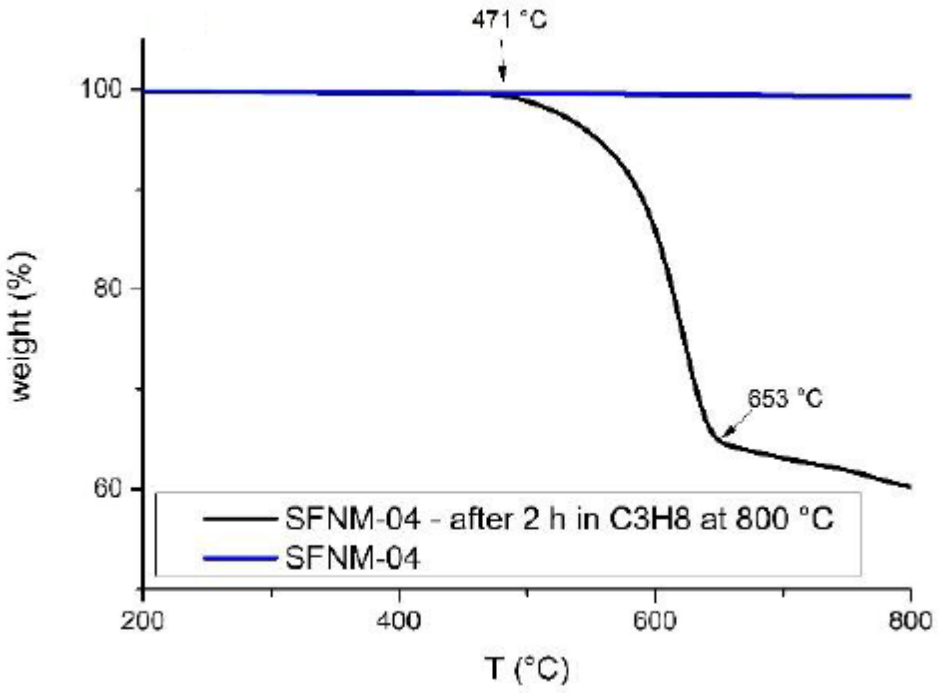

Figure 4.6: *TGA for untreated "SFNM04" (blue curve) and "SFNM04, prop" (black curve).*

It is observed that a thermal treatment allows to make $SrCO_3$ disappear and also a decrease in $SrMoO_4$was detected. Finally, with a last calcination step at 900°C in air also the low content of $SrMoO_4$ is reabsorbed in the lattice restoring the original perovskite phase. Finally, oxy-dry reforming (ODR) catalytic tests were performed that show better results with respect to dry reforming. These tests involve an 80 mg sample and a gas flow composed by CH_4 and CO_2 (3:2). The sample was pre-treated in reducing atmosphere in H_2 for 1 hour at 800°C, and kept at 700°C in reducing

environment for 12 hours. The CO_2 conversion has an inflection between 550°C and 600°C, while the CH_4 conversion tends to increase as direct consequence of methane combustion with oxygen. Then, between 600°C and 650°C a reducing conversion of both CH_4 ad CO_2 occurred. Concluding, this test revealed a low catalytic activity in case of oxy-dry reforming due to small surface area of the powder sample [124].

4.2 – Experimental tests

The SFNM04 powder was prepared and then tested in the microreactor setup described in the previous chapter. The analysis is mainly based on redox reactions and the analysis of the gas flow composition of the mixture exiting the microreactor after reacting with the perovskite sample. The gas analyzer, as already described, is connected to the reactor outlet gas line and provided the measure in ppm of the species contained in the final gas mixture. The main goal in our case is to analyze the *CO* production achieved during the oxidation step, and this represents the focus of all performed tests. Obviously, before each test, an analyzer calibration phase (exploiting the by-pass line) is carried out in order to have the most reliable measurements possible; the zero value for all the channels was fixed while flushing in the gas lines a nitrogen flow in order to reach flat signals and fix the zero value by calibrating the instrument. On the other hand, the maximum value was selected for each signal on the basis of the specific test, since in many cases the percentages of CO_2, in the oxidation step, and H_2, in the reduction step, was changed and modified so that the various behavior and responses to different parameters could be analyzed. Finally, once the instrument had been calibrated, it was possible to send a mixture with various compositions to make sure the analyzer responded properly. The various tests performed were reported below, and they have been schematically reported in Table 1 and 2.

Table 1: *List of tests performed for SFNM's oxidation investigation.*

Test ID	T [°C]	Gas Compositions	Number of cycles	Reactions time	Total flux [Nml/ min]
TEST(I)	Isothermal 850°C	Oxy: 20% CO_2 Red: 10% H_2	5	Oxy: 90 min Red: 1 hour	200
TEST(II)	T_{ox}=550, 650, 750, 850°C T_{red}=850°C	Oxy: 20% CO_2 Red: 10% H_2	5	Oxy: 30 min Red: 1 hour	200
TEST(III)	Isothermal at 850°C (3 cycles) and at 750°C (3 cycles)	Oxy: 20-40% CO_2 Red: 10% H_2	6	Oxy: 30 min Red: 1 hour	200
TEST(IV)	Isothermal at 850°C (10 cycles) and at 750°C (10 cycles)	Oxy: 6-100% CO_2 Red: 10% H_2	10 + 10	Oxy: 30 min Red: 1 hour	200
TEST(V)	T_{ox}=750°C T_{red}=850°C	Oxy=6-100% CO_2 Red: 10% H_2	10	Oxy: 30 min Red: 1 hour	200

Table 2: *List of tests performed for SFNM's reduction investigation.*

Test ID	T [°C]	Gas Compositions	Number of cycles	Reactions time	Total flux [Nml/ min]
TEST(VI)	T_{ox}=850°C T_{red}=550, 650, 750, 850°C	Oxy: 20% CO_2 Red: 10% H_2	5	Oxy: 30 min Red: 1 hour	200
TEST (VII)	Isothermal at 850°C (10 cycles) and at 750°C (10 cycles)	Oxy: 20% CO_2 Red: 5-100% H_2	10+10	Oxy: 30 min Red: 1 hour	200
TEST (VIII)	T_{ox}=750°C T_{red}=850°C	Oxy: 20% CO_2 Red: 5-100% H_2	10	Oxy: 30 min Red: 1 hour	200
TEST(IX)	Isothermal at 850°C	Oxy: 20% CO_2 Red: 10% H_2	6	Oxy: 30 min Red: 15, 30, 40, 60, 90, 120 min	200
TEST(X)	Isothermal at 850°C	Oxy: 20% CO_2 Red: 100% H_2	1	Oxy: 7 hours Red: 2 hours	200

4.2.1 – TEST(I): 5 isothermal cycles at 850°C

In this first step a SFNM sample was employed in order to evaluate its cyclic stability performing five identical isothermal cycles at 850°C. Before the first redox

cycle a pre-treatment step in air at 500°C was performed in order to obtain a fully oxidized sample and avoiding the presence of any contaminants. Then the temperature varies from 500°C to 850°C with a ramp having a rate of 10 K/min. A single isothermal cycle consisted of four sequences:

- Purge in N_2 for 5 minutes;
- Reduction step with a gas flow composition of 10% H_2 in N_2 for 1 hour;
- Purge in N_2 for 5 minutes;
- Oxidation step with 20% CO_2 in N_2 for 90 min;

In order to identify the *CO* production rate [μmol/g/s] and the yield [μmol/g], two methods have been considered: the total integral of the production curve, and the integral of the curve after cutting the tail as explained below. Once plotted the *CO* produced during the oxidation step (example in Figure 4.7) the tail never reached the values observed before the peak, but it seems to stabilize at around 1,400 ppm. However, in order to avoid this tail affects the measurement of the *CO* yield, the derivative has been exploited, taking as breaking point to calculate the yield the value in which the derivative tends to stay between a fixed tolerance. The decided tolerance value is quite conservative and was fixed at 0.05%. This means that when the derivative variation between one average value and the next is lower than 0.05% than we could consider that the tail has reached a constant value.

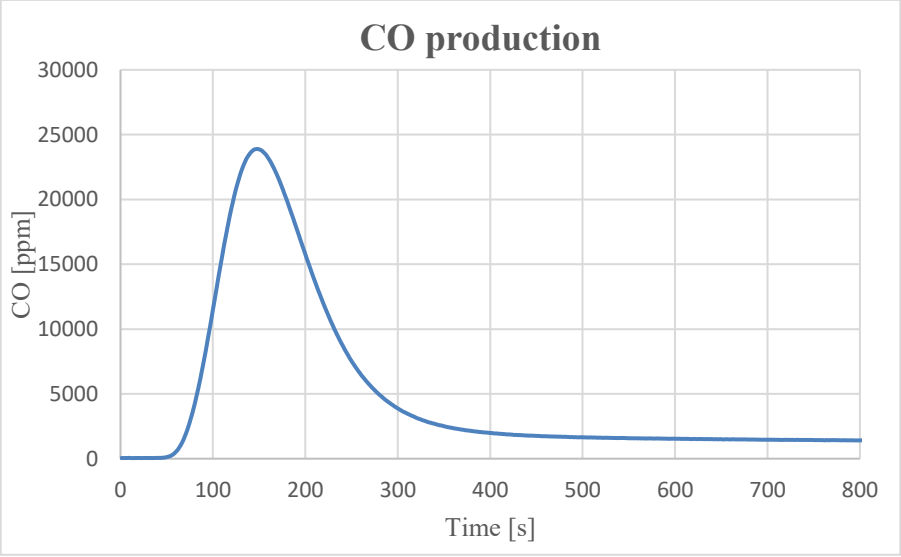

Figure 4.7: *CO production during oxidation step with 20% CO_2/N_2.*

Once obtained the time instant at which the peak can be considered concluded, a straight line has been drawn (Figure 4.8a) and the difference between the curve representing the *CO* production and the straight line has been calculated obtaining the net production according to the assumption made (Figure 4.8b).

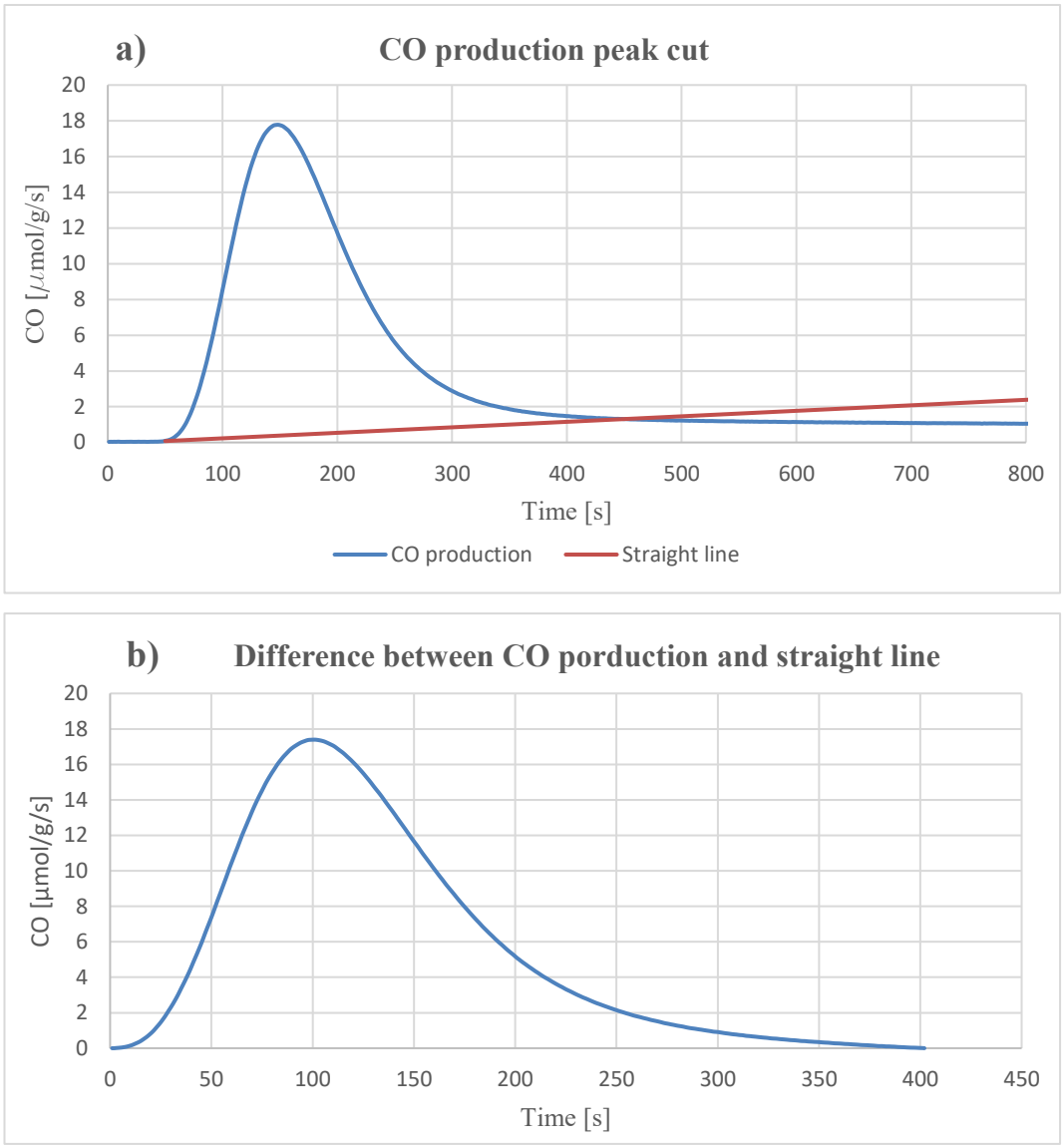

Figure 4.8: *(a) Straight line cutting the CO production curve; (b) Delta CO production subtracting the straight line to the CO production curve.*

This method has been used for all the tests carried out, however in some cases the entire area under the *CO* production curve has been considered also as additional

way to compare the results. The results obtained from the isothermal test are reported in terms of *CO* production rate and yield in Figure 4.9.

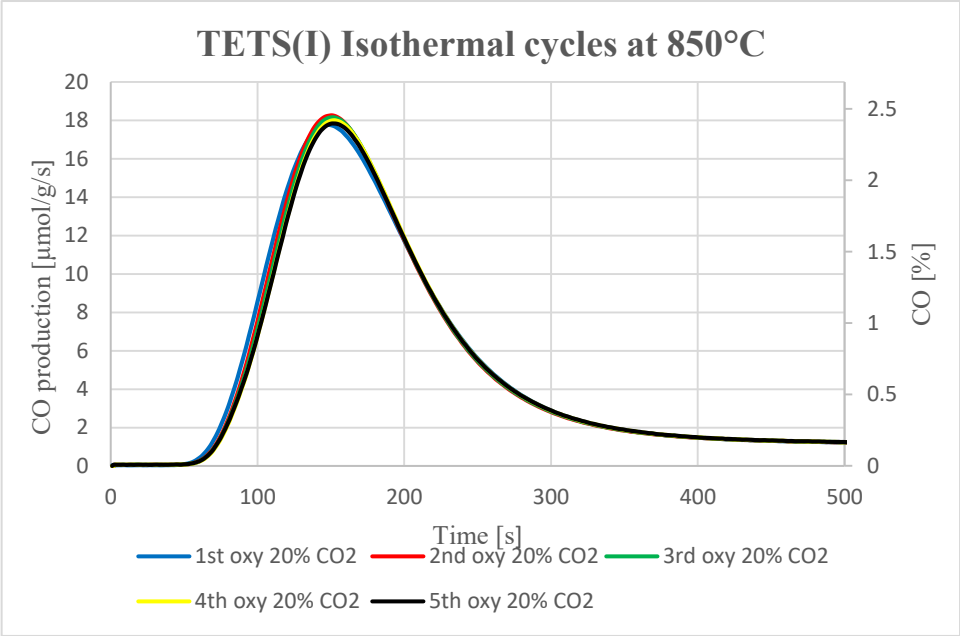

Figure 4.9: *TEST(I) CO production during 5 isothermal cycles, oxidation step carried out with 20% CO_2.*

Under the fixed conditions, the sample response remain the same during the five cycles exhibiting a good stability and repeatability throughout the whole process. The sample used has a mass of 200 mg, and the gas mixture has been kept at 200 Nml/min. In all the cycles the peak is considered to be concluded after 450 seconds from the oxidation step beginning, namely the introduction of CO_2 in the reactor.

Table 3: *Oxidation results for TEST(I): global yield, max CO produced, converted CO_2.*

Cycle	*CO [μmol/g]*	*Max CO [%]*	*CO_2 conversion [%]*
1	2248,427	2.39	11.95
2	2210.002	2.45	12.27
3	2190.708	2.44	12.21
4	2178.917	2.42	12.10
5	2165.093	2.40	12.00

The peak values obtained are all around 18 μmol/g/s, corresponding to a *CO* percentage of about 2.4% and a CO_2 conversion of 12%. The curves show all the same trend, and thus the kinetic also is comparable in all the cycles. The results of each cycles are listed in Table 3.

4.2.2 – TEST(II): 5 cycles at different oxidation temperatures

In this test 5 cycles have been performed varying the oxidation temperature from 850°C to 550°C (Figure 4.10). The first and the last cycles have been carried out with oxidation steps at 850°C, while the other three oxidations were performed at 550°C, 650°C, and 750°C, respectively. The reduction was kept constant at 850°C with 10% H_2/N_2, while the oxidizing gas flow was composed by 20% CO_2/N_2. As usual, the first step is a pre-treatment at 500°C in air, then there is a ramp up that leads to 850°C while flushing N_2 in the reactor. The other steps are listed below:

- Reduction at 850°C in 10% H_2/N_2 for 1 hour (1-2-3-4-5);
- Purge in N_2 for 10 minutes (1), cooling up to 550°C (2), 650°C (3), 750°C (4), purge of 10 minutes (5);
- Oxidation at 850°C (1), 550°C (2), 650°C (3), 750°C (4), 850°C (5) in 20% CO_2/N_2 for 30 minutes;
- Purge in N_2 for 10 minutes (1), heating back to 850°C (2-3-4), ramp-down up to room temperature in N_2 (5 – end of the process).

At first glance, it is immediately evident that the first cycle, performed at the same identical operating conditions of the previous test, shows values of *CO* production rate similar to those obtained in the cycles of TEST(I) (Figure 4.9) demonstrating, once more, a good repeatability. Then, at lower oxidation temperatures the curves exhibit a slower trend suggesting that the fixed temperature values imply a slow reaction kinetics causing a lower *CO* yield. In fact, as the oxidation temperature increases, the *CO* yield and peak are both higher and the redox ability seems to be improved. Finally, the last cycle is performed at the same conditions of the first one, and in fact it shows the same trend, meaning that the previous low temperature oxidations did not negatively affect the material reactivity.

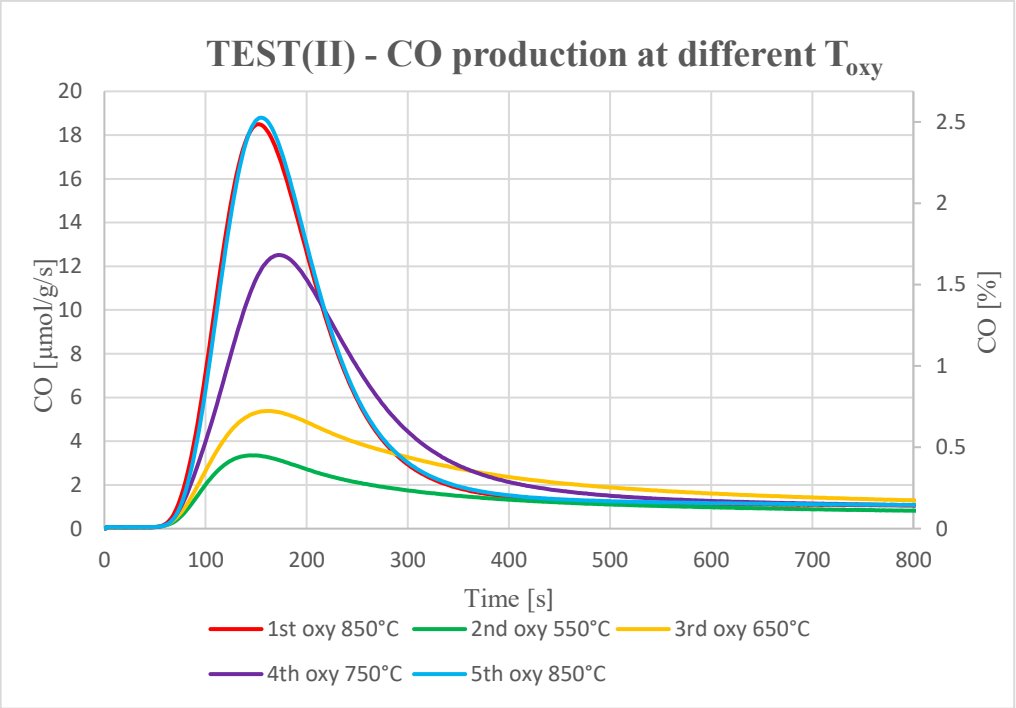

Figure 4.10: *Test(II) CO production rate in oxidation steps performed at 550°C-850°C with 20% CO_2/N_2, reduction reactions carried out at 850°C with 10% H_2/N_2.*

According to the data reported in Table 4, it is noticed how the two first and last cycles exhibit very similar performances, whereas the oxidation steps at lower temperature show a lower *CO* yield and also a lower CO_2 conversion due to slower kinetics.

Table 4: *Oxidation results for TEST(II): global yield, max CO produced, converted CO_2.*

Cycle	***T_{oxy} [°C]***	***CO [μmol/g]***	***Max CO [%]***	***CO_2 conversion [%]***
1	850	2276.233	2.49	12.43
2	550	825.272	0.45	2.25
3	650	1534.092	0.72	3.62
4	750	1863.529	1.68	8.41
5	850	2274.428	2.53	12.63

At 850°C the global *CO* yield is almost three times higher than that obtained at 550°C, while the percentage of CO_2 converted at 850°C is six and four times higher than that at 550°C and 650°C, respectively. According to this test, a higher temperature allows to achieve a better performance, however it is important to remember that the recent focus on perovskite material as alternative oxygen carrier for thermochemical cycles lies on the objective of reducing the operating temperatures of the entire process to make it more reliable. In this regard, one of the main challenges in thermochemical cycle processes is the high temperature, and for this reason it is important to stay below certain limits. In addition, at higher temperatures levels there are already materials able to outperform perovskite-based oxygen carriers, like ceria, so it is important to investigate low temperature ranges and find new promising materials that require lower temperature facilitating the integration with solar thermal energy. On the other hand, if the operating temperature is too low, especially during the oxidation step, beside the bad performances, another significant issues is related to the formation of carbonates by the CO_2 adsorption on Sr. Their presence heavily affects the ability to produce *CO* since the CO_2 gas flow participates in the carbonates formation rather than dissociate and convert to *CO*. Nevertheless, in this second test it was pointed out that the oxidation temperature plays a crucial role in terms of redox performance and catalytic activity, mainly affecting the reaction kinetics.

4.2.3 – TEST(III): Isothermal cycles with varying CO_2 concentration (20-40%)

In this test six cycles have been performed, the first three cycles are carried out at 850°C, while the last three at 750°C. Globally, there are two isothermal processes at different temperature levels. The oxidation steps are 30 minutes long, while the reduction steps last 1 hour. The parameter varied was the CO_2 concentration in the oxidizing gas mixture and its value ranges between 20-40%. Therefore, the first three cycles are carried out at 850°C with 20%, 30%, and 40% of CO_2 in N_2, respectively. Same thing for the last three cycles, with the only difference

represented by the temperature (750°C). The six cycles have all been reported together in the same graph, see Figure 4.11.

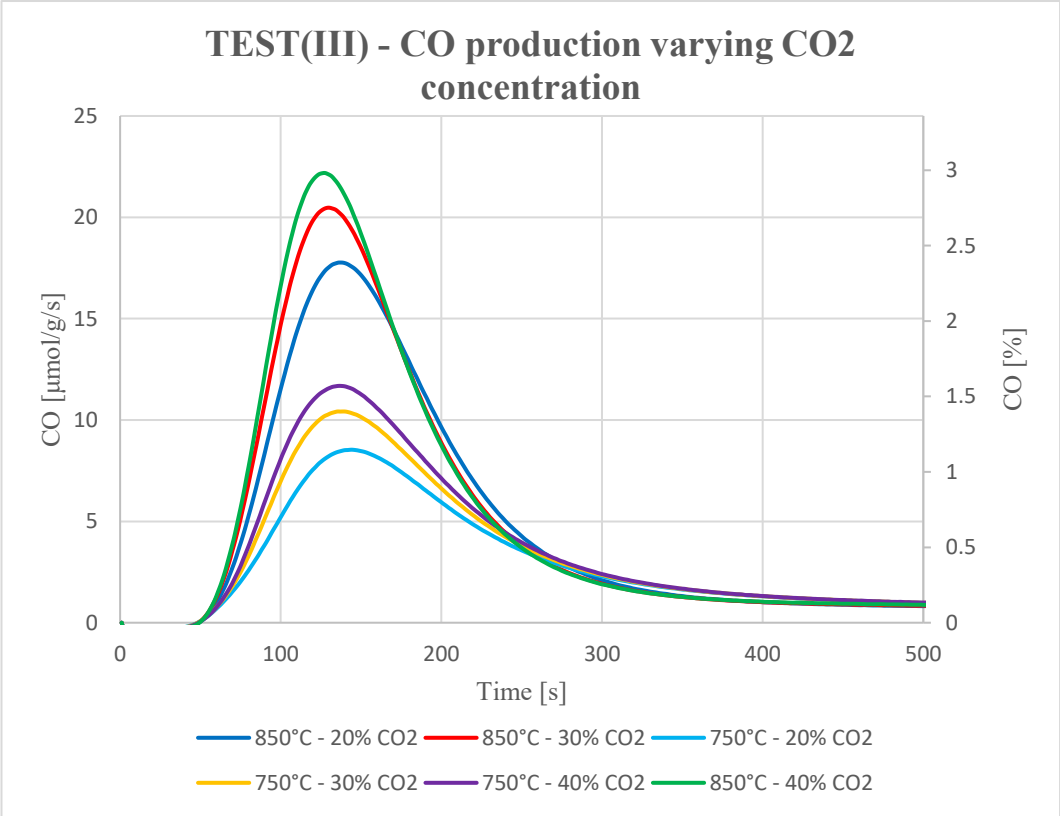

Figure 4.11: *TEST(III) CO production rate performed in isothermal conditions; three cycles obtained at 850°C, the remainder performed at 750°C; CO_2 concentration varying in the range 20-40%.*

From the results, it is noticed how the three cycles performed at 850°C show higher peaks and a faster production reaction if compared to those obtained at 750°C. However, another important aspect is the influence of the different CO_2 content in the oxidizing gas mixture. As the CO_2 concentration increases, the CO production increases as well, reaching a higher maximum value (see Table 5). A higher amount of CO_2, in the microreactor, ideally favors the re-oxidation of the sample producing *CO* and facilitating the occupation of the oxygen vacancies generated during the reduction step. Moreover, the production peak tends to slightly shift leftwards when the CO_2 increases, suggesting a faster reaction kinetics and highlighting that the oxidation step is favored when the partial pressure of the oxidant increases. Comparing the integral values at fixed CO_2 concentration and varying the oxidation

temperature it is possible to notice that at 750°C the values are almost 25% lower than those obtained at 850°C. Moreover, the maximum *CO* production rate and the CO_2 conversion, at 850°C and fixed CO_2 content, are two times higher if compared to the results at 750°C. The 100°C increase of temperature has a huge impact on the redox ability of the perovskite sample. Beside the temperature influence, also the CO_2 content variation leads to significant differences among the measured values. However, the differences showed in the measured data when varying the oxidation temperature are remarkable, indicating that the temperature influence is crucial in terms of reaction kinetic and redox activity. Especially when using SFNM, the temperature play an important role since it has to be high enough, in case of oxidation, in order to reduce the possible carbonates formation that are typically produced when using material containing elements like Sr. This test represents only a preliminary investigation of the CO_2 percentage influence on the performances and the redox activity of the sample. In fact, the entire range of possible percentages has been analyzed, from 6% up to 100% of CO_2 as oxidizing gas. More precisely, two tests have been performed which the only difference is the temperature program.

Table 5: *Oxidation results for TEST(III): global yield, max CO produced, converted* CO_2.

Cycle	T_{oxy} ***[°C]***	CO_2 ***[%]***	***CO [μmol/g]***	***Max CO [%]***	CO_2 ***conversion [%]***
1	850	20	2183.249	2.39	11.94
2	850	30	2223.767	2.75	9.17
3	850	40	2341.243	2.98	7.46
4	750	20	1444.416	1.15	5.74
5	750	30	1634.311	1.40	4.67
6	750	40	1789.173	1.57	3.93

4.2.4 – TEST(IV): Isothermal cycles with different concentration of CO_2 (6-100%)

The variation of CO_2 content has been investigated in two distinct ways: ten isothermal cycles at 850°C, and ten isothermal cycles at 750°C. Both the processes, as already said, consists of ten redox cycles, each cycle is composed by oxidation and reduction steps carried out at 750°C, the reduction steps are performed in 10% H_2/N_2 for 1 hour, while the oxidizing gas mixture has different compositions with the amount of CO_2 ranging between 6% and 100% for 30 minutes. The results regarding the *CO* production are reported in Figure 4.12.

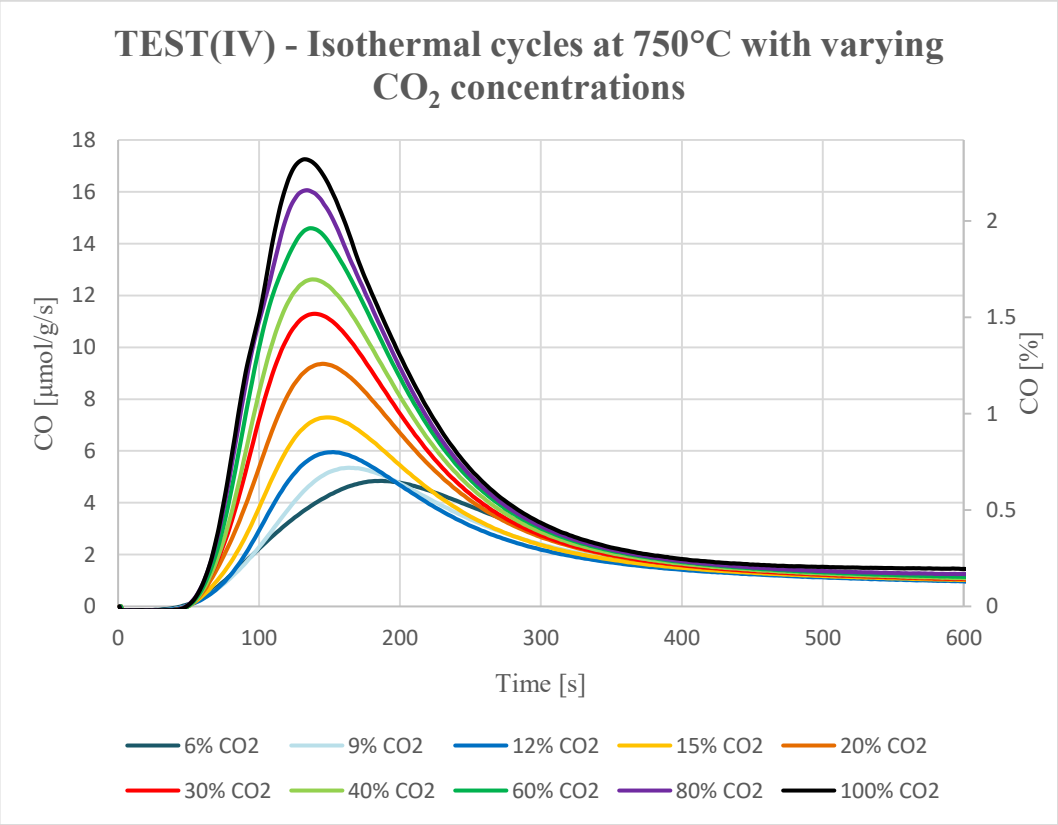

Figure 4.12: *TEST(IV) CO production rate for isothermal process at 750°C with varying CO_2 content (6-100%).*

As for the previous test, the increasing CO_2 content leads to a higher *CO* yield and the values corresponding to 20%, 30%, and 40% are similar to those obtained in the TEST(III). The maximum *CO* production rate value is around 17 μmol/g/s, with a

global yield of 2269.63 μmol/g that are slightly lower if compared to the values obtained during the oxidation steps performed at 850°C with 20% of CO_2 (Table 6). Therefore, even though a 100% CO_2 gas flow is used during the oxidation step, it results in a redox performance already achievable at 850°C with only 20% of CO_2 content. In general, in Figure 4.12, it is noticed the same behavior of the previous test, thus the increasing CO_2 amount in the oxidizing gas mixture affects the reaction increasing the kinetics and promoting a larger CO production.

Table 6: *Oxidation results for TEST(IV) at 750°C: global yield, max CO produced, converted* CO_2.

Cycle	***CO_2 [%]***	***CO [μmol/g]***	***Max CO [%]***	***CO_2 conversion [%]***
1	6	1114.650	0.65	10.85
2	9	1118.019	0.72	7.99
3	12	1138.694	0.80	6.67
4	15	1193.606	0.98	6.54
5	20	1499.687	1.26	6.29
6	30	1723.395	1.52	5.06
7	40	1895.495	1.70	4.24
8	60	2110.649	1.96	3.27
9	80	2157.806	2.16	2.70
10	100	2269.629	2.32	2.32

The same test has been performed fixing the isothermal temperature at 850°C (Figure 4.13). Also in this test, as the CO_2 content increases a CO production rate increase is detected. However, the curve tends to shrink when the CO_2 increases, revealing a faster reaction kinetics. Anyway, the differences in CO peak production are larger for low CO_2 concentrations and slighter from 60% to 100% of CO_2. In Table 7 the values as measured from the gas analyzer are reported indicating a much higher CO yield with respect to the process performed at 750°C.

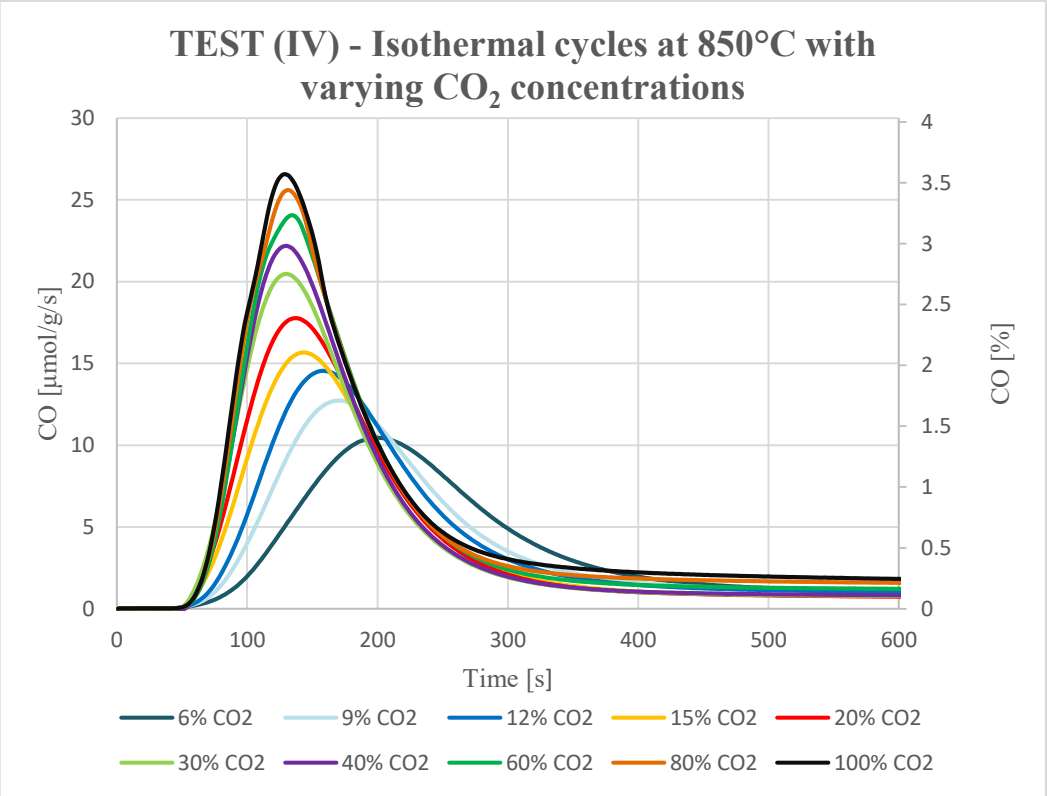

Figure 4.13: *TEST(IV) CO production rate for isothermal process at 850°C with varying CO_2 content (6-100%).*

Table 7: *Oxidation results for TEST(IV) at 750°C: global yield, max CO produced, converted CO_2.*

Cycle	*CO_2 [%]*	*CO [μmol/g]*	*Max CO [%]*	*CO_2 conversion [%]*
1	6	1800.420	1.41	23.43
2	9	1936.536	1.71	19.01
3	12	2027.047	1.96	16.29
4	15	2090.292	2.11	14.04
5	20	2183.249	2.39	11.94
6	30	2223.767	2.75	9.17
7	40	2341.243	2.98	7.46
8	60	2622.133	3.23	5.39
9	80	2688.860	3.44	4.30
10	100	2777.929	3.57	3.57

In addition, it is noticed how the amount of converted CO_2 decreases as its content in the oxidizing gas mixture increases. More precisely, with 6% of CO_2 a conversion of 23.43% is obtained, that is eight times higher than the CO_2 conversion reached for 100% CO_2. The maximum CO production values are represented in Figure 4.14 and it can be noticed that the values tend to reach a plateau, making the gap between them lower as the CO_2 amount in the oxidizing flow increases.

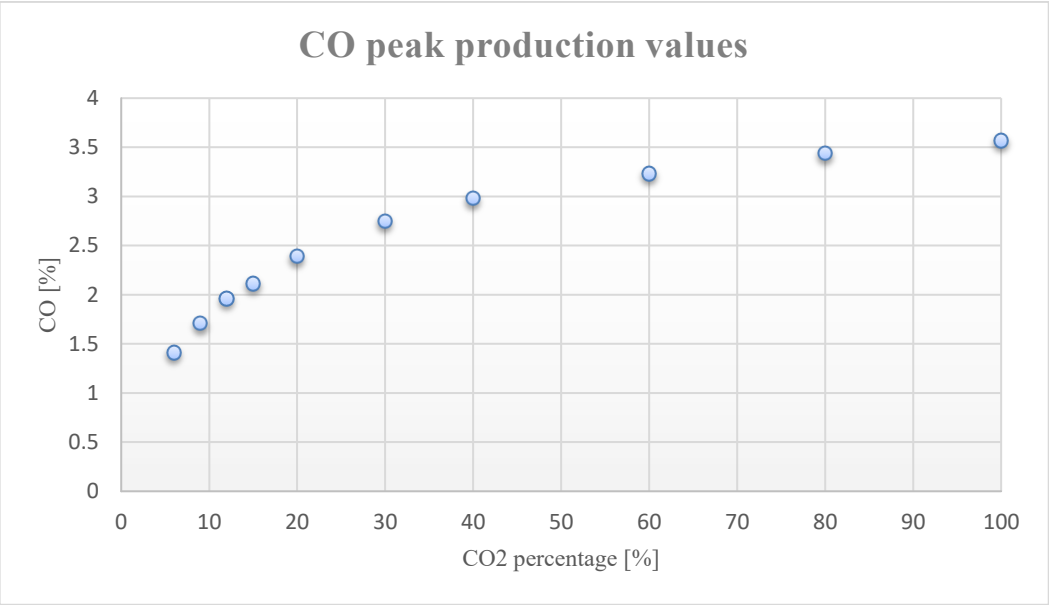

Figure 4.14: *Peak of CO production at various CO_2 content*

Nevertheless, an important observation regards the global CO yield. Ideally, regardless of the CO_2 amount, if the sample-reoxidation was completed, the CO yield should be similar, indicating that all the oxygen vacancies available have been occupied and the maximum CO production has been reached. However, the behavior observed did not follow this pattern, as if the re-oxidation completion was not achieved. This aspect is quite interesting to be understand in order to find the right parameters that allow to achieve a complete re-oxidation and the maximum obtainable CO production, and in order to investigate the eventual presence of side reactions or other phenomena. However, this aspect will be further discussed later.

4.2.5 – TEST(V): Non-isothermal cycles with different CO_2 concentrations (6-100%)

This test is quite similar to that described previously. The main difference is that the CO_2 content influence has been tested for a process performed in non-isothermal conditions. The reduction reactions are carried out at 850°C in 10% H_2/ N_2 for 1 hour, whereas the oxidation steps are performed at 750°C for 30 min with various compositions of the oxidizing gas mixture with CO_2 content ranging between 6% and 100%. The results are reported in Figure 4.15.

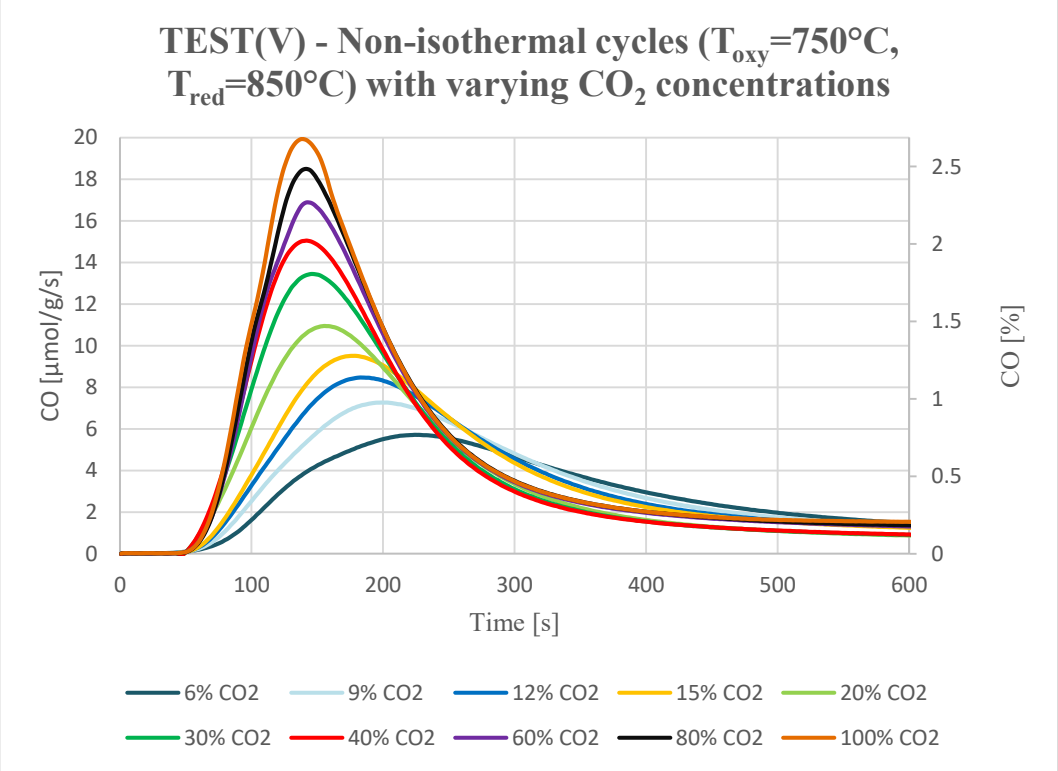

Figure 4.15: *TEST(V) CO production rate for 10 non-isothermal cycles with varying CO_2 content (6-100%).*

The obtained values are higher than those showed in the isothermal process at 750°C and lower than that isothermally performed at 850°C. This means that the reduction temperature, being higher, allows to reach a better sample reduction generating a larger number of oxygen vacancies than consequently lead to a higher

CO production during the re-oxidation steps. Also in this test, as the CO_2 content increases the redox ability of the sample improves, revealing a faster kinetics, a higher maximum *CO* production rate, and higher global yields. According to these results, it is possible to improve the production of an isothermal process performed at 750°C without directly changing the oxidation parameters, but enhancing the reduction step, trying to propose a reducing environment able to generate a large number of vacancies without affecting the material redox ability or stability. However, the presence of a temperature swing between oxidation and rection generally has a partial negative impact on the gas concentration reading due to temperature oscillation of the gases entering the analyzer. Substantially, an isothermal process favors a cleaner reading with respect to a non-isothermal one.

This set of tests conclude the investigation on the oxidation step. In each test and process, before to proceed with the redox reactions a pre-treatment phase in air at 500°C has been always performed in order to guarantee complete re-oxidation of the sample and avoiding any presence of contaminants. In addition, between each reduction and oxidation step a flow of N_2 has always been flushed in the reactor for 10/15 minutes as purge gas. Regarding the oxidation analysis, all the parameters playing an important role in the process, such as temperature or CO_2 concentration, have been widely investigated finding their influence on the CO_2 dissociation and the consequent *CO* formation by using SFNM as oxygen carrier. The sample showed a high stability and repeatability, in fact, in each test, the results have always been coherent and presented a trend close to the expectations. However, the oxidation step is only a portion of the entire process. Several tests suitable for investigating the reduction step have been carried out and are discussed in the next sections.

4.2.6 – TEST(VI): 5 cycles at different reduction temperatures

TEST(VI) is the first one in which the reduction step is analyzed varying its parameters. In this case, the focus is on the reduction temperature variation. A new sample has been employed for the reduction investigation. Using a 200 mg SFNM sample, the reduction temperature plays a fundamental role, since its level has to be

enough to promote the exsolution of the Fe-Ni alloy towards the lattice surface, facilitating the oxygen vacancies formation and increasing the redox ability and the stability of the material. In this specific test, the reduction temperature has been changed from 850°C to 550°C as done for the oxidation temperature. In addition, a last cycle at 850°C has been performed in order to make a comparison with the first cycle at 850°C checking the reference values obtained in terms of *CO* yield. The oxidation step has been maintained at 850°C for all the cycles for 30 minutes, with an oxidizing gas composition of 20% CO_2 in N_2. Before of performing the 5 cycles, an air pre-treatment at 500°C has been carried out, then the temperature was raised up to 850°C while flushing N_2. The cycles are composed as follows:

- Reduction step at 850°C (1, 5), 750°C (2), 650°C (3), 550°C (4) with 10% H_2 in N_2 for 1 hour;
- Purge in N_2 for 10 minutes (1, 5), heating ramp in N_2 up to 850°C (2, 3, 4);
- Oxidation step at 850°C in 20% CO_2/ N_2 for 30 minutes (1-5);
- Cooling in N_2 from 850°C to 750°C (1), 650°C (2), 550°C (3), purge in N_2 for 10 minutes (4), ramp-down in N_2 cooling up to room temperature (5 – end of the process).

The results obtained from the gas analyzer measurements are quite close to what expected. In fact, the *CO* production tends to decrease as the reduction temperature is lowered. A lower reduction temperature may affect the oxygen vacancies formation and the exsolution process, consequently affecting the *CO* production that is favored when the vacancies content in the lattice is higher. The higher the oxygen vacancies number, the higher the oxygen that can be captured from the CO_2 dissociation and adsorbed in the vacancies, the higher the *CO* production. However, since only the reduction temperature has been varied, maintaining constant the oxidation one, the kinetics did not seem to be significantly affected by the T_{red} variation. Conceptually, the observed behavior (Figure 4.16) is quite similar to that obtained in TEST(II), thus at higher temperatures the sample exhibits an enhanced reactivity and an improved redox ability. The first and the last cycles, both performed at 850°C, are not perfectly similar, the first one shows lower *CO* yield and a lower peak. This behavior is actually very common when employing a new

sample, in fact initially, before to obtain a reliable reference a stabilization phase is necessary. In fact, after a first test and an activity period, the sample starts to stabilize its response and in the next tests a more stable and repeatable results will be obtained. Furthermore, this phenomenon is present also in the TEST(II) even if the differences between the first and last cycle are lower than in this case (around 2%).

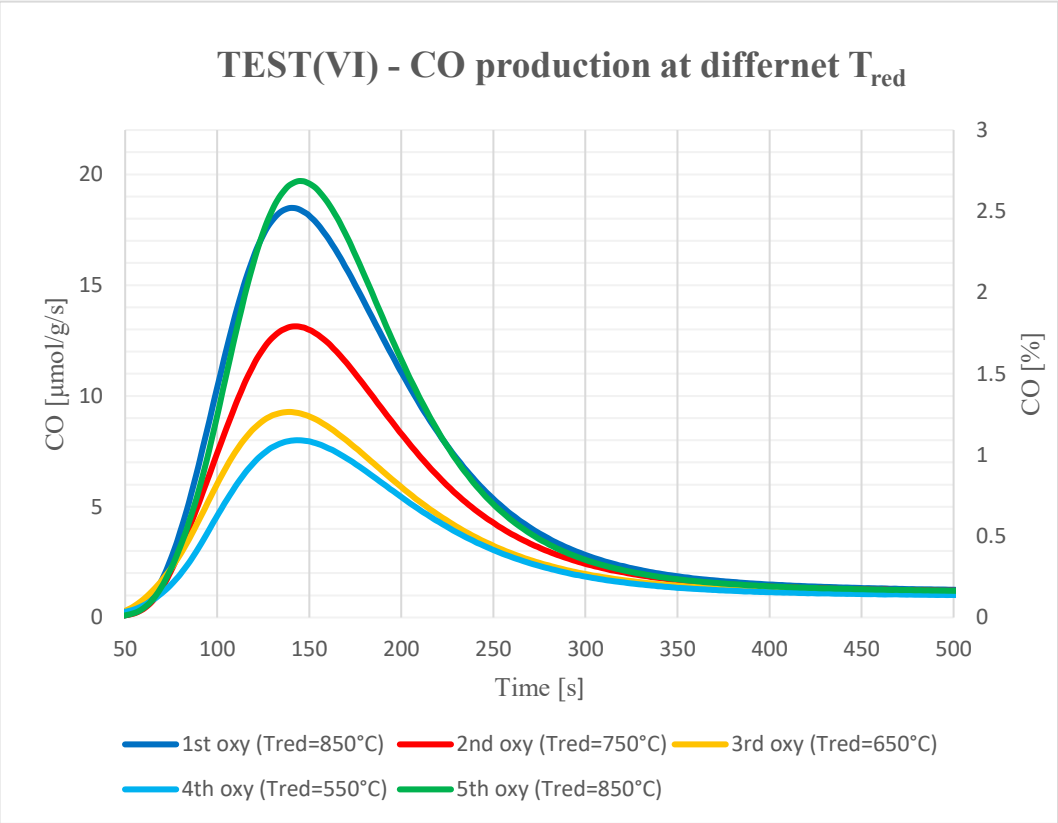

Figure 4.16: *TEST(VI) CO production rate with various reduction temperatures ranging from 850°C to 550°C.*

Considering the cycles obtained at lower reduction temperatures (Table 8) it can be concluded that the lower production yields may be due to a scarcity of oxygen vacancies or to a limited exsolution of Fe and Ni that hinder the oxygen carrier activity. This test confirmed that the best performance is achievable at high temperatures, thanks to the activation of various mechanisms, such as the exsolution, that favor the CO_2 dissociation and the consequent CO production.

Table 8: *Oxidation results for TEST(VI) at various T_{red}: global yield, max CO produced, converted CO_2.*

Cycle	T_{red} *[°C]*	*CO [μmol/g]*	*Max CO [%]*	CO_2 *conversion [%]*
1	850	2304.049	2.48	12.42
2	550	1115.830	1.08	5.38
3	650	1276.639	1.25	6.23
4	750	1724.812	1.77	8.83
5	850	2360..157	2.69	13.43

4.2.7 – TEST(VII): Isothermal cycles with different H_2 concentration (5-100%)

During this test, the *CO* production rate has been measured varying the concentration of H_2 from 5%, that is the minimum amount that can be sent in the reactor and that can be measured by the mass flowmeter, to 100%. The first isothermal process consists of reduction steps performed at 750°C for 1 hour, while the oxidation step is carried out in 20% CO_2/ N_2 for 30 minutes, always at 750°C. The second process is an isothermal test performed at 850°C with the same operating conditions of that carried out at 750°C. As usual, the first step is always represented by the air thermal pre-treatment of the sample, ensuring a full re-oxidation. In Figure 4.17 the *CO* production curves related to the cycles performed for the isothermal process at 750°C are reported. It is noticed that the *CO* yield tends to increase as the H_2 content increases from 5% to 100%. A higher H_2 concentration promotes a favorable reduction of the sample that means a higher amount of released oxygen, and thus a higher amount of oxygen vacancies generated within the structure. Obviously, also the exsolution process is slightly enhanced when the sample reacts in a stronger reducing environment, even if the most important factor for the exsolution occurrence mainly remain the reduction temperature.

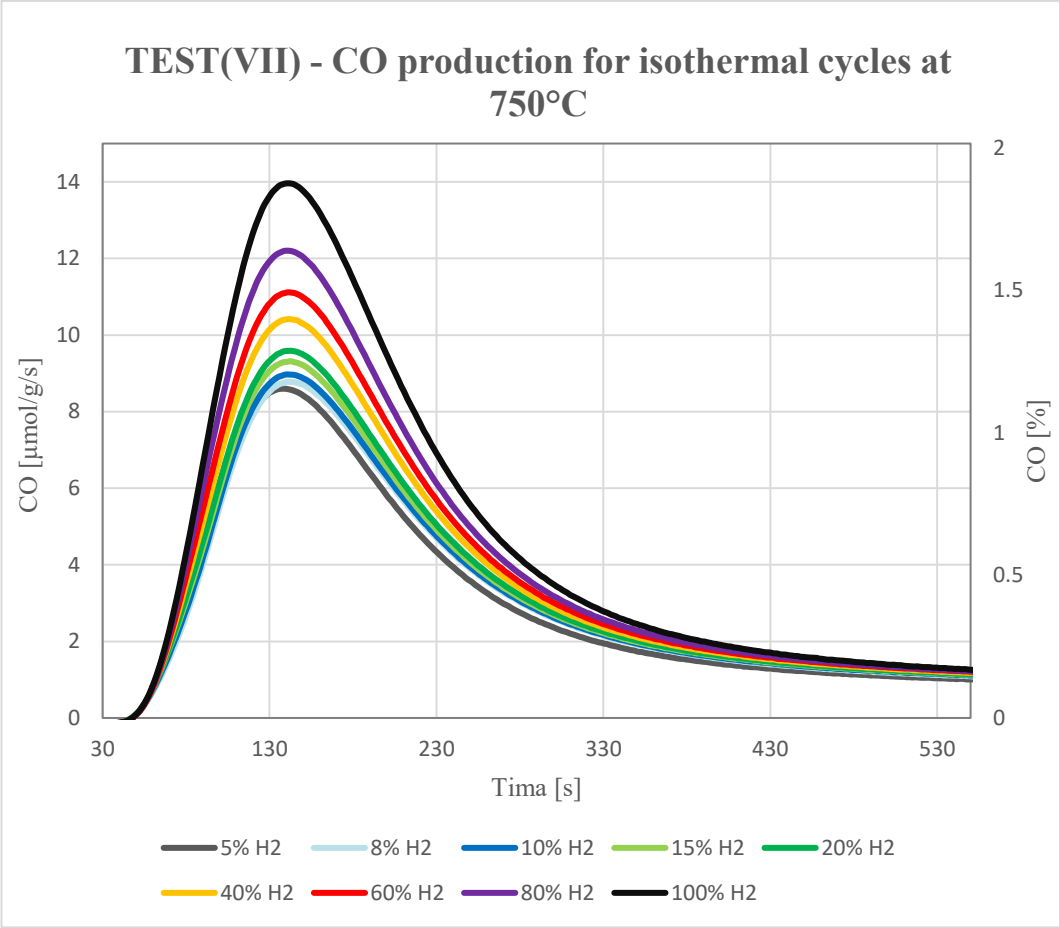

Figure 4.17: *TEST(VII) CO production rate with different H_2 concentrations (5-100%).*

Comparing these results with those obtained at 750°C but varying the CO_2 content it is noticed that in this case the difference between the *CO* peaks tends to increase as the H_2 concentration arises, while during the isothermal TEST(IV) at 750°C the differences were quite constant, exhibiting a slight decrease just for high CO_2 concentrations. The *CO* peak range of variability goes from 8.598 μmol/g/s to 13.961 μmol/g/s, and it is only the half of the range observed in the TEST(IV) when varying the CO_2 content from 6% to 100%. This difference can be explained considering that the used amount of CO_2 directly affects the production of *CO* during the oxidation step and has a higher impact than the H_2 content since the latter only indirectly affects the *CO* production step by leading to a structure containing less oxygen vacancies and then less suitable to produce fuels during a re-oxidation step. Another obvious difference is the influence on the reaction kinetics. The

variation of reducing gas composition by increasing or decreasing the H_2 content shows a trend in which the peak is always reached around the same time instant and the *CO* production rate tends to have a trend very similar to the others, despite the higher values obtained for higher H_2 contents (see Table 9).

Table 9: *Oxidation results for TEST(IV) at 750°C: global yield, max CO produced, converted* CO_2.

Cycle	***H_2 [%]***	***CO [μmol/g]***	***Max CO [%]***	***CO_2 conversion [%]***
1	5	1395.851	1.16	5.78
2	8	1434.225	1.18	5.90
3	10	1458.834	1.21	6.03
4	15	1513.672	1.25	6.26
5	20	1557.499	1.29	6.44
6	40	1688.123	1.40	7.00
7	60	1790.317	1.49	7.47
8	80	1944.104	1.64	8.20
9	100	2190.358	1.88	9.38

The increasing CO_2 conversion, as the H_2 content arises, confirms that the higher H_2 amount permits to generate more oxygen vacancies and to better reduce the sample preparing it to the subsequent re-oxidation, thus a higher *CO* production. Another important aspect that can be found comparing the data in Table 9 with those from the Table 3, is that the maximum *CO* global yield achieved in this test with 100% of H_2, is very close to the value of *CO* production obtainable performing an isothermal cycle at 850°C with 10% of H_2/N_2 as reducing gas and 20% CO_2/N_2 for the oxidation step. Thus, once more, performing a process at 750°C imply neither an effective advantage nor an improvement of the redox performances. In Figure 4.18 have been reported in detail the trends of *CO* production peak ad the percentage of CO_2 converted during the oxidation steps. Unlike the behavior observed when varying the CO_2 content, in this case the trend does not show a tendency to reach a plateau, on the opposite the curve tends to sharply increase as

the H_2 varies from 20% to 100%. Below the 20% of H_2, the variation between the values relative to CO peaks and CO_2 conversion are quite low, on the other hand, the delta between the values tends to rise as the H_2 percentage grows. The plateau does not occur since the variation of H_2 content has not a direct impact on the oxidation, and thus on the CO_2 conversion or on the maximum production of CO achieved. Thus, the H_2 content has an impact on the generation of oxygen vacancies but not on the completion of the sample re-oxidation that, instead, is strongly affected by the CO_2 content injected during the oxidation; an increasing amount of CO_2 implies a higher oxygen uptake and thus a larger CO production, and as the oxidation step approaches completion the CO peaks tend to similar values and then a plateau is reached. In this test, the H_2 flow does not have a strong influence on the oxidation completion, however it has a remarkable role in the path to reach high production rates.

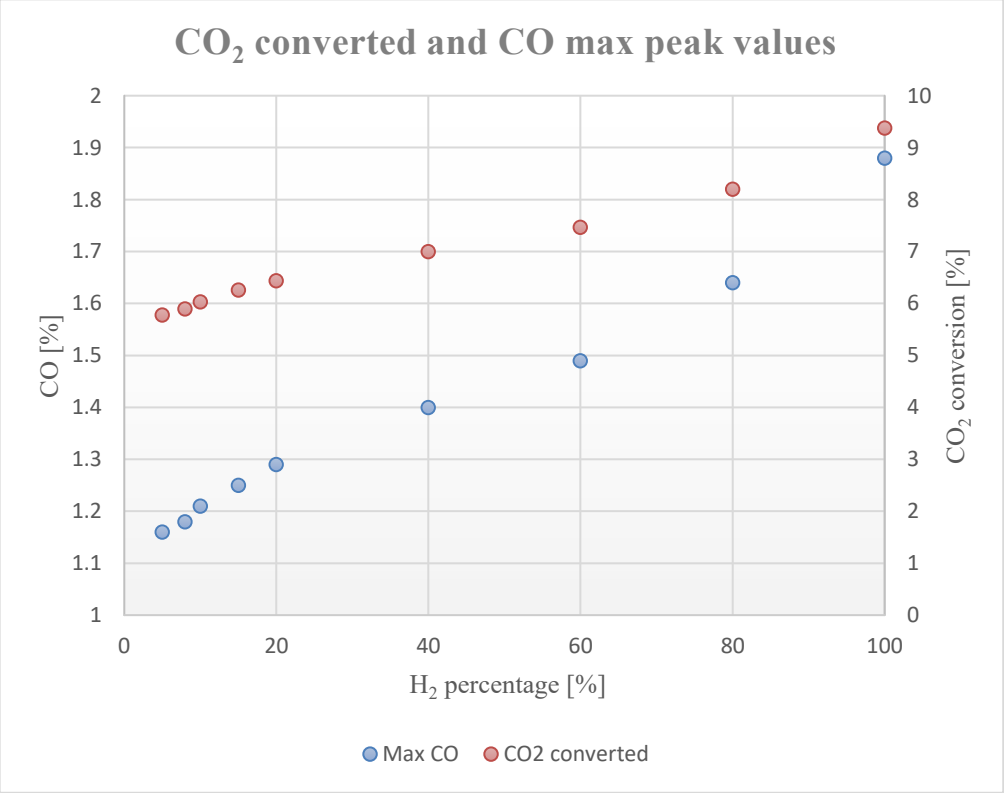

Figure 4.18: *CO_2 conversion and CO production peaks with varying H_2 content (5-100%) at 750°C.*

Anyway, the same kind of test has been performed changing the isothermal temperature and fixing it at 850°C, that is the mainly used value and it represents a

sort of reference for the entire experimental study. However, the oxidation and reduction steps are identical to those already performed at 750°C, the H_2 content has been varied from 5% to 100%, while the oxidation is based on an oxidizing gas mixture with 20% CO_2 in N_2. With a higher operating temperature, an enhancement of the reaction kinetics is expected together with a larger CO production rate and global yield. The results are reported in Figure 4.19.

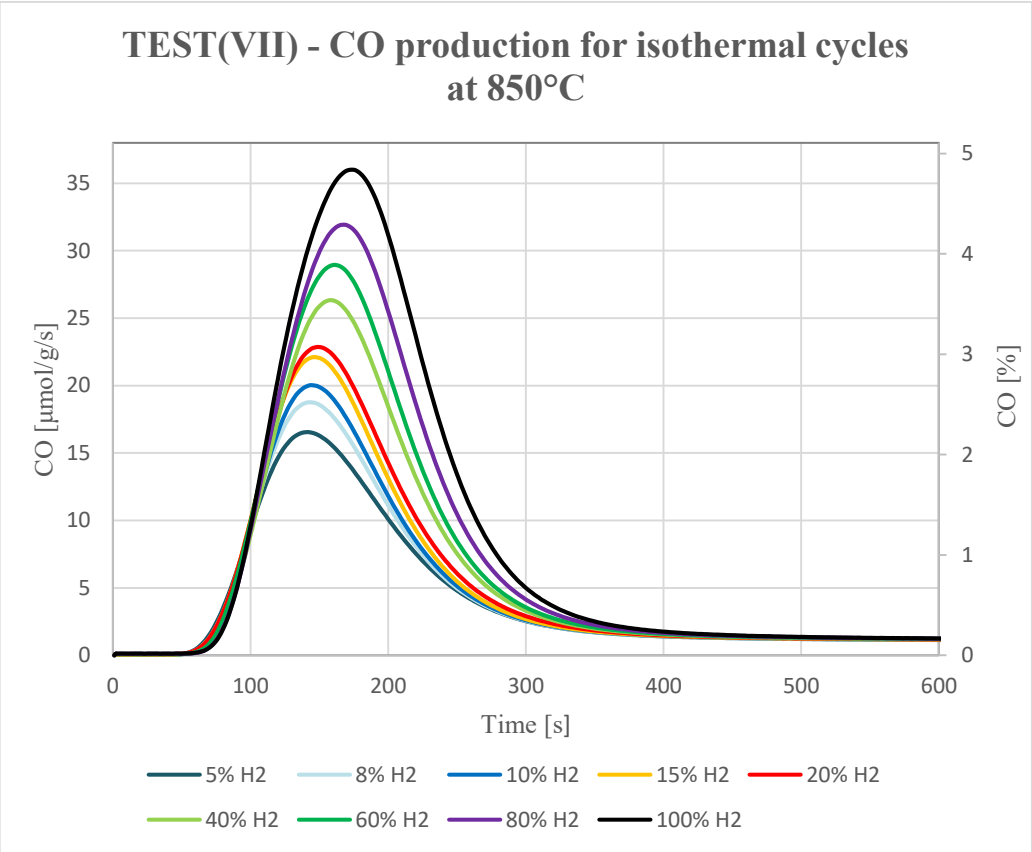

Figure 4.19: *TEST(VII) CO production rate at 850°C (isothermal cycles) with various H_2 content (5-100%).*

It was noticed how the values obtained at 850°C are largely higher than those obtained at 750°C, in fact when using the 5% of H_2 at 850°C the maximum CO production rate reached is higher of that observed when performing an isothermal cycle at 750°C with a reducing gas composed by only hydrogen (100% H_2). In fact, at 750°C with 100% H_2 a maximum CO production rate of around 14 μmol/g/s is reached, that is lower than that obtained at 850°C with 5% of H_2, 16.549 μmol/g/s.

Among all the tests performed, this one presented the highest values in terms of *CO* production (Table 10). In fact, in previous tests the best data had been seen in Figure 4.13 in which an isothermal process at 850°C was performed varying the CO_2 content from 6% to 100%. When the oxidizing gas flow was composed by only CO_2, the observed *CO* production peak was below 27 μmol/g/s, while in this test, keeping the CO_2 content fixed at 20%, but increasing the H_2 amount up to 100%, a *CO* production peak of 36 μmol/g/s was observed. Considering the values involved in the results, the difference of about 10 μmol/g/s is significantly large, and it suggests that at a fixed temperature (that allows exsolution process occurrence) increasing the H_2 content leads to higher *CO* production values than those observed at various oxidizing gas compositions. Furthermore, from the results of this test it is pointed out that the sample generally is not fully reduced. If the sample was completely reduced, independently from the amount of CO_2 contained in the oxidizing gas mixture, the global integral of the *CO* production curve should always be around the same value; in addition, at fixed oxidation parameters, if eventually the sample can be fully reduced using the 10% of H_2, an increase of the H_2 content should not further affect the *CO* production presenting higher values. Resuming, if the increased *CO* production and yield are consequent to an increase of the H_2 concentration in the reducing mixture, then, probably, the reduction cannot be considered completed. The measured data observed in this test overcome the results obtained from all the other tests performed so far. The values reported in Table 10 suggest that improving the reduction phase, strongly reducing the SFNM sample, can lead to fuel production values which are almost two times higher of those obtained in the second best test performed, namely the isothermal test at 850°C with 100% of CO_2. The only improvement or change of the oxidation parameters has an important but also a limited impact on the effective fuel production if compared to the improvements achievable varying also the reduction steps in order to optimize the *CO* production. Thus, an important aspects to be considered is that the oxidation improvement needs to be accompanied by an adequate modification of the reduction parameters too. In Figure 4.20 the *CO* maximum values and the CO_2 conversion have been reported exhibiting an almost linear trend.

Table 10: *Oxidation results for TEST(VII) at 850°C: global yield, max CO produced, converted* CO_2.

Cycle	H_2 *[%]*	*CO [μmol/g]*	*Max CO [%]*	CO_2 *conversion [%]*
1	5	2068.011	2.22	11.12
2	8	2251.821	2.52	12.61
3	10	2364.193	2.69	13.46
4	15	2582.983	2.97	14.86
5	20	2714.205	3.07	15.36
6	40	3122.819	3.54	17.70
7	60	3468.895	3.89	19.45
8	80	3883.687	4.29	21.45
9	100	4524.128	4.84	24.20

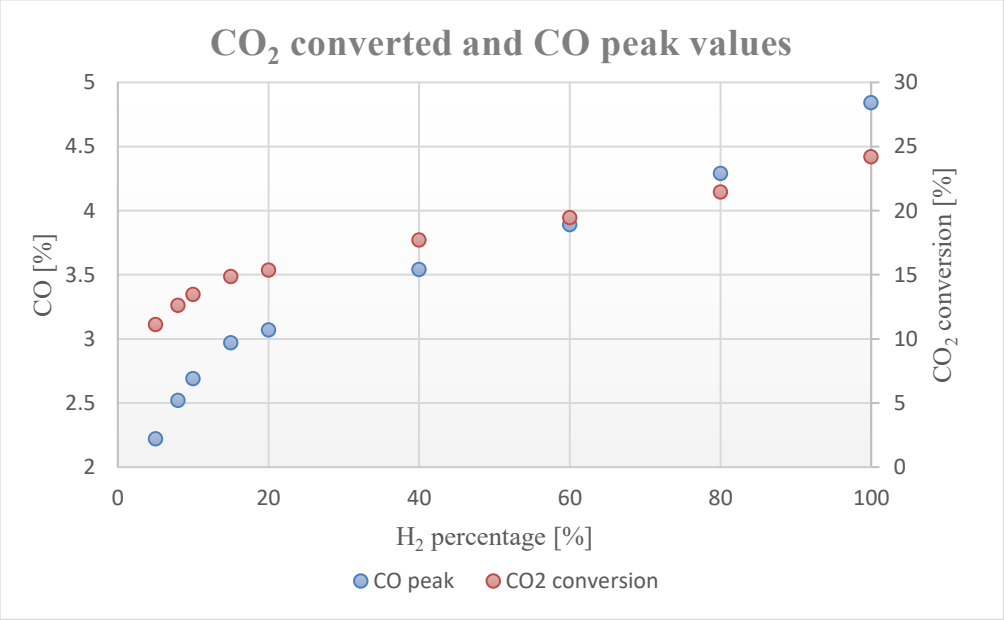

Figure 4.20: *CO_2 conversion and CO production peaks with varying H_2 content (5-100%) at 850°C.*

Also in this case, as already mentioned for the Figure 4.18, the values never reached a plateau but tend to increase monotonically. Unlike the data reported in Figure 4.18, the higher increase is detected for low H_2 concentrations, then the trend

follows a constant growth that represent almost a straight line. The same identical behavior was shown by the CO_2 conversion values, without never approaching an effective plateau. The CO_2 conversion reached a maximum value of 24.2% that is more than two times higher than both the values obtained for the previous isothermal process at 750°C with 100% of H_2 (9.38%), and for the isothermal cycle at 850°C with 20% CO_2 during the oxidation and 10% H_2 during the reduction step (11.94%).

4.2.8 – TEST(VIII): Non-isothermal cycles with different H_2 concentrations (5-100%)

This non-isothermal test has been performed in order to further investigate the effects of H_2 content on the redox ability of the SFNM sample. The reduction steps is carried out at 850°C for 1 hour, while the oxidation ones are performed at 750°C with 20% CO_2/N_2 for 15 minutes. Between the two reactions N_2 has been flushed

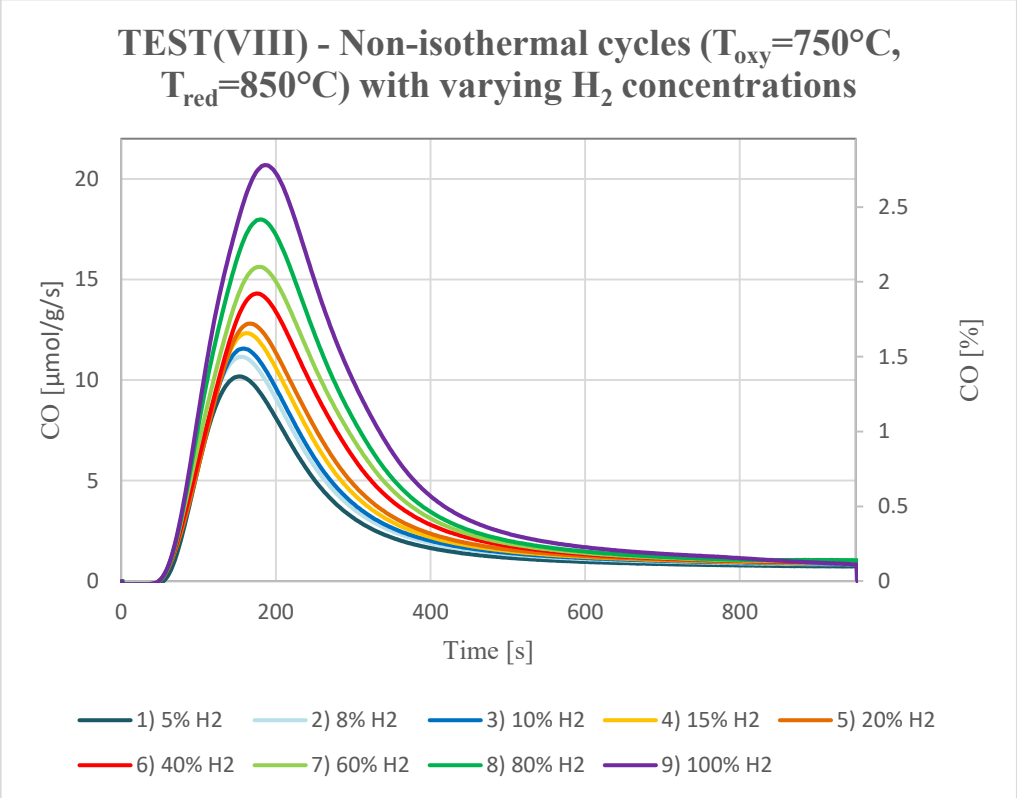

Figure 4.21: *TEST(VIII) CO production rate during non-isothermal process (T_{oxy}=750°C, T_{red}=850°C) with varying H_2 concentrations (5-100%).*

during the heating and cooling ramps needed to switch the operating temperature. Before the first cycle, a usual air pre-treatment was carried out in order to remove any contaminants and to re-oxidize and regenerating the sample avoiding that the previous tests may affects the measurements of the new test. In Figure 4.21 the expected behavior is observed, namely the maximum *CO* produced and its global yield rises as the H_2 content is increased up to 100%. As already observed, a higher hydrogen content improved the reducibility of the sample, however, being the following oxidation step performed at 750°C, the values obtained are significantly lower with respect to those obtained in the previous isothermal test carried out at 850°C. However, despite the lower temperature of the oxidation steps, when using high amount of H_2 the values of *CO* yield are also higher than the values observed when performing isothermal cycle at 850°C during the TEST(IV) as reported in Figure 4.13. In that test, the higher value for the *CO* yield was reported to be 2777.929 μmol/g with a CO_2 conversion of 3.57% (Table 7) when using 100% of CO_2 during the oxidation and 10% H_2 during the reduction, while in this case a maximum global yield of 4034.172 μmol/g and a CO_2 conversion of 13.9% were obtained (see Table 11).

Table 11: *Oxidation results for TEST(VIII): global yield, max CO produced, converted* CO_2.

Cycle	***H_2 [%]***	***CO [μmol/g]***	***Max CO [%]***	***CO_2 conversion [%]***
1	5	1739.105	1.37	6.84
2	8	1916.362	1.50	7.50
3	10	1995.437	1.55	7.77
4	15	2157.362	1.66	8.29
5	20	2286.014	1.72	8.60
6	40	2667.443	1.92	9.61
7	60	2981.933	2.10	10.50
8	80	3424.417	2.42	12.09
9	100	4034.172	2.78	13.90

This comparison reveals a significant difference among the two tests performances, indicating that even with at lower oxidation temperature and a lower CO_2 percentage in the oxidizing gas flow, it is possible to remarkably increase the fuel production by improving the reduction step, enhancing the sample reduction and the oxygen vacancies generation. Furthermore, another parameter that can be extremely improved is the CO_2 conversion, in fact it was observed that this parameter tends to increase as the CO_2 content in the oxidizing gas mixture decreases. The highest CO_2 conversion, regarding the oxidation investigation (TEST I-V), was observed during the isothermal TEST(IV) at 850°C with 6% of CO_2, reaching a value around 23% (Table 7). However, in the previous test, it was reached a value of 24.2% when using 20% of CO_2 in the oxidizing gas, and 100% of H_2 during the reduction. Also in this test, it was confirmed that high CO_2 conversion values can be obtained by improving the sample reduction, as alternative to the use of low CO_2 content that leads to high conversion values but, on the other hand, negatively affecting the amount of *CO* produced. This test is the last one conducted with the aim of investigating the influence of the hydrogen content on the sample performances. An important aspect to underlain is that, unlike the tests where the CO_2 amount was varied, varying the composition of the reducing gas by increasing the amount of H_2 implies *CO* production rate curves that presents wider peaks. In these cases a wider peak was always correlated to a higher *CO* yield, and this behavior may be explained by the greater availability of oxygen vacancies, generated during the reduction step, which in turn allow to improve the fuel production. During the oxidation experimental investigation was observed how the CO_2 content and the oxidation temperature, when changed, affected the reaction kinetics, and thus affected the *CO* production. Nevertheless, varying the H_2 content leads to different trends where the curves start to rise at the same time, at almost an identical rate, continuing to grow until the peak is reached, and both the peak value and the time spent to reach it strongly seem to depend on the amount of oxygen vacancies in the sample lattice. On the opposite, it can be observed that during the oxidation investigations, when varying the CO_2 concentration value in the gas mixture, as the CO_2 increases the starting growing rate of the *CO* production is faster, furthermore the peaks tended to shift to the left, this means that the peak

values were reached in less time and that the reaction kinetic was faster. So, summing up, can be concluded that the oxidant gas composition mainly affects the reaction kinetic, and thus the speed at which the *CO* is produced by CO_2 dissociation, whereas the reducing gas composition significantly affects the curves width, suggesting that it strongly depends on the oxygen vacancies potentially available in the perovskite lattice.

4.2.9 – TEST(IX): Isothermal cycles at 850°C with various reduction reaction time

This type of test is considered important in order to understand how the reduction duration may affect the sample structure and its redox properties. In the previous tests the reduction reaction was always carried out for 1 hour, regardless of both the H_2 content and the fixed operating temperature. However, the reaction time represents a key parameter as much as the others investigated so far. Each cycle consists of a reduction step performed at 850°C with 10% of H_2, since it is the reference value adopted also in the other tests. The reduction time (t_{red}) has been changed starting from 15 minutes up to 2 hours. The oxidation reaction is carried out at 850°C for 30 minutes with 20% of CO_2; also in this case the reference value has been used in order to better understand the effects only due to the reduction time variation. The *CO* production rate has been studied performing 6 redox cycles by imposing always the same operating conditions except for the reduction step duration that has been fixed at 15, 30, 40, 60, 90, and 120 minutes, respectively. The results are shown in Figure 4.22 which reveals that the general trend correspond to an increasing *CO* production as the reduction time became larger. This behavior may be explained considering that, even if the H_2 concentration in the reducing gas is only equal to 10%, if such a gas mixture is flushed for 15 minutes it has a certain reducing effectiveness on the sample that would be lower with respect to that of the same mixture that is constantly flushed for 1 hour. During a reduction or oxidation step, generally, the reaction begins on the sample surface, especially thanks to the SFNM properties correlated also to the exsolution process. Anyway, when the time available for the reaction is greater, the gas mixture has the potential to better react

with the entire structure, diffusing into the lattice that consequently releases or uptakes oxygen ions, depending on the type of reaction. For this reason, a probable explanation for the measured data (Table 12) is linked to the possibility of improving the reaction extension beyond the reaction sites located on the sample surface.

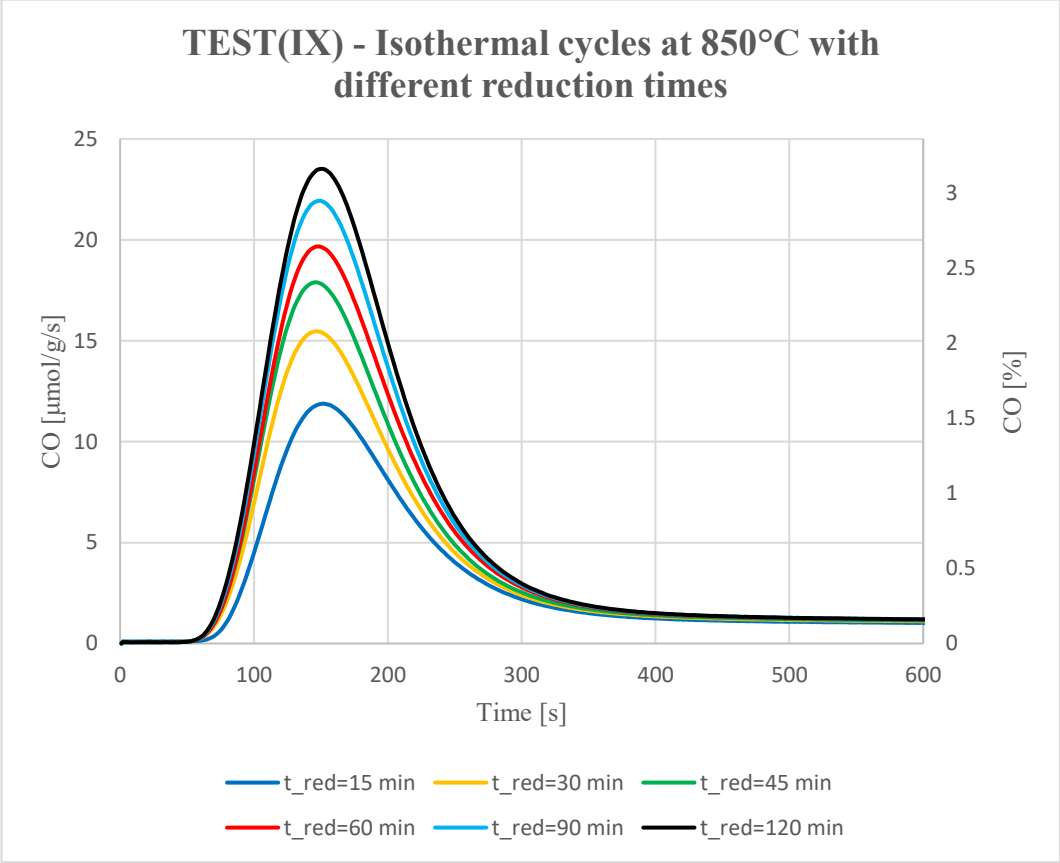

Figure 4.22: *TEST(IX) CO production rate during an isothermal process at 850°C with different reduction times (15-120 minutes).*

The worst results are obtained for low reduction time, in fact when it is fixed at 15 minutes, the *CO* yield reached 1453.697 μmol/g that is equal to the 60% of the reference value observed when imposing a reduction duration of 60 minutes. The same thing is valid when comparing the *CO* peak and the CO_2 conversion values. On the other hand, the maximum time selected for the reduction reaction is 2 hours. In this case the *CO* global yield increased by 20% with respect to the reference value, with a consequent improvement of the fuel production. Resuming, from this

test has been understand how much the reduction time may affects the *CO* production and that the longer the reduction is performed, the more the sample is able to produce higher amount of *CO* exhibiting a larger amount of oxygen exchanged. Likewise, in the next section the oxidation time has been investigated in order to assess its influence on the sample reactivity and redox ability.

Table 12: *Oxidation results for TEST(IX): global yield, max CO produced, converted* CO_2.

Cycle	t_{red} ***[min]***	***CO [μmol/g]***	***Max CO [%]***	CO_2 ***conversion [%]***
1	15	1453.697	1.60	7.98
2	30	1864.056	2.08	10.39
3	45	2128.861	2.41	12.03
4	60	2356.220	2.64	13.22
5	90	2607.049	2.95	14.74
6	120	2792.556	3.16	15.80

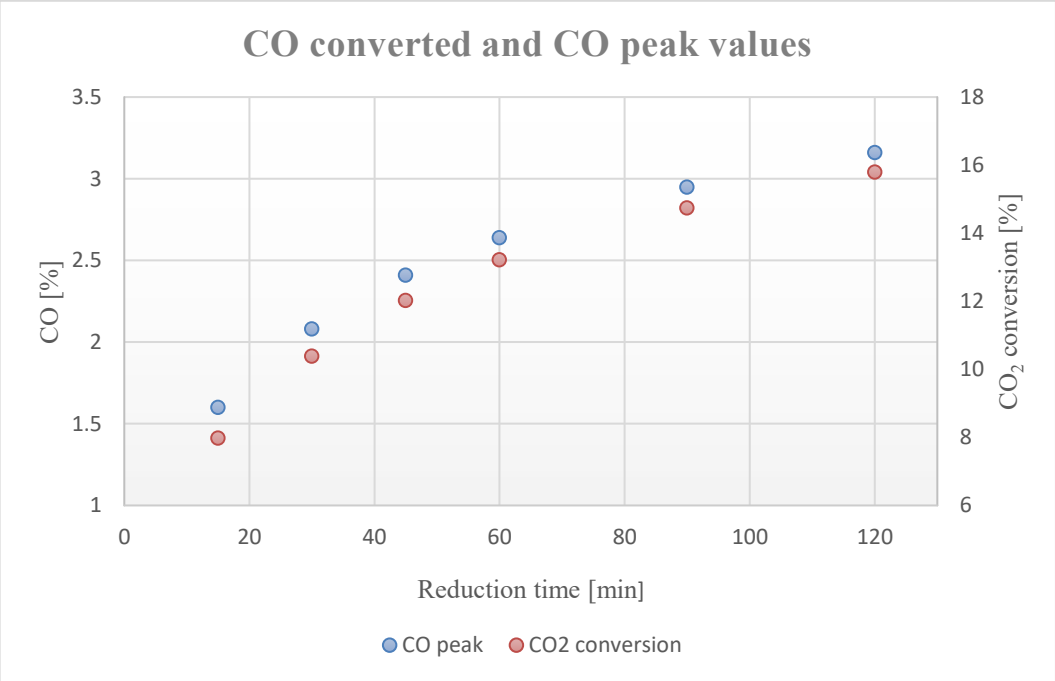

Figure 4.23: *CO_2 conversion and CO production peaks with varying reduction times (15-120 minutes).*

Finally, in Figure 4.23, the *CO* peak values and the CO_2 conversion have been reported. It can be noticed that has the reduction time increases the variation among the values tends to slightly decrease, however the difference between the two last values is not negligible and it may suggest that the reduction is not complete yet.

4.2.10 – TEST(X): Isothermal cycle at 850°C with oxidation reaction of 7 hours

In all the tests described so far in this chapter, the oxidation reaction has always been performed for a maximum of 30 minutes. As already assessed for the reduction step, the reaction time may be fundamental also in the case of the oxidation steps allowing to better perform the re-oxidation of the sample reaching the deeper oxygen ions in the sample lattice. An important aspect, that pushes further to investigate the reaction time effects, is *CO* production values detected in proximity of the tails. In fact, it was noticed that once the production peak is exhausted the measured data tend to settle on an almost constant value generating a flat tail that exhibit a very low degrowth rate. This value was thought to correspond to a reading inaccuracy of the gas analyzer, or maybe the instrument continued to see a little amount of *CO* which could be minimally confused with CO_2 contained in the gas flow sent to the microreactor. However, this tail values were compared with those obtained during a white test where several cycles have been performed changing the CO_2 content from 6% to 100% with a reaction time of 30 minutes. Anyway, the maximum *CO* production value obtained during this test was below 1800 ppm when using a 100% CO_2 flow, instead the tail values were lower than 700 ppm. In the previous test, when the microreactor was charges, the tail values settle around 1100 ppm, with a minimum *CO* peak of 4500 ppm, when using 6% of CO_2 at 850°C. Obviously, the focus is on the curves tail value, ideally the values read during the white test can be considered the value correspondent to the zero *CO* production rate, thus if the values grow when employing the SFNM sample it may means that there is a minimum rate of *CO* production that persists for long time after the peak occurrence. In view of the facts, it is reasonable to suppose that the oxidation

conditions used so far may not have been sufficient to fully re-oxidize the sample. The aim of this test is to understand if this behavior is due to a non-ended oxidation of the material or to a wrong instrument reading. In order to assess this aspect, it was chosen to perform a cycle at 850°C with a 7 hour-long oxidation. The best operating conditions were used in order to favor the reduction reaction, in fact this step was carried out at 850°C for 2 hours with 100% of H_2, while the oxidation step was performed at 850°C with the reference concentration of 20% CO_2 gas flow. The results of this test are shown in Figure 4.24, the amount of CO produced has been calculated integrating the curve using both the method illustrated in Figure 4.8 (a) considering only the peak, and by calculating the entire area below the curve without cutting the tail. The combination of high H_2 concentration and high reduction time (2 hours) lead to the highest peak of CO production rate among all the tests performed, it is equal to 46.129 μmol/g/s or 6.2%. The same goes for the CO_2 conversion that reaches 31% which represents the highest value achieved in the tests proposed in this chapter.

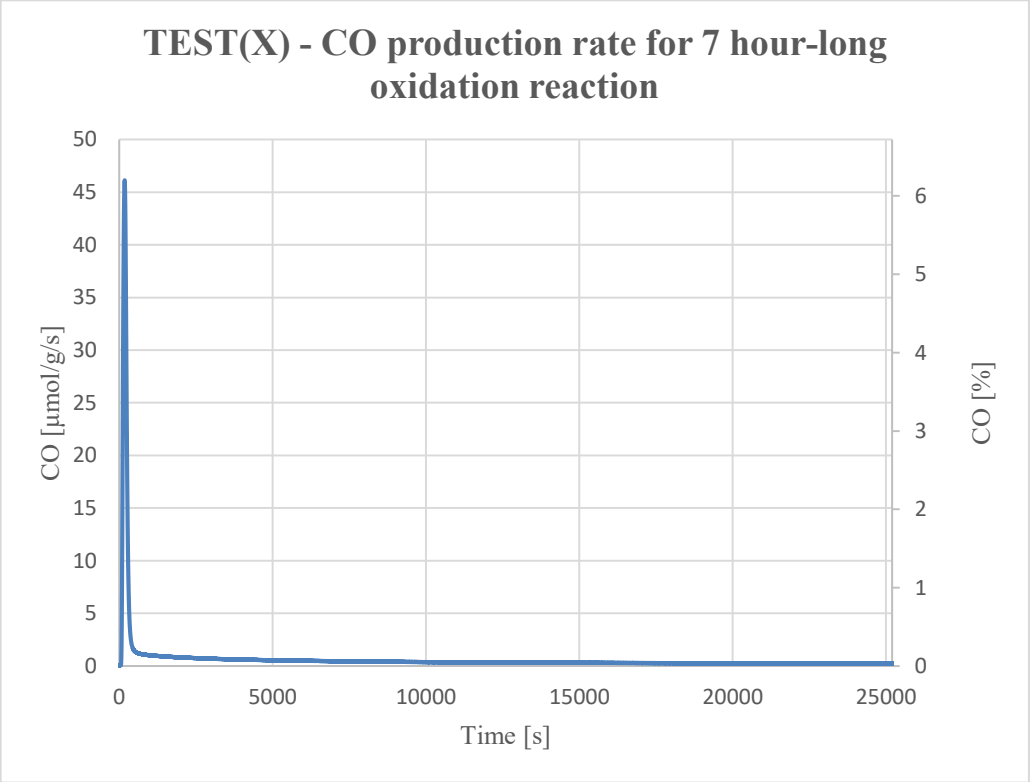

Figure 4.24: *TEST(X) CO production rate during an isothermal process at 850°C with 7 hour-long.*

The optimum results observed here are obviously due to the combination of the best reduction operating conditions, but also to the elongation of the oxidation duration. The modification of both oxidation and reduction reactions contributes to this achievement. However, in order to assess the nature of the curve tail a white test has been performed, maintaining the same identical conditions, but removing the sample from the microreactor. In this way no reactions will occur in the reactor and no *CO* should be detected by the analyzer. However, it was already discussed that a minimum portion of *CO* could be detected anyway during a white test, and in that case, we can consider that value as corresponding to the "zero" *CO* production. The comparison of the two curves, with charged and discharged microreactor are reported below in Figure 2.25.

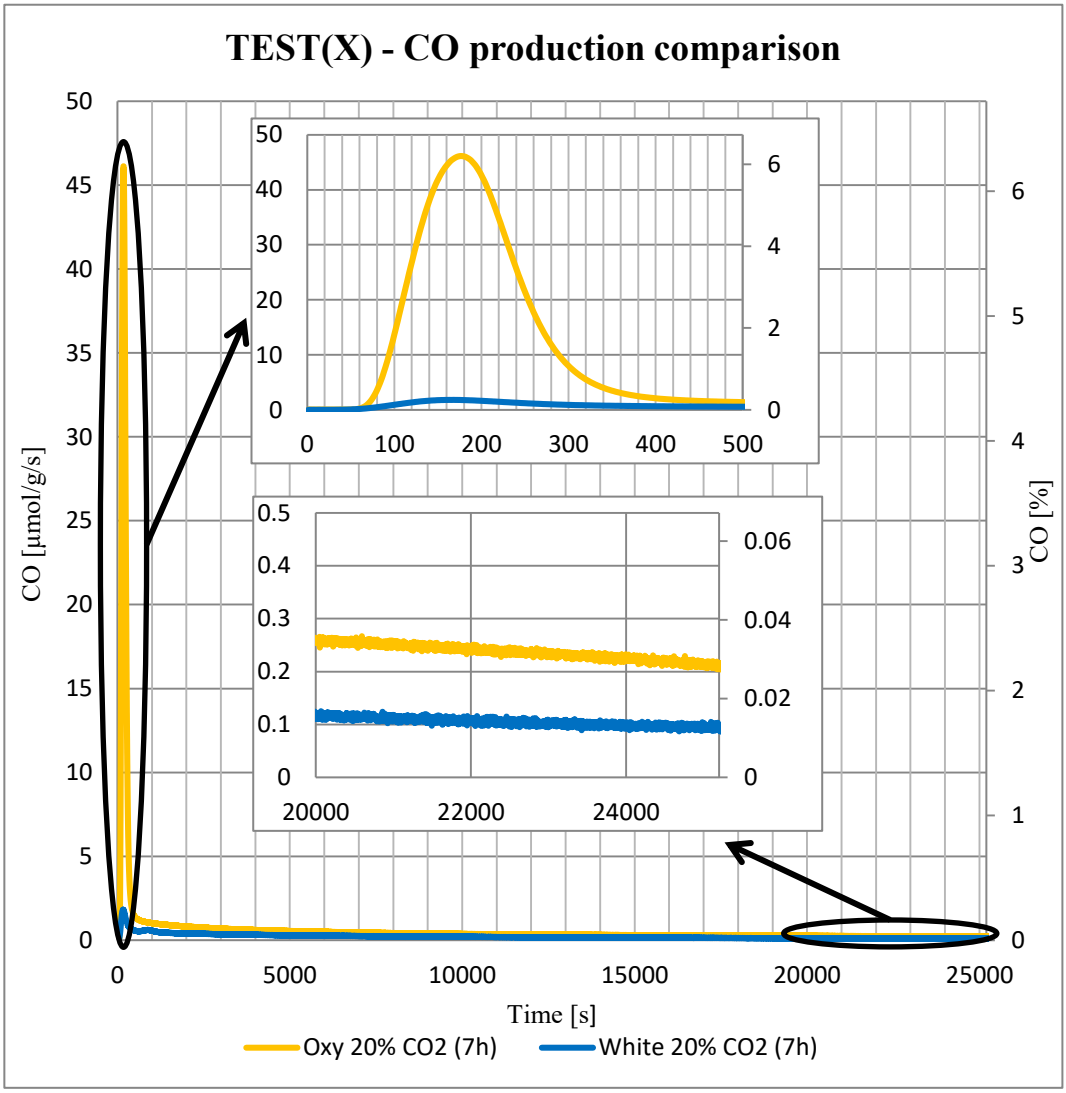

Figure 4.25: *TEST(X) CO production rate for 7 hour-long oxidation compared to a white test.*

In this figure the two tails exhibit an almost constant difference (around 0.1/0.2 μmol/g/s), its presence may be explained by a non-ended reaction, however it could be possible to imagine that the reaction goes on because an equilibrium condition is reached and it involves, even if low, continuous production of *CO*. The global yield has been recalculated by subtracting the white test values from the test performed with the charged microreactor. Several options have been considered:

- Area 1: *CO* peak area cutting the tail as represented in Figure 4.8 (a);
- Area 2: Total *CO* yield considering the entire curve;
- Area 3: Total *CO* yield by subtracting the values corresponding to the white test.

Table 13: *Global CO yield for TEST(X) using different methods.*

Area 1 [μmol/g]	**Area 2 [μmol/g]**	**Area 3 [μmol/g]**
6343.693	16777.850	11282.056

The two magnifications in Figure 4.25 are a more detailed representation of the comparison between the two curves. The one at the top corresponds to the first part of the reaction and it includes the production rate peak occurring in the first few seconds of the reaction. The other magnification is representative of the final portion of the reaction and shows the difference between the two tails, revealing that the difference is present, but it is quite small. Following all the performed tests, based only on the reactivity investigation of the sample, it is not possible to identify the actual cause of the discrepancy of the production tail values with the white test ones. As already said, it could be due to gas analyzer inaccuracy, it may represent an actual fuel production, the equilibrium condition may be reached leading to a low but almost constant *CO* production, it may be related to other mechanisms involving structural changes or new phases formation such as carbonates ($SrCO_3$) and insulant phases ($SrMoO_4$). However, at the same time, it is quite difficult to understand whether the oxidation reaction is complete or not and for what reasons.

Chapter 5

5 – Discussion and considerations

The results obtained through the microreactor tests revealed the SFNM04 ability to be subjected to redox cycles and it exhibited a very good stability and a great ability to perform redox reactions in a two-step thermochemical process. SFNM04 properties and characteristics have been evaluated and analyzed by varying the operating conditions, namely the reaction temperature, the gas mixture composition, and the reaction time of both oxidation and reduction steps. The analysis has been subdivided in two parts, an investigation exclusively focused on the oxidation reaction parameters, and a second one based on the reduction conditions variation. One of the first experimental tests revealed the influence of the oxidation temperature. The reference temperature used during the tests was 850°C, but as soon as it was decreased the oxidation step turned out to be slower and the *CO* production was significantly lower. The lower temperature values investigated was 550°C, in this case the results exhibited a slow reaction kinetics with a *CO* production rate curve that reach a maximum value much lower than the reference one, resulting in a maximum concentration of *CO* in the gas exiting the reactor of 0.49% against the reference value of 2.52%. In can be concluded that the oxidation temperature has a relevant effect on the reaction kinetics and thus on the *CO* global yield. Subsequent tests focused on the influence of the oxidant gas compositions. The CO_2 concentration was changed several times within the range

6%-100%. Generally, regardless of the temperature involved in the process, as the CO_2 increased a higher CO yield was observed and also the CO production peak reached higher values. Firstly, the amount of CO_2 in the gas mixture seemed to affect the kinetics, in fact considering an isothermal process at 850°C, a mixture containing 100% of CO_2 needed around 120 seconds to reach the peak, that is almost half the time necessary in the test performed using an oxidizing mixture with 6% of CO_2 that needed 200 seconds to reach its maximum CO production value. Furthermore, as the CO_2 concentration decreased it resulted in wider curves. However, if the sample re-oxidation had been complete the global yield should not have changed as the CO_2 concentration increased, anyway the opposite behavior is observed in the test results suggesting that probably the sample never reached a complete re-oxidation. Nevertheless, from the data measured by the gas analyzer the graphs queue exhibited CO production values higher with respect to the values observed when performing a white test, thus without a sample placed in the microreactor. This behavior led to justify it as consequence of a constant CO production due to the achievement of the reaction equilibrium. However, this remain a hypothesis difficult to verify being able of relying only on the analyzer measured data. The same goes for the reduction step, in order to understand when the sample is completely reduced it could be useful to directly measure the amount of oxygen ions released from the perovskite lattice. However, the oxygen ions released are only indirectly estimated by considering the amount of CO produced during the oxidation step. In this regard, several tests have been carried out where the H_2 concentration in the reducing gas mixture was changed from 5% to 100%. It was noticed that when increasing the H_2 concentration value, the subsequent oxidation step resulted in higher CO global yields. This behavior can be easily explained considering that a higher amount of H_2 permits a greater release of oxygen from the structure and thus the generation of a higher amount of oxygen vacancies. Obviously, it represented a huge advantage that favored the CO production during the following oxidation step, however, the constant increase of the CO global yield when increasing the H_2 content suggested that probably also the sample reduction cannot be considered complete. If the sample was fully reduced, while increasing the H_2 content, the total CO production should be the

same, however the opposite behavior can be observed in Figure 4.19. Other tests revealed also the importance of the reduction time, the longer the reduction the higher the consequent *CO* production, probably due to the same phenomena that occurs when increasing the H_2 concentration, that is, the increase in oxygen vacancies. Generally, it is observed that when varying the oxidation parameters they affected mainly the reaction kinetics and thus it had a direct impact on the *CO* production, on the other hand, when varying the reduction conditions it resulted in an indirect way to affect the *CO* production during the oxidation step by increasing the availability of oxygen vacancies in the lattice and exhibiting as result higher and wider curves. The effects of CO_2 and H_2 concentration variation was evaluated during the TEST(IV) and TEST(VII), respectively, and it was noticed the higher impact of the reducing gas composition with respect to the oxidizing one. In fact, an oxidation performed with 100% of CO_2, when using 10% of H_2 during the reduction step, led to a maximum *CO* yield of 2777.929 μmol/g, on the other hand, when using 100% of H_2 for the reduction, and 20% of CO_2 during the oxidation reaction, a *CO* global yield of 4524.128 was achieved. However, it was also noticed a substantial difference in terms of CO_2 conversion which tended to increase significantly when the reduction reaction time or the H_2 concentration were increased, respectively. The higher CO_2 conversion value, 24.2%, was observed during TEST(VII) when performing an isothermal process at 850°C with the reducing gas mixture containing 100% of H_2. Anyway, a similar value (23.43%) was achieved during the oxidation reaction investigation, in particular during TEST(IV) at 850°C when using a concentration of CO_2 equal to 6% in the oxidizing gas mixture. However, it should be emphasized that in the TEST(IV) with 6% of CO_2, despite the achievement of a good level of CO_2 conversion, the values corresponding to the *CO* production were extremely disappointing and widely lower than the reference values. On the other hand, during TEST(VII) at 850°C there was a combination of high CO_2 conversion percentage and high *CO* yields. On that basis, the experimental results have shown how the reduction conditions had a huge influence on the process and how beneficial its effects could be. Probably, a plausible explanation it can be found by considering the exsolution phenomenon (Figure 5.1).

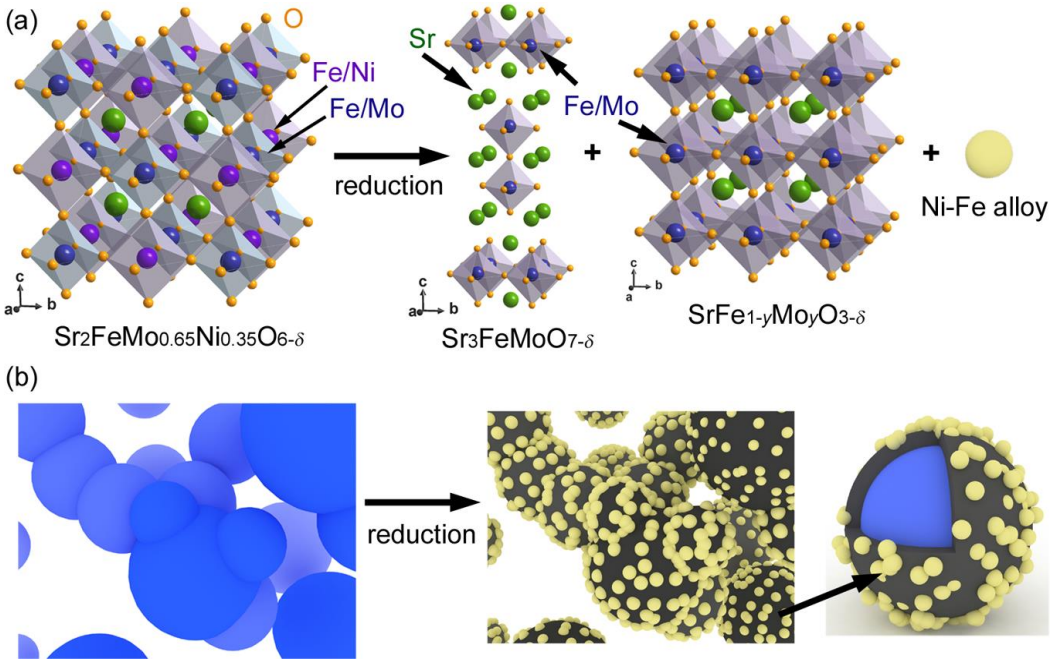

Figure 5.1: *(a) variation of the perovskite structure, (b) exsolution phenomena occurred under reducing conditions [133].*

The exsolution, occurring under reducing atmosphere, implies the reduction of Fe^{2+} and Ni^{3+} which move towards the surface where an alloy Fe-Ni is generated. The presence of this metal alloy may represent the reasons why enhancing the reduction conditions lead to beneficial effects. First of all, the exsolution of these ions allows the formation of several vacancies, secondly the metal alloy play the role of catalyst of the oxidation reaction by favoring the CO_2 dissociation. This twofold effect related to the exsolution phenomenon further underlines the importance of performing a reduction step by employing the best possible operating conditions. Du et al. [133] confirmed the exsolution occurrence by studying $Sr_2FeMo_{0.65}Ni_{0.35}O_{6-\delta}$ that had an *Ni* content slightly lower to that used in this work (x=0.4). An XRD analysis was performed on the sample after a reduction step carried out at 850°C in H_2 (Figure 5.2). The results have shown a transition from the perovskite structure to a structure containing also the overcited RP phase, in addition the presence of the $FeNi_3$ alloy was detected on the lattice surface confirming the results obtained from the University of Udine. However, the exsolution process needed a temperature at least higher of 450°C in order to occur (Figure 4.3).

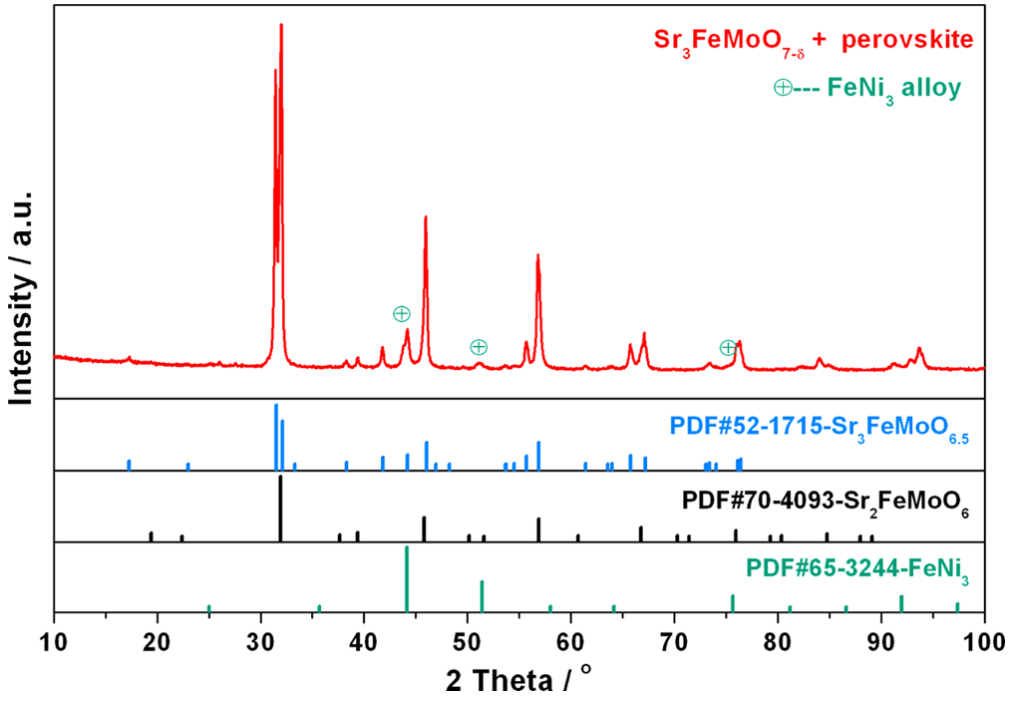

Figure 5.2: *XRD analysis of* $Sr_2FeMo_{0.65}Ni_{0.35}O_{6-\delta}$ *after a reduction step in* H_2 *at 850°C [133].*

An additional issue that was found in literature when performing thermochemical cycles aimed at CO_2 splitting is the possible formation of carbonates. Microreactor tests did not allow to directly recognize the presence of carbonates such as, in this case, $SrCO_3$ but its presence could be more easily detected through thermogravimetric analysis. In that case, a constant increasing mass of the sample, during an oxidation step, may be a signal of the carbonated formation. However, in this work only microreactor tests have been performed, thus the only direct results

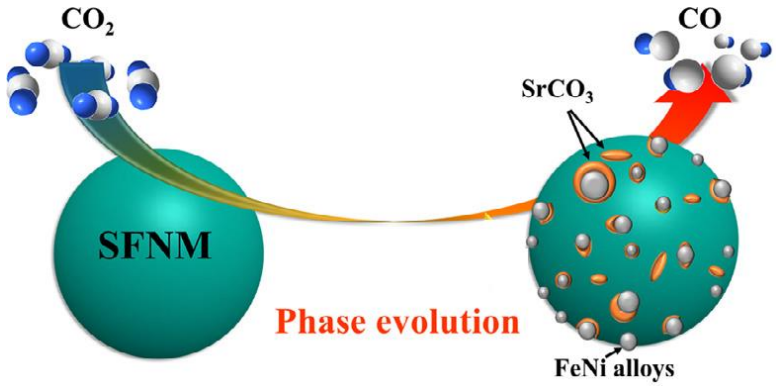

Figure 5.3: *Phase transition of SFNM and carbonates formation [136].*

obtained regarded the gas composition analysis. The carbonates formation, in this case, is highly favored by the presence of *Ni* that act as catalyst and facilitates the formation of $SrCO_3$. Its presence in the structure negatively affects the re-oxidation of the sample by hindering the CO_2 splitting and the oxygen diffusion on the surface, thus inhibiting the consequent *CO* production. Nevertheless, despite its negative influence, the $SrCO_3$ content in the structure was noticed to significantly decrease, with its consequent decomposition, performing a thermal treatment at around 500-550°C. $SrMoO_4$ represent an insulant phase that affects negatively the SFNM redox cycles processes and, also in this case, its formation is favored by the *Ni* presence in the structure. However, it was found that increasing the *Ni* content in the sample and performing a calcination at around 900°C led to $SrMoO_4$ decomposition. Resuming, the *Ni* doping in the SFM structure favors the stability, reactivity, and cyclability of the sample, but at the same time provokes the presence of detrimental phases such as $SrCO_3$ and $SrMoO_4$.

Chapter 6

6 – Conclusion

The main theme of this work concerns the experimental analysis of SFNM04 perovskite material for CO_2 splitting through chemical looping processes. $Sr_2FeMo_{0.6}Ni_{0.4}O_{6-\delta}$ is a novel material object of study within a project born from the international collaboration between University of Udine, Massachusetts Institute of Technology (MIT), and Politecnico of Torino. This work encompasses one of the first experimental evaluation of SFNM in terms of redox cycles through microreactor tests. The tests performed so far outlined a preliminary assessment in terms of redox ability and reactivity of SFNM when employed in thermochemical cycles with the aim of dissociating CO_2 in order to produce carbon monoxide. SFNM04 has a double perovskite structure that shows a phase transition when subjected to a reducing environment. The phase transition leads to a new Ruddlesden-Popper phase ($Sr_3FeMoO_{6.5}$) that partially substitutes the pure perovskite structure. A peculiar feature of this material is the exsolution occurrence in reducing atmosphere. This phenomenon consists in the reduction of the Ni^{3+} and Fe^{2+} and their consequent exsolution from the lattice towards the surface generating a nanoparticles metal alloy Fe-Ni. The utility of this alloy located on the lattice surface involves catalyzing the oxidation reaction and the generation of oxygen vacancies inside the material structure. Several tests have been performed alternately varying the operating conditions of oxidation and reduction reactions, respectively. In each test one of the main parameters among reaction temperature, reaction time and gas mixture composition has been changed within a certain range. The temperature has been varied between 550°C and 850°C (reference temperature)

for both oxidation and reduction steps, while the H_2 and CO_2 concentrations have been changed in the range 5%-100% for reducing and oxidizing gas mixtures, respectively. The first tests in the microreactor setup have shown a good reproducibility of the cycles underlying a material stability for repeated redox cycles. Despite the positive aspects regarding the *CO* production rates and the *CO* global yields achieved in the various tests, consistently with the fixed operating conditions, it was extensively questioned whether the reactions were complete or not, thus whether the sample was considerable as fully oxidized/reduced or not. In order to investigate this aspect various tests have been carried out trying to expand the reaction time and to increase the concentration of H_2 or CO_2 based on the type of reaction being considering in that specific test. Moreover, white tests were performed and compared to the results obtained employing the perovskite sample. The comparison was mainly focused on the data collected correspondingly to the final portion of the oxidation reaction, namely the curves tail, and a slight difference was noticed reveling that when the sample is used the results are higher with respect to the "zero value" correspondent to the white test values. Although small, that difference could actually represent a *CO* production that continues even after 7 hours of reaction. This behavior could be ideally justified by imagining a higher difficulty to reach innermost vacancies in the structure and therefore the reaction takes more time, alternatively it could be due to the achievement of the reaction equilibrium. Nevertheless, it could be the influence of other factors and mechanisms that are not visible and measurable by the gas analyzer, thus they are hard to identify. Carbonates and molybdates formation is the main option among the various negative factors that could affect the reactivity of the SFNM04 sample. In fact, it was noticed that when using a material such as SFNM04, there is a high probability to find carbonates ($SrCO_3$) and molybdates ($SrMoO_4$) since their formation is highly favored by the presence of *Ni* in the perovskite lattice and by the exsolution process. The *Ni* act as catalyst and lead to the formation of $SrCO_3$ by hindering the CO_2 dissociation, at the same time *Ni* is also responsible for the stabilization of the insulating phase $SrMoO_4$. Their presence has negative impact on SFNM04 properties and ability to produce *CO*. In the view of the facts, regarding the future experimental test on this material, it would be necessary to investigate

the aspect of complete oxidation/reduction of the sample by integrating thermogravimetric, XRD (X-ray diffraction), and SEM (Scanning Electron Microscopy) analysis. For example, a post-mortem XRD analysis would be extremely useful to detect eventual detrimental phases in the sample and to observe any structural variation in comparison to an as-synthesized sample. Nevertheless, a further investigation through microreactor tests is necessary in order to identify the best operating conditions for SFNM04 trying to achieve the best possible results optimizing the *CO* production and the global yield.

However, the investigated material represent a promising alternative to the conventional materials (metal oxide, ceria, etc.) used as oxygen carriers in the chemical looping processes. The main objective is to obtain attractive results using lower operating temperatures, also facilitating the integration of the chemical looping process with solar thermal energy. CSP technologies represent the main candidates for this purpose but some technological issues have to be overcome yet, such as the source discontinuity, the large thermal inertia, high-temperature resistant materials, and operating temperature values which make the application not yet feasible in an efficient and reliable way. The ideal goal of such a technology is to produced synthetic fuels like syngas (H_2 and *CO* mixture) and hydrogen aiming at a decarbonization path. In addition to solar energy, carbon capture technologies play a huge role in terms of reducing CO_2 emissions, and the captured carbon dioxide can be then reused in order to fulfill the environmental constraints in order to reduce the environmental impact. The coupling of such a technology with chemical looping processes it could make it possible to reduce emissions and concretely favor the transition to less impacting technologies. However, a lot of work is still needed in order to develop these technologies making them more efficient and feasible, in fact the use of perovskite materials in chemical looping processes need to be further investigated and experimented pushing the technology readiness level (TRL), currently around 3-4, to higher values in order to validate the technology in laboratory scale first, and then industrially. The road toward a mature technology is still long and efforts are still required in order to improve and enhanced it to higher levels. In conclusion, SFNM04 material investigated in this work, represents one of the promising alternative to well-known materials currently

used, but many others may be synthetized and discovered in the next future, and they may speed up the technology validation process and achieve results and performances that will made possible to replace the technologies currently on the market.

References

[1] IPCC, 2014: *Climate Change 2014: Synthesis Report. Contribution of Working Groups I, II and III to the Fifth Assessment Report of the Intergovernmental Panel on Climate Change* [Core Writing Team, R.K. Pachauri and L.A. Meyer (eds.)]. IPCC, Geneva, Switzerland, 151 pp.

[2] IPCC, 2018: *Global Warming of 1.5°C. An IPCC Special Report on the impacts of global warming of 1.5°C above pre-industrial levels and related global greenhouse gas emission pathways, in the context of strengthening the global response to the threat of climate change, sustainable development, and efforts to eradicate poverty* [Masson-Delmotte, V., P. Zhai, H.-O. Pörtner, D. Roberts, J. Skea, P.R. Shukla,A. Pirani, W. Moufouma-Okia, C. Péan, R. Pidcock, S. Connors, J.B.R. Matthews, Y. Chen, X. Zhou, M.I. Gomis, E. Lonnoy, T. Maycock,M. Tignor, and T. Waterfield (eds.)]. In Press. 2019.

[3] Elena Rozzi, Francesco Demetrio Minuto, Andrea Lanzini, Pierluigi Leone, "*Green Synthetic Fuels: Renewable Routes for the Conversion of Non-Fossil Feedstocks into Gaseous Fuels and Their End Uses".* In *Energies* 2020, 13(2), 420.

[4] https://www.worldenergydata.org/world-electricity-generation/

[5] IEA, *Global Energy & CO2 Status Report 2018*. 2019

[6] IEA, IRENA, UNSD, World Bank, WHO. 2020. Tracking SDG 7: The Energy Progress Report. World Bank, Washington DC. c World Bank. License: Creative Commons Attribution—NonCommercial 3.0 IGO (CC BY-NC 3.0 IGO). 2020.

[7] IEA, *CO2 emissions from fuel combustion HIGHLIGHTS* (2019 edition), 2019.

[8] IEA, *The Future of Hydrogen for G20*; IEA: Paris, France, 2019.

[9] IEA, *Transforming Industry through CCUS,* IEA: Paris, France, 2019.

[10] Mai Bui, Claire S. Adjiman, André Bardow, Edward J. Anthony, Andy Boston, Solomon Brown, Paul S. Fennell, Sabine Fuss, Amparo Galindo, Leigh A. Hackett, Jason P. Hallett, Howard J. Herzorg, George Jackson, Jasmin Kemper, Samuel Krevor, Geoffrey C. Maitland, Michael Matuszewski, Ian S. Metcalfe, Camille Petit, Graeme Puxty, Jeffrey Reimer, David M. Reiner, Edward S. Rubin, Stuart A. Scott, Nilay Shah, Berend Smit, J. P. Martin Trusler, Paul Webley, Jennifer Wilcox, Niall Mac Dowell, "*Carbon capture and storage (CCS): the way forward*". In *Energy & Environmental Science,* 2018, 11, 1062.

[11] Gabriele Centi, Siglinda Perathoner, *"Opportunities and prospects in the chemical recycling of carbon dioxide to fuels"*. In *Catalysis Today*, vol. 148, pp, 191-205, 2009.

[12] P.L. Spath, D.C. Dayton, Preliminary Screening, "*Technical and Economic Assessment of Synthesis Gas to Fuels and Chemicals with Emphasis on the Potential for Biomass-Derived Syngas*", 2003.

[13] Christopher Graves, Sune D. Ebbesen, Mogens Mogensen, Klaus S. Lackner, "*Sustainable hydrocarbon fuels by recycling CO2 and H2O with renewable or nuclear energy*". In *Renewable and Sustainable Energy Reviews*, vol. 15, pp. 1-23, 2011.

[14] H.I. Villafan-Vidales, C.A. Arancibia-Bulnes, D. Riveros-Rosas, H. Romero-Paredes, C.A Estrada, "*An overview of the solar thermochemical*

processes for hydrogen and syngas production: Reactors, and facilities". In *Renewable and Sustainable Energy Reviews,* vol. 75, pp 894-908, 2017.

[15] Christos Agrafiotis, Martin Roeb, Christian Sattler, "*A review on solar thermochemical syngas production via redox pair-based water/carbon dioxide splitting thermochemical cycles"*. In *Renewable and Sustainable Energy Reviews*, vol. 42, pp. 254-285, 2015.

[16] Lan Xiao, Shuang-Ying Wu, You-Rong Li, "*Advances in solar hydrogen production via two-step water-splitting thermochemical cycles based on metal redox reactions"*. In *Renwable Energy*, vol. 41, pp. 1-12, 2012.

[17] Deepak Yadav, Rangan Banjeree, "*A review of solar thermochemical processes"*. In *Renewable and Sustainable Energy Reviews*, vol. 54, pp. 497-532, 2016.

[18] I. Alxneit, "*Assessing the feasibility of separating a stoichiometric mixture of zinc vapor and oxygen by a fast quench – Model calculations*". In *Solar Energy*, vol. 82, pp. 959-964, 2008.

[19] Christopher L. Munich, Samuel Blaser, Marie C. Hoes, Aldo Steinfeld, "*Comparing the solar-to-fuel energy conversion efficiency of ceria and perovskite based thermochemical redox cycles for splitting H2O and CO2"*. In *International Journal of Hydrogen Energy,* vol. 43, pp. 18814-18831, 2018.

[20] IEAGHG, "*Information Sheets for CCS"*, 2013/16, November 2013.

[21] IEA, *"Energy Technology Perspectives 2020 – Special Report on Carbon Capture Utilization and Storage"*, 2020.

[22] Global CCS Institute, "*Global Status of CCS 2020"*, 2020.

[23] European Federation of Geologists, "*Carbon Capture & Storage"*, 2020.

[24] Dennis Y. C. Leung, Giorgio Caramanna, M. Mercedes Maroto-Valer, "*An overview of current status of carbon dioxide capture and storage technologies*". In *Renewable and Sustainable Energy Reviews*, vol. 39, pp. 426-443, 2014.

[25] Eliane Blomen, Chris Hendriks, Filip Neele, "*Capture technologies: Improvements and promising developments*". In *Energy Procedia*, vol. 1, pp. 1505-1512, 2009.

[26] P. Chiesa, G. Lozza, A. Malandrino, M. Romano, V. Piccolo, "*Three-reactors chemical looping process for hydrogen production*". In *International Journal of Hydrogen Energy*, vol. 33, pp. 2233-2245, 2008.

[27] IPCC, 2005: IPCC Special Report on Carbon Dioxide Capture and Storage. Prepared by Working Group III of the Intergovernmental Panel on Climate Change [Metz, B., O. Davidson, H. C. de Coninck, M. Loos, and L. A. Meyer (eds.)]. Cambridge University Press, Cambridge, United Kingdom and New York, NY, USA, 442 pp., 2005.

[28] Mohamed A. Habib, Medhat Nemitallah, Rached Ben-Mansour, "*Recent Development in Oxy-Combustion Technology and its Applications to Gas Turbine Combustors and ITM Reactors*". In *Energy Fuels*, 2013, 27, 1, 2-19.

[29] Notes from the course "*Polygeneration and advanced energy systems*" held by prof. M. Santarelli, Politecnico di Torino, a.y. 2019/2020.

[30] Rosa M. Cuellar-Franca, Adisa Azapagic, "*Carbon capture, storage and utilization technologies: A critical analysis and comparison of their life*

cycle environmental impacts". In *Journal of CO2 Utilization*, vol. 9, pp. 82-102, 2015.

[31] ENEA, V. Calabrò, A. Iulianelli, S. Liguori, A. Basile, A. Gugliuzza, A. Saraceno, "*Stato dell'arte sui processi di rimozione della* CO_2 *mediante tecnologie a membrana*", 2011.

[32] ENEA, M. G. De Angelis, M. Giacinti Baschetti, M. Minelli, L. Olivieri, P. Deiana, C. Bassano, "*Sintesi, caratterizzazione e prova di membrana per la separazione della* CO_2 *e la purificazione del Synthetic Natural Gas (SNG)*", 2014.

[33] F. Pelayo García de Arquer, Cao-Thang Dinh, Adnan Ozden2, Joshua Wicks, Christopher McCallum, Ahmad R. Kirmani, Dae-Hyun Nam, Christine Gabardo, Ali Seifitokaldani, Xue Wang, Yuguang C. Li, Fengwang Li, Jonathan Edwards, Lee J. Richter, Steven J. Thorpe, David Sinton, Edward H. Sargent, "CO_2 *electrolysis to multicarbon products at activities greater than 1 A/cm*^{2}". In *Science*, vol. 367, pp. 661-666, 2020.

[34] Severin Foit, Lucy Dittrich, Tobias Duyster, Izaak Vinke, Rüdiger-A. Eichel, L. G. J. (Bert) de Haart, "*Direct Solid Oxide Electrolysis of Carbon Dioxide: Analysis of Performance and Process*". In *Processes*, 8(11), 1390 2020.

[35] Vignesh Kumaravel, John, Bartlett, Suresh C. Pillai, "*Photoelectrochemical Conversion of Carbon Dioxide into fuels and Value-added Products*". In *ACS Energy Lett.* 5, 2, 486-519, 2020.

[36] Maria Tou, Jian Jin, Yong Hao, Aldo Steinfeld, Ronald Michalsky, "*Solar-driven co-thermolysis of CO2 and H2O promoted by in situ oxygen removal across a non-stoichiometric ceria membrane*". In *Reaction Chemistry & Engineering*, 4, 1431, 2019.

[37] Huang Dan, "*Sulfur-Iodine thermochemical cycle for hydrogen production*", 2009.

[38] A. Edrisi, Z. Mansoori, B. Dabir, "*Using three chemical looping reactors in ammonia production process – A novel plant configuration for a green production*". In *International Journal of Hydrogen Energy*, vol. 39, pp. 8271-8282, 2014.

[39] Liang Zeng, Fanxing Li, Ray Kim, Samuel Bayham, Omar McGiveron, Andrew Tong, Daniel Connell, Siwei Luo, Deepak Sridhar, Fei Wang, Zhenchao Sun, Liang-Shih Fan, "*Coal direct chemical looping retrofit to pulverized coal power plants for in-situ CO_2 capture*", 2013.

[40] Ronald W. Breault, "*Handbook of Chemical Looping Technology*", 2019.

[41] Anders Lyngfelt, "*Chemical-looping combustion of solid fuels – Status of development*". In *Applied Energy*, vol. 113, pp. 1869-1873, 2014.

[42] Xing Zhu, Yonggang Wei, Hua Wang, Kongzhai Li, "*Ce-Fe oxygen carriers for chemical-looping steam methane reforming*". In *International Journal of Hydrogen Energy,* vol. 38, pp. 4492-4501, 2013.

[43] Xing Zhu, Kongzhai Li, Yoggang Wei, Hua Wang, Lingyue Sun, "*Chemical-Looping Steam Methane Reforming over a CeO2-Fe2O3 Oxygen Carrier: Evolution of its Structure and Reducibility*". In *Energy Fuels*, 28, 2, 754-760, 2014.

[44] Lin Zhu, Luling Li, Junming Fan, "*A modified process for overcoming the drawbacks of conventional steam methane reforming for hydrogen production: Thermodynamic investigation*". In *Chemical Engineering Research and Design*, vol. 104, pp. 792-806, 2015.

[45] Magnus Ryden, Anders Lyngfelt, Tobias Mattisson, De Chen, Anders Holmen, Erlend Bjorgum, "*Novel oxygen-carrier materials for chemical-looping combustion and chemical-looping reforming;* $La_xSr_{1-x}Fe_yCo_{1-y}O_{3-\delta}$ *perovskite and mixed-metal oxides of NiO, Fe2O3 and Mn3O4*". In *Energy & Environmental Science*, 2008.

[46] Azharuddin Farooqui, Felice Di Tommaso, Archishman Bose, Domenico Ferrero, Jordi Llorca, Massimo Santarelli, "*Techno-economic and exergy analysis of polygeneration plant for power and DME production with the integration of chemical looping* CO_2/H_2O *splitting*". In *Energy Conversion and Management*, vol. 186, pp. 200-219, 2019.

[47] A. Steinfeld, R. Palumbo, "*Solar thermochemical process technology*". In *Academic Press,* vol. 15, pp. 237-256, 2001.

[48] Peter G. Loutzenhiser, Anton Meier, Aldo Steinfeld, "*Review of Two-Step* H_2O/CO_2 *– Splitting Solar Thermochemical Cycle Based on Zn/ZnO Redox Reactions*". In *Materials*, vol. 3, pp. 4922-4938, 2010.

[49] E. Koepf, I. Alxneit, C. Wieckert, A. Meier, "*A review of high temperature solar driven reactor technology: 25 years of experience in research and development at the Paul Scherrer Institute*". In *Applied Energy*, vol. 188, pp. 620-651, 2017.

[50] Srirat Chuayboon, Stephane Abanades, Sylvain Rodat, "*Solar chemical looping gasification of biomass with the ZnO/Zn redox system for syngas and zinc production in a continuously-fed solar reactor*". In *Fuel*, vol. 215, pp. 66-79, 2018.

[51] M. Kromer, K. Roth, R. Takata, P. Chin, "*Support for cost analyses on solar-driven high temperature thermochemical water-splitting cycles*". In 2011.

[52] M. Chambon, S. Abanades, G. Flamant, "*Kinetic investigation of hydrogen generation from hydrolysis of SnO and Zn solar nanopowders*". In *International Journal of Hydrogen Energy*, vol. 34, pp. 5326-5336, 2009.

[53] K-S. Kang, C-H. Kim, W-C. Cho, K-K. Bae, S-H. Kim, C-S. Park, "*Novel two-step thermochemical cycle for hydrogen production from water using germanium oxide: KIER 4 thermochemical cycle*". In *International Journal of Hydrogen Energy*, vol. 34, pp. 4283-4290, 2009.

[54] W. Villasmil, A. Meier, A. Steinfled, "*Dynamic modelling of a solar reactor for zinc oxide thermal dissociation and experimental validation using IR thermography*". In *Journal of Solar Energy Engineering*, 136(1), 11 pages 2014.

[55] B. Buflin, J. Vieten, C. Agrafiotis, M. Roeb, C. Sattler, "*Applications and Limitations of Two Step Metal Oxide Thermochemical Redox Cycles; A Review*". In *Journal of Materials Chemistry A,* vol. 5, pp. 18951-18966, 2017.

[56] T. Nakamura, "*Hydrogen production from water utilizing solar heat at high temperature*". In *Solar Energy*, vol. 19, pp. 467-475, 1977.

[57] T. Kodama, Y. Kondoh, A. Kiyama, K-I. Shimizu, "*Hydrogen production by solar thermochemical water-splitting/methane-reforming process*". In *International Solar Energy Conference*, 44037, pp. 121-128, 2003.

[58] N. Gokon, T. Mizuno, S. Takahashi, T. Kodama, "*A two-step water splitting with ferrite particles and its new reactor concept using an internally*

circulating fluidized bed". In *International Solar Energy Conference*, 99063, pp. 205-214, 2006.

[59] T. Kodama, Y. Nakamuro, T. Mizuno, R. Yamamoto, "*A two-step thermochemical water splitting by iron-oxide on stabilized zirconia*". In *Journal of Solar Energy Engineering*, 128(1), pp. 3-7, 2004.

[60] N. Gokon, H. Murayama, A. Nagasaki, T. Kodama, "*Thermochemical two-step water splitting cycles by monoclinic ZrO_2-supported m- $NiFe_2O_4$ and Fe_3O_4 powders and ceramic foam devices*". In *Solar Energy*, vol. 83, pp. 527-537, 2009.

[61] N. Gokon, T. Kodoma, N. Imaizumi, J. Umeda, T. Seo, "*Ferrite/zirconia-coated foam device prepared by spin coating for solar demonstration of thermochemical water-splitting*". In *International Journal of Hydrogen Energy*, vol.36, pp.2014-2028, 2011.

[62] S. Abanades, G. Flamant, "*Thermochemical hydrogen production from a two-step solar-driven water-splitting cycle based on cerium oxides*". In *Solar Energy*, vol.80, pp.1611-1623, 2006.

[63] WC. Chueh, SM. Haile, "*Ceria as a thermochemical reaction medium for selectively generating syngas or methane from H2O and CO2*". In *ChemSusChem*, vol.2, pp.735-739, 2009.

[64] WC Chueh, C. Falter, M. Abbott, D. Scipio, P. Furler, SM. Haile, "*High-flux solar-driven thermochemical dissociation of CO2 and H2O sin non-stoichiometric ceria*". In *Science*, vol.330, pp.1797-1801, 2010.

[65] P. Furler, JR. Scheffe, A. Steinfeld, "*Syngas production by simultaneous splitting of H2O and CO2 via ceria redox reactions in a high-temperature*

solar reactor". In *Energy & Environmental Science*, vol.5, pp.6098-6103, 2012.

[66] P. Furler, J. Scheffe, M. Gorbar, L. Moes, U. Vogt, A. Steinfeld, "*Solar thermochemical CO2 splitting utilizing a reticulated porous ceria redox system*". In *Energy Fuels*, 26, 11, pp.7051-7059, 2012.

[67] P. Furler, J. Scheffe, D. Marxer, M. Gorbar, A. Bonk LJ. Vogt, "*Thermochemical CO2 splitting via redox cycling of ceria reticulated foam structures with dual-scale porosities*". In *Physical Chemistry Chemical Physics*, vol.16, pp.10503-10511, 2014.

[68] S. Ackermann, L. Sauvin, R. Castiglioni, J. L. Rupp, J. R. Scheffe, A. Steinfeld, "*Kinetics of CO2 reduction over nonstoichiometric ceria*". In *The Journal of Physical Chemistry C*, 119, 29, pp.16452-16461, 2015.

[69] A. E. Farooqui, A. Manfredi Pica, P. Marocco, D. Ferrero, A. Lanzini, S. Fiorilli, J. Llorca, M. Santarelli, "*Assessment of kinetic model for ceria oxidation for chemical-looping CO2 dissociation*". In *Chemical Engineering Journal*, vol. 346, pp.171-181, 2018.

[70] QL. Meng, C. Lee, T. Ishihara, H. Kaneko, Y. Tamaura, "*Reactivity of CeO2-based ceramics for solar hydrogen production via a two-step water-splitting cycle with concentrated solar energy*". In *International Journal of Hydrogen Energy*, vol.36, pp.13435-13441, 2011.

[71] A. Le Gal, S. Abanades, "*Catalytic investigation of ceria-zirconia solid solutions for solar hydrogen production*". In *International Journal of Hydrogen Energy*, vol.36, pp.4739-4748, 2011.

[72] S. Kawakami, T. Myojin, HS. Cho, T. Hatamachi, N. Gokon, T. Kodama, "*Thermochemical two-step water splitting cycle using Ni-ferrite and CeO2*

coated ceramic foam devices by concentrated Xe-light radiation". In *Energy Procdia,* vol.49, pp-1980-1989, 2014.

[73] A. Le Gal, S. Abanades, "*Dopant incorporation in ceria for enhanced water-splitting activity during solar thermochemical hydrogen generation*". In *The Journal of Physical Chemistry C*, 116, 25, pp.13516-13523, 2012.

[74] Q. Jiang, G. Zhou, Z. Jiang, C. Li, "*Thermochemical CO_2 splitting reaction with $Ce_xM_{1-x}O_{2-\delta}$ ($M = Ti^{4+}$, Sn^{4+}, Hf^{4+}, Zr^{4+}, La^{3+}, Y^{3+}, and Sm^3) solid solutions*". In *Journal of Materials Chemistry A*, vol.5, pp.6874-6883, 2014.

[75] G.D. Takalkar, R.R. Bhosale, A. Kumar, F. AlMomani, M. Khraisheh, R. A. Shakoor, "*Transition metal doped ceria for solar thermochemical fuel production*". In *Solar Energy*, vol.172, pp.204-211, 2018.

[76] Mingchen Tang, Long Xu, Maohong Fan, "*Progress in oxygen carrier development of methane-based chemical-looping reforming: A review*". In *Applied Energy*, vol.151, pp.143-156, 2015.

[77] Anita Haeussler, Stephane Abanades, Julien Jouannaux, Anne Julbe, "*Non-stoichiometric redox active perovskite materials for solar thermochemical fuel production: A review*". In *Catalysts*, 8(12), 611, 2018.

[78] Marlus Kubicek, Alexander H. Bork, Jennifer L. M. Rupp, "*Perovskite oxides – a review on versatile material class for solar-to-fuel conversion process*". In *Journal of Materials Chemistry A,* vol.5, pp.11983-12000, 2017.

[79] Raymond E. Schaak, Thomas E. Mallouk, "*Perovskite by design: A toolbox of solid-state reactions*". In *Chemistry of Materials*, 14, 4, pp.1455-1471, 2002.

[80] Olga Savinskaya, Alexnder P. Nemudry, "*Oxygen transport properties of nanostructured $SrFe_{1-x}Mo_xO_{2.5+3/2x}$ (0<x<0.1) perovskites*". In *Accounts of Chemical Research*, 47, 11, pp.3340-3348, 2011.

[81] Peter I. Cowin, Christopher T. G. Petit, Rong Lan, John T. S. Irvine, Shanwen Tao, "*Recent progress in the development of anode materials for solid oxide fuel cells*". In *Advanced Energy Materials*, vol.1, pp.314-332, 2011.

[82] J. A. Kilner, A. Berenov, J. Rossiny, "*Perovskite oxide for solid oxide fuel cells*", 2009.

[83] Long Jiang, Gan Liang, Jiantao Han, Yunhui Huang, "*Effects of Sr-site deficiency on structure and electrochemical performance in Sr_2MgMoO_6 for solid-oxide fuel cell*". In *Journal of Power Sources*, vol.270, pp.441-448, 2014.

[84] Kun Zhao, Fang He, Zhen Huang, Anqing, Zheng, Haibin Li, Zengli Zhao, "*Three-dimensionally ordered macroporous $LaFeO_3$ perovskites for chemical-looping steam reforming of methane*". In *International Journal of Hydrogen Energy*, vol.39, pp.3243-3252, 2014.

[85] Kun Zhao, Fang He, Zhen Huang, Guoqiang Wei, Anqing Zheng, Haibin Li, Zengli Zhao, "*Perovskite-type oxides $LaFe_{1-x}Co_xO_3$ for chemical looping steam methane reforming to syngas and hydrogen co-production*". In *Applied Energy*, 2016.

[86] Qingqing Jiang, Jinhui Tong, Guilin Zhou, Zongxuan Jiang, Zhen Li, Can Li, "*Thermochemical CO_2 splitting reaction with supported $La_xA_{1-x}Fe_yB_{1-y}O_3$ (A=Sr, Ce, B=Co, Mn; 0<x, y<1) perovskite oxides*". In *Solar Energy*, 2014.

[87] Anita Haeussler, Stephane Abanades, Anne Julbe, Julien Jouannaux, Bruno Cartoixa, "*Two-step CO_2 and H_2O splitting using perovskite-coated ceria foam for enhanced green fuel production in a porous volumetric solar reactor*". In *Journal of CO2 Utilization*, vol.41, pp.101257, 2020.

[88] Antoine Demont, Stephane Abanades, Eric Beche, "*Investigation of perovskite structures as oxygen-exchange redox materials for hydrogen production from thermochemical two-step water-splitting cycles*". In *The Journal of Physical Chemistry C*, 118, 24, 12682-12692, 2014.

[89] Chih-Kai Yang, Yoshihiro Yamazaki, Aykut Aydin, Sossina M. Haile, "*Thermodynamic and kinetic assessment of strontium-doped lanthanum magnetite perovskites for two-step thermochemical water splitting*". In *Journal of Materials Chemistry A*, vol.2, pp.13612-13623, 2014.

[90] Jonathan R. Scheffe, David Weibel, Aldo Steinfeld, "*Lanthanum-strontium-manganese perovskites as redox materials for solar thermochemical splitting of H_2O and CO_2*". In *Energy Fuels*, 27, 8, pp.4250-4257, 2013.

[91] Feng Zheng, Larry R. Pederson, "*Phase behavior of lanthanum strontium manganites*". In *Journal of the Electrochemical Society*, vol.146, pp.2810, 1999.

[92] Lulu Wang, Mohammad Al-Mamun, Porun Liu, Yu Lin Zhong, Yun Wang, Hua Gui Yang, Huijun Zhao, "*Enhanced thermochemical H_2 production on Ca-doped lanthanum magnetite perovskites through optimizing the dopant level and re-oxidation temperature*". In *Acta Metallurgica Sinica*, 31(4), pp.431-439, 2017.

[93] Sunita Dey, B. S. Naidu, A. Govindaraj, C. N. R. Rao, "*Noteworthy performance of $La_{1-x}Ca_xMnO_3$ perovskites in generating H_2 and CO by*

the thermochemical splitting of H_2O and CO_2". In *Physical Chemistry Chemical Physics*, vol.17, pp.122-125, 2014.

[94] A. Demont, S. Abanades, "*Solar thermochemical conversion of CO_2 into fuel via two-step redox cycling of non-stoichiometric Mn-containing perovskite oxides*". In *Journal of Materials Chemistry A*, vol.3, pp.3536-3546, 2015.

[95] M. M. Nair, S. Abanades, "*Insights into the redox performance of non-stoichiometric lanthanum manganite perovskites for solar thermochemical CO_2 splitting*". In *ChemestrySelect*, vol.1, pp.4449-4457, 2016.

[96] Thomsa Cooper, Jonathan R. Scheffe, Maria E. Galvez, Roger Jacot, Greta Patzke, Aldo Steinfeld, "*Lanthanum manganite perovskites with Ca/Sr A-site and Al B-site doping as effective oxygen exchange materials for solar thermochemical fuel production*". In *Energy Technology*, vol.3, pp.1130-1142, 2015.

[97] Mahesh M. Nair, Stephane Abanades, "*Experimental screening of perovskite oxides as efficient redox materials for solar thermochemical CO_2 conversion*". In *Sustainable Energy & Fuels*, vol.2, pp.843-854, 2018.

[98] Lulu Wang, Mohammad Al-Mamun, Porun Liu, Yun Wang, Hua Gui Yang, Huijun Zhao, "*Notable hydrogen production on $La_xCa_{1-x}CoO_3$ perovskites via two-step thermochemical water splitting*". In *Journal of Materials Science*, vol.53, pp.6796-6806, 2004.

[99] Maria Orfila, Maria Linares, Raul Molina, Juan Angel Botas, Raul Sanz, Javier Marugan, "*Perovskite materials for hydrogen production by thermochemical water splitting*". In *International Journal of Hydrogen Energy*, vol.41(42), pp.1-10, 2016.

[100] Qiongqiong Jiang, Yali Cao, Xiangyu Liu, Hao Zhang, Hui Hong, Hongguang Jin, "*Chemical looping combustion over a lanthanum nickel perovskite-type oxygen carrier with facilitated O^{2-} transport*". In *Energy Fuels*, 34, 7, pp.8732-8739, 2020.

[101] Qiongqiong Jiang, Hao Zhang, Yali Cao, Hui Hong, Hongguang Jin, "*Solar hydrogen production via perovskite-based chemical-looping steam methane reforming*". In *Energy Conversion and Management*, vol.187, pp.523-536, 2019.

[102] Fang He, Xinai Li, Kun Zhao, Zhen Huang, Guoqiang Wei, Haibin Li, "*The use of $La_{1-x}Sr_xFeO_3$ perovskite-type oxides as oxygen carriers in chemical-looping reforming of methane*". In *Fuel*, vol.108, pp.465-473, 2013.

[103] Sunita Dey, B. S. Naidu, C. N. R. Rao, "*$Ln_{0.5}A_{0.5}MnO_3$ (Ln=Lanthanide, A=Ca, Sr) perovskites exhibiting remarkable performance in the thermochemical generation of Co and H_2 from CO_2 to H_2O*". In *Chemistry -A European Journal*, vol.21, pp.7077-7081, 2015.

[104] A. H. McDaniel, E. C. Miller, D. Arifin, A. Ambrosini, E. N. Coker, R. O'Hayre, W. C. Chueh, J. Tong, "*Sr- and Mn-doped $LaAlO_{3-\delta}$ for solar thermochemical H_2 and CO production*". In *Energy & Environmental Science*, vol.6, pp.2424-2428, 2013.

[105] M. E. Galvez, R. Jacot, J. Scheffe, T. Cooper, G. Patzke, A. Steinfeld, "*Physico-chemical changes in Ca, Sr, and Al-doped La-Mn-O perovskites upon thermochemical splitting of CO_2 via redox cycling*". In *Physical Chemistry Chemical Physics*, vol.17, pp.6629-6634, 2015.

[106] M. Takacs, M. Hoes, M. Caduff, T. Cooper, J. R. Scheffe, A. Steinfeld, "*Oxygen nonstoichiometry, defect equilibria, and thermodynamic*

characterization of $LaMnO_3$ perovskites with Ca/Sr A-site and Al B-site doping". In *Acta Materialia*, vol.103, pp.700-710, 2016.

[107] Lulu Wang, Mohammad Al-Mamun, Yu Lin Zhong, Lixue Jiang, Porun Liu, Yun Wang, Hua Gui Yang, Huijun Zhao, "*Ca^{2+} and Ga^{3+} doped $LaMnO_3$ perovskite as a highly efficient and stable catalyst for two-step thermochemical water splitting*". In *Sustainable Energy & Fuels*, vol.1, pp.1013-1017, 2016.

[108] M. V. Patrakeev, E. B. Mitbeg, A. A. Lakhtin, I. A. Leonidov, V. L. Kozhenikov, V. V. Kharton, M. Avdeev, F. M. B. Marques, "*Oxygen nonstoichiometry, conductivity, and Seebeck coefficient of $La_{0.3}Sr_{0.7}Fe_{1-x}Ga_xO_{2.65+\delta}$ perovskites*". In *Journal of Solid State Chemistry*, vol.167, pp.203-213, 2002.

[109] Julien Jouannaux, Anita Haeussler, Martin Drobek, André Ayral, Stephane Abanades, Anne Julbe, "*Lanthanum manganite perovskite ceramic powders for CO_2 splitting: Influence of Pechini synthesis parameters on sinterability and reactivity*". In *Ceramics International*, vol.45, pp.15636-15648, 2019.

[110] Alfonso J. Carrillo, Alexander H. Bork, Thierry Moser, Eva Sediva, Zachary D. Hood, Jennifer L. M. Rupp, "*Modifying $La_{0.6}Sr_{0.4}MnO_3$ perovskites with Cr incorporation for fast isothermal CO_2-splitting kinetics in solar-driven thermochemical cycles*". In *Advanced Energy Materials*, vol.9, 2019.

[111] G. Luciani, G. Landi, A. Aronne, A. Di Benedetto, "*Partial substitution of B cation in $La_{0.6}Sr_{0.4}MnO_3$ perovskites: A promising strategy to improve the redox properties useful for solar thermochemical water and carbon dioxide splitting*". In *Solar Energy*, vol.171, pp.1-7, 2018.

[112] Sean M. Babiniec, Eric N. Coker, James E. Miller, Andrea Ambrosini, "*Investigation of $La_xSr_{1-x}Co_{1-y}M_yO_{3-\delta}$ (M=Mn, Fe) perovskite materials*

as thermochemical energy storage media". In *Solar Energy*, vol.118, pp.451-459, 2015.

[113] A. H. Bork, M. Kubicek, M. Struzik and J. L. M. Rupp, "*Perovskite $La_{0.6}Sr_{0.4}Cr_{1-x}Co_xO_{3-\delta}$ solid solutions for solar-thermochemical fuel production: strategies to lower the operation temperature*". In *Journal of Materials Chemistry A*, vol.3, pp.15546-15557, 2015.

[114] Tom Van Gerven, Guido Mul, Jacob Moulijn, Andrzej Stankievicz, "*A review of intensification of photocatalytic processes*". In *Chemical Engineering and Processing: Process Intensification*, vol.46, pp.781-789, 2007.

[115] Gerard N. Kraai, Floris Van Zwol, Boelo Schuur, Hero J. Heeres, Johannes G. De Vries, "*Two-phase (bio)catalytic reactions in a table-top centrifugal contact separator*". In *Angewandte Chemie International Edition*, vol.47, pp.3905-3908, 2008.

[116] A. Pohar, I. Plazl, "*Process intensification through microreactor application*". In *Chemical and Biochemical Engineering Quarterly,* 23(4), pp.537-544, 2009.

[117] Invensys Eurotherm, "*iTools Help Manual*", 2010.

[118] Carbolite GeroLtd. "*Carbolite Gero 3000°C, furnace brochure catalogue*".

[119] API SRL, "*Manuale API-MIoT Poli_To*", 2020.

[120] Xiao Liu, Sitian Cheng, Hong Liu, Sha Hu, Daqiang Zhang, Huansheng Ning, "*A survey on gas sensing technology*". In *Sensors*, 12(7), pp.9635-9665, 2012.

[121] Yu-Feng Sun, Shao-Bo Liu, Fan-Li Meng, Jin-Yun Liu, Zhen Jin, Ling-Tao Kong, Jin-Huai Liu, "*Metal oxide nanostructured and their gas sensing properties: A review*". In *Sensors*, 12(3), pp.2610-2631, 2012.

[122] S. B. Twiss, D. M. Teague, J. W. Bozek, M. V. Sink, "*Application of infrared spectroscopy to exhaust gas analysis*". In *Journal of the Air Pollution Control Association*, 5:2, pp.75-83, 2012.

[123] XSTREAM, "*Gas analyzers Z-Stream enhanced series – Instruction Manual*", 2017.

[124] Marta Boaro, Andrea Felli, "*PRIN17 Project Direct Biopower*", 2020.

[125] Xiao-Ming Ge, Siew-Hwa Chan, Qing-Lin Liu, Qiang Sun, "*Solide oxide fuel cell anode materials for direct hydrocarbon utilization*". In *Advanced Energy Material,* vol.2, pp.1156-1181, 2012.

[126] Martin Hoffman, Victor N, Antonov, Lev V. Bekenov, Kalevi Kokko, Wolfram Hergert, Arthur Ernst, "*Variation of magnetic properties of Sr_2FeMoO_6 due to oxygen vacancies*". In *Journal of Physics: Condensed Matter*, vol.30, 305801, 2018.

[127] M. Retuerto, M. Martinez-Lope, M. Garcia-Hernandez, J. A. Alonso, "*High-pressure synthesis of the double perovskite Sr_2FeMoO_6: increment of the cationic ordering and enhanced magnetic properties*". In *Journal of Physics: Condensed Matter*, vol.21, 186003, 2009.

[128] Falak Sher, A. J. Williams, A. Venimadhev, Mark G. Blamire, J. Paul Attfield, "*Synthesis, structure, and properties of two new Ruddlesden-Popper phase analogues of SFMO (Sr_2FeMoO_6)*". In *Chemistry of Materials*, 17, 7, pp.1792-1796, 2005.

[129] Yang Song, Qin Zhong, Wenji Tan, Cai Pan, "*Effect of cobalt – substitution* $Sr_2Fe_{1.5-x}Co_xMo_{0.5}O_{6-\delta}$ *for intermediate temperature symmetrical solid oxide fuel cells fed with* H_2-H_2S". In *Electrochemical Acta*, vol.139, pp.13-20, 2014.

[130] Qiang Liu, Xihui Dong, Guoliang Xiao, Fei Zhao, Fanglin Chen, "*A novel electrode material for symmetrical SOFCs*". In *Advanced Materials*, vol.22, pp.5478-5482, 2010.

[131] Qiang Liu, Chenghao Yang, Xihui Dong, Fanglin Chen, "*Perovskite* $Sr_2Fe_{1.5}Mo_{0.5}O_{6-\delta}$ *as electrode materials for symmetrical solid oxide electrolysis cells*". In *International Journal of Hydrogen Energy*, vol.35, pp.10039-10044, 2010.

[132] Ana B. Munoz-Garcia, Daniel E. Bugaris, Michele Pavone, Jason P. Hodges, Ashfia Huq, Fanglin Chen, Hans-Conrad zur Loye, Emily A. Carter, "*Unveiling structure-property relationship in* $Sr_2Fe_{1.5}Mo_{0.5}O_{6-\delta}$*, an electrode material for symmetric solid oxide fuel cells*". In *Journal of the American Chemical Society*, 134, 15, pp.6826-6833, 2012.

[133] Zhihong Du, Hailei Zhao, Sha Yi, Qing Xia, Yue Gong, Yang Zhang, Xing Cheng, Yan Li, Lin Gu, Konrad Swierczek, "*High-performance anode material* $Sr_2FeMo_{0.65}Ni_{0.35}O_{6-\delta}$ *with in situ exsolved nanoparticle catalyst*". In *ACS Nano*, 10, 9, pp.8660-8669, 2016.

[134] Mingyue Hou, Wang Sun, Pengfa Li, Jie Feng, Guoquan Yang, Jinshuo Qiao, Zhenhua Wang, David Rooney, Jinsheng Feng, Kening Sun, "*Investigation into the effect of molybdenum-site substitution on the performance of* $Sr_2Fe_{1.5}Mo_{0.5}O_{6-\delta}$ *for intermediate temperature solid oxide fuel cells*". In *Journal of Materials Chemistry A*, vol.2, pp.17628-17634, 2014.

[135] Yi-Fei Sun, Ya-Qian Zhang, Jian Chen, Jian-Hui Li, Ying-Tao Zhun, Yi-Min Zeng, Babak Shalchi Amirkhiz, Jian Li, Bin Hua, Jing-Li Luo, "*New opportunity for in situ exsolution of metallic nanoparticles on perovskite parent*". In *NANO Letters*, 16, 8, pp.5303-5309, 2016.

[136] Shiqing Hu, Lixiao Zhang, Huanying Liu, Wenping Li, Zhongwei Cao, Lili Cai, Yue Zhu, Xuefeng Zhu, Weishen Yang, "*Detrimental phase evolution triggered by Ni in perovskite-type cathodes for CO_2 electroreduction*". In *Journal of Energy Chemistry*, vol.36, pp.87-94, 2019.

[137] A. V. Nikonov, K. A. Kuterbekov, K. Zh. Bekmyrza, N. B. Pavzderin, "*A brief review of conductivity and thermal expansion of perovskite-related oxides for SOFC cathode*". In *Eurasian Journal of Physics and Functional Materials*, 2(3), pp.274-292, 2018.